NASA CONTRACTOR REPORT

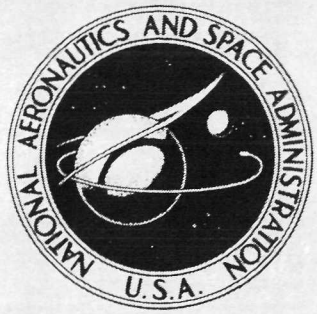

NASA CR-2002

NASA CR-2002

EFFECTS OF LEADING-EDGE CAMBER ON LOW-SPEED CHARACTERISTICS OF SLENDER DELTA WINGS

by W. H. Wentz, Jr.

Prepared by
WICHITA STATE UNIVERSITY
Wichita, Kans.
for Langley Research Center

NATIONAL AERONAUTICS AND SPACE ADMINISTRATION • WASHINGTON, D. C. • OCTOBER 1972

1. Report No.	2. Government Accession No.	3. Recipient's Catalog No.
NASA CR-2002		

4. Title and Subtitle	5. Report Date
EFFECTS OF LEADING-EDGE CAMBER ON LOW-SPEED CHARACTERISTICS OF SLENDER DELTA WINGS	October 1972
	6. Performing Organization Code
7. Author(s)	8. Performing Organization Report No.
W. H. Wentz, Jr.	
9. Performing Organization Name and Address	10. Work Unit No.
Aeronautical Engineering Department Wichita State University Wichita, Kansas	136-13-01-02
	11. Contract or Grant No. NAS1-10082
	13. Type of Report and Period Covered
12. Sponsoring Agency Name and Address	Contractor Report
National Aeronautics and Space Administration Washington, D. C. 20546	14. Sponsoring Agency Code

15. Supplementary Notes

16. Abstract

Wind-tunnel studies have been conducted to determine the effects of leading-edge camber on the low-speed aerodynamic characteristics of a thin, sharp-edge 74° delta wing. The results include force and moment measurements, pressure distributions, and flow visualization patterns determined from oil flow, tuft and water vapor observations. The study indicated that leading-edge camber near the apex is effective in controlling the pitch-up tendency of slender delta wings.

17. Key Words (Suggested by Author(s))	18. Distribution Statement
Slender Wing, Vortex Lift, Camber Effects. Vortex Flow, Leading-Edge Flaps	Unclassified-Unlimited

19. Security Classif. (of this report)	20. Security Classif. (of this page)	21. No. of Pages	22. Price*
Unclassified	Unclassified	106	$3.00

*For sale by the National Technical Information Service, Springfield, Virginia 22151

EFFECTS OF LEADING-EDGE CAMBER ON LOW-SPEED CHARACTERISTICS OF SLENDER DELTA WINGS

By W. H. Wentz, Jr.

SUMMARY

Wind tunnel studies have been conducted to determine the effects of leading-edge camber on the low speed aerodynamic characteristics of a thin, sharp-edge 74° delta wing. Tests were carried out in the Wichita State University 7' by 10' wind tunnel, at a Reynolds number of 1.7×10^6. Data obtained include six-component force measurements, pressure distributions, and flow visualization patterns using oil flow, tufts, and water vapor. Conical and constant percent chord leading-edge cambers were tested, as well as a constant percent chord leading-edge flap. Results show that leading-edge camber near the apex is effective in controlling the destabilizing tendency of slender delta wings at high lift coefficients. Effects of sideslip are discussed in terms of the leading-edge vortex flow.

INTRODUCTION

The necessity of thin low aspect ratio wings for aircraft with efficient supersonic cruising performance is well established. However, an important requirement of any civilian supersonic aircraft is the ability to perform with reasonable efficiency at subsonic speeds for approach, holding, and takeoff and landing operations. Conventional subsonic lifting surface theories such as those of Multhopp, Lamar and Wagner (Refs. 1, 2 and 3) are available for predicting the subsonic performance for cases of fully attached flow on cambered or uncambered wings. For thin wings operating above design angle of attack, leading-edge separation occurs and upper surface vortices appear. These vortices are responsible for large changes in the aerodynamic forces and moments produced by such wings.

Recently, Polhamus developed a very accurate technique for predicting vortex lift and associated drag for sharp-edge flat plate wings (Ref. 4). This technique is based upon consideration of the relationship between the leading-edge suction force and the leading-edge vortices. The technique has not yet been successfully applied to cambered surfaces, since the lift and drag components associated with the vortices (components of the

leading-edge suction force) are strongly dependent upon the location and strength of the vortices. In fact, the nature of leading-edge vortices developed by slender wings with leading-edge camber has not been previously investigated in detail.

The purpose of the present studies is to determine the effects of cambering on the forces and flow fields associated with thin, slender wings at low speeds.

Models consisted of thin delta wings having 74° leading-edge sweep. Flat plate, conical camber and constant percent chord camber surfaces were tested, as well as 15 percent chord leading-edge flaps, with deflections up to 60°. Tests were conducted at a Reynolds Number of 1.7×10^6, pitch angles from -10° to +40°, and sideslip angles from -25° to +25°.

It was felt particularly important to carry out detailed flow visualization and pressure studies along with force measurements, in order to develop the best possible understanding of the leading-edge flow phenomena associated with cambered highly swept surfaces.

SYMBOLS

The longitudinal data are referred to the wind axes and lateral stability data are referred to the body system of axes. The origin for these axes is the moment reference position of 30 percent of the mean aerodynamic chord. Dimensional quantities are given in both International (SI) Units and U.S. Customary Units. Measurements and calculations were made in the U.S. Customary Units. Conversion factors between SI Units and U.S. Customary Units are presented in reference 5. The symbols are defined as follows:

a	wing local semi-span, feet.
b	wing span, feet.
$\bar{c}$	wing mean geometric chord, $\int c^2 dy$/wing area.
c_l	airfoil section lift coefficient, section lift/qS.
C_l	wing rolling moment coefficient, rolling moment/qSb.
C_L	wing lift coefficient, lift/qS.
C_D	wing drag coefficient, drag/qS.
C_{D_o}	wing drag coefficient at zero lift, drag/qS.
C_M	wing pitching moment coefficient about .30$\bar{c}$, moment/qS$\bar{c}$.

C_n	wing yawing moment coefficient, yawing moment/qSb.
C_{N_L}	local longitudinal loading, obtained by spanwise C_p integration.
C_p	pressure coefficient, $(p - p_\infty)/q$.
C_Y	wing sideforce coefficient, sideforce/qS.
q	dynamic pressure, force/area.
X	chordwise coordinate, measured from model trailing edge positive forward.
Y	spanwise coordinate, measured from model centerline positive to right.
α	angle of attack with respect to flat portion of all wings, degrees.
β	angle of sideslip, degrees.
δ_n	leading-edge flap deflection normal to hinge line, degrees

EXPERIMENTAL INVESTIGATIONS

Wind Tunnel Models and Instrumentation

Three design configurations of the wing were chosen; a flat plate delta for baseline data, a wing with constant percent camber at each airfoil station, and a second cambered wing with conical camber. All models have the same planform; a delta wing with 74° leading-edge sweep, and a 76.2 cm (30 in.) centerline chord. All models were fabricated from 0.635 cm (0.25 in.) aluminum plate with sharp leading and trailing edges. Models were fitted with tubing for static surface pressure measurements. The models, pressure tap locations and mounting sting are shown in figures 1 through 6.

The "flat plate" model is the basic 74° leading-edge sweep flat plate delta. The "apex camber" model is composed of NACA 230 mean lines designed for a section lift coefficient of $c_l = 0.5$ (Ref. 6), with the 74° delta planform. The resulting surface has maximum camber at the apex, tapering to zero camber at the wing tip. The "conical camber" model has the same planform, with cambered leading-edges generated as elements of the right circular cones, emanating from the apex. This results in conically cambered leading edges. The camber at the mid semi-span station was selected to match the camber of the apex camber model at mid semi-span. Additional tests were conducted with the flat plate model fitted with 15% chord leading-edge flaps.

A 12° streamwise flap deflection was selected for testing to match the camber of the apex camber model (Fig. 6). Streamwise deflections of 7° and 17° were established as minus and

plus 5° from the nominal value, and a 35° value was added to obtain a setting which more nearly matched the leading-edge slope of the apex camber model. Because of the large sweepback of the flap hinge line, the deflections normal to the hinge line differ considerably from the streamwise angles, as indicated in Table 1.

Table 1 - Leading-Edge Flap Settings

δ streamwise	δ normal to hinge
7°	12°
12°	24°
17°	36°
35°	60°

Experiments were conducted in the Wichita State University 7- x 10-ft. low speed, closed circuit wind tunnel. Tests were conducted at a dynamic pressure of 1916 newtons/meter^2 (40 psf), which corresponds to a Reynolds number of 1.7 x 10^6 based upon mean aerodynamic chord. Six component force data were obtained from all the models, employing a 2.54 cm (1") dia. internal sting balance.

Recent studies by Blackwell (Ref. 7) have shown that for high aspect ratio wings in transonic flow, the location of the transition point may have a strong effect on shock-induced separation point, and will consequently alter force and pressure characteristics significantly. These studies have shown the importance of properly locating trip strips when shock-induced separation is to be simulated. Unfortunately, these studies do not clarify the problem of transition fixing on wings with leading-edge separation.

Transition studies more appropriate to highly swept delta wings have been carried out in the transonic regime by Stahl, Hartmann, and Schneider (Ref. 8). These authors have suggested that significant Reynolds number effects are to be expected at all Mach numbers, even though their studies of Reynolds number effects were restricted to Mach numbers near unity. Because the present tests were carried out at low Mach numbers, it was felt essential to explore the question of transition fixing during the present experiments.

To accomplish this purpose, the models of the present tests were fitted with trip strips along the 65% semi-span locations. Preliminary force measurements were conducted at a series of tunnel speeds, with and without transition strips on upper and lower wing surfaces. The results, presented in detail in reference 9, indicate no substantial changes due to Reynolds number or transition position.

For the purposes of the present tests it was felt that Reynolds number and transition point location were not important unless they were responsible for significant changes in the force and moments produced by the wings. Furthermore, the transition strips do produce local effects on surface pressure fields, due to the contour "bump" of the transition strip. It was therefore deemed best to test without transition fixing, and all subsequent tests were conducted without transition strips.

Data Reduction

The force data from the tunnel was reduced employing the IBM 1130 computer of Wichita State University, and applying the usual wind tunnel boundary corrections. Details are given in Appendix B (Ref. 9). The moments were resolved about the 30% mac location (see fig. 2), using a length of 2/3 centerline chord as the mean aerodynamic chord.

Results of Force Tests

Lift, drag, and pitching moments. - The basic longitudinal force characteristics of the flat plate, apex camber and conical camber wings are shown in figures 7 through 15. It should be noted that the zero angle of attack reference for all models of this study has been selected as the flat plate portion of the wing. This is contrary to the usual practice for high aspect ratio wings, but was deemed advisable in this case for two reasons. First, the amounts of camber tested are substantially greater than that required for optimum supersonic cruise, and would probably be achieved through variable geometry on a practical design. Second, leading-edge cambering of low aspect ratio wings does not produce as much shift in zero lift angle as would occur on low sweep high aspect ratio wings. (See Ref. 10).

Figures 16 and 17 compare the lift and drag results of the cambered models with the experimental results of the flat plate delta wing. Theoretical lift for the flat plate model, based upon Polhamus' leading-edge suction analogy (Ref. 4) is also shown on figure 16, and a theoretical induced drag based upon the leading-edge suction analogy is shown in figure 17. It is seen that the suction analogy is quite accurate for predicting lift and induced drag for uncambered deltas, as reported earlier (Refs. 4, 11, and 12).

At moderate angles of attack, the conical camber and apex camber deltas show less lift than the flat plate. Since the theoretical lift curve slope is independent of camber, the expected ΔC_L due to camber would be given by:

$$\Delta C_L = - \frac{dC_L}{d\alpha} \Delta\alpha \qquad \text{(Equation 1)}$$

Where $\Delta\alpha$ is the change in zero lift angle. The potential lift curve slope from computer studies (Ref. 2) for these planforms is: $dC_L/d\alpha = .0254$ per degree. Using equation 1 and the experimentally observed changes in angle of zero lift, "expected" changes in potential lift may be determined. These are shown in Table 2, along with experimental results.

Table 2 - Effects of Camber on Lift

Model	Experimental Zero Lift Angle *	Experimental C_L@10°	Experimental ΔC_L@10°	Expected Potential ΔC_L@10°
Flat Plate	0°	0.34	(baseline)	(baseline)
Apex Camber	+0.8°	0.28	-0.06	-.02
Conical Camber	+0.8°	0.30	-0.04	-.02

* with respect to flat plate portion of wing.

Thus the observed lift reductions at 10° angle of attack are substantially greater than would be expected from potential flow considerations. Evidently leading-edge camber reduces the vortex lift as well as the potential lift. Furthermore, vortex lift has a significant influence even at moderate angles of attack, for cambered highly-swept surfaces.

At high C_L's, the drag polars of the cambered models exhibit substantial reductions in drag due to lift compared to the flat plate. This is illustrated by the values given in Table 3.

Table 3 - Effect of Leading-Edge Camber on Drag

Model	C_L	C_D	Drag Reduction
Flat Plate	1.2	0.69	(baseline)
Apex Camber	1.2	0.61	12%
Conical Camber	1.2	0.64	7%

The reductions in drag shown are attributed to recovery of a portion of the thrust component of leading-edge suction as a direct consequence of cambering.

The slope of the flat plate $C_M - C_L$ curve (fig. 9) is about -.10 at low C_L values, indicating an aerodynamic center location of about .40$\bar{c}$. The curve indicates a less negative slope at C_L's above 0.4, reflecting a decrease in static stability. This is substantially below the stalling C_L value of 1.4.

The aerodynamic center location at low C_L's and the destabilizing trend at higher C_L's are both typical of slender delta wings (Ref. 13). Examination of figure 18 reveals a very strong influence of camber near the apex (constant percent chord camber) on pitching characteristics. The conically cambered model, on the other hand, has pitching characteristics nearly identical with the flat plate delta, prior to stall. The apex camber is apparently quite effective in overcoming the pre-stall destabilizing tendency. The importance of apex geometry in slender wing aerodynamics has been observed in previous studies of delta and double-delta wings (Refs. 12 and 14).

Leading-Edge Flap. - Based upon the favorable effects of apex camber versus conical camber, the flat plate model was modified to have a leading-edge flap with constant percent chord rather than either a constant chord or a "reverse taper" flap which would have approximated conical cambering. The constant percent chord flap approximates the camber of the NACA 230 mean lines utilized on the apex camber model.

In order to understand the effects of camber on angle of zero lift, the leading-edge flap configurations were analyzed theoretically utilizing the modified Multhopp computational routine in cooperation with Mr. John Lamar of NASA Langley Research Center (Ref. 2). It should be noted that the Multhopp method is only approximate for flapped wings, since the method does not account the discontinuity in surface slope at the flap hinge line. The results of the analysis are compared with experiment in Table 4.

Table 4 - Effect of Leading-Edge Flaps on Zero Lift Angle

	Zero Lift Angle	
δ_n	Theory	Present Tests
0°	0°	0°
12°	0.08°	0.3°
24°	0.15°	0.2°
36°	0.21°	0.4°
60°	0.44°	0.8°

The agreement between experiment and theory is reasonably good, with less than 0.4° maximum difference. It should be re-emphasized that these angles are measured with respect to the slope of the unflapped portion of the wing surface.

Figures 19 through 21 show the comparisons of lift curve, drag polar and the pitching moment curves of the apex camber wing with the flat plate wing with various amounts of leading-edge flap deflection. It is seen that the wing with $\delta_n = 36°$ behaves much like the apex camber delta, demonstrating that the performance and stability benefits of apex cambering can be achieved with rather simple variable leading-edge geometry.

Effects of Sideslip. - The variations of side force, rolling moment and yawing moment coefficients with sideslip angle at various angles of attack are shown in figures 22 through 24.

The curves are generally linear at low angles of attack (up to 10°) and become increasingly non-linear with increase in angle of attack.

The flat plate delta shows a large rolling moment at high angles of attack and sideslip, a result of the asymmetries in vortex strengths and positions. For cases in which the sideslip angle exceeds the complement of the leading-edge sweepback angle, the downwind "leading" edge becomes, in fact, a "trailing" edge and would not be expected to contribute to the vortex strength. Yawing moment and side force coefficients remain small. With cambered leading edges, substantial side force and yawing moments are developed as a result of forward facing area upon which thrust components of vortex-induced suction can be effective.

Recent work by Davenport and Huffman (Ref. 15) presents an analytical approach for predicting aerodynamic moments in sideslip, based upon the leading-edge suction analogy. This method appears quite promising, but has not yet been extended to include the effects of leading-edge camber.

Flow Visualization Studies

Composite Flow Field Results.- For analyzing complex flow field situations, a variety of experimental visualization techniques are available. Because each of several techniques has been found valuable for providing a particular type of information, three techniques were employed in the present investigations. A composite of typical results is shown in figure 25, along with a sketch of the flow field vortex sheets and typical streamlines. Interpretation of the flow evidence proceeds as follows:

a) The locus of minimum pressure points is determined from pressure distribution plots. These points correlate with the primary vortex core centers.

b) The water vapor traces give the locus of the primary vortex cores. Vortex bursting will be evidenced by an abrupt increase in core diameter.

c) Primary and secondary separation lines are readily apparent in the oilflow patterns, being marked by a pair of dark lines emanating from the apex.

d) The tuft patterns provide the best information as to reattachment of the leading-edge vortex sheet. This is evidenced by an abrupt change in direction of the tufts; the tufts inboard are nearly streamwise and those outboard of reattachment have a strong spanwise component.

The paragraphs which follow give detailed interpretations of the various visualization results.

Tuft Photos at Zero Sideslip. - Tuft photos of the upper surface flow patterns at zero sideslip are shown in figures 26 through 33. In this series the flat plate, apex cambered, and conically cambered models may be compared directly. At 10° angle of attack, the flat plate model shows a well-developed vortex flow with full reattachment inboard of the vortex. This is indicated by the steady, streamwise-pointed tufts in the center region of the wing, and the tufts which show an outboard deflection from about the 60% semi-span position outboard. The outboard deflection is caused by the velocities induced by leading-edge vortices. The apex camber model, on the other hand, appears to have attached flow up to about 30% chord with evidence of a separated flow aft of this position. From these photos, it appears that the apex camber model has no apex leading-edge separation at angles below 30°. This is in contrast to the flow patterns on the flat plate delta.

The conical camber delta at 10° angle of attack appears to have attached streamwise flow along the drooped extreme tip regions, with vortex flow developed inboard.

Oilflow Patterns at Zero Sideslip. - The surface flow patterns at zero sideslip are shown in figures 34 through 40. These patterns are characterized by a pair of lines emanating from the apex which are indicative of the secondary separation which occurs outboard of the leading-edge vortex core location. At $\alpha = 10°$ the flat plate and conical camber models exhibit a distinct secondary separation line, while the apex camber model

has a primary separation line near the apex (flow is attached at the apex leading edge), and a faint secondary separation line along the aft portion of the wing where vortices are present.

At higher angles of attack, the flat plate and conical camber model flow patterns retain their similarity, indicating that the basic leading-edge vortex patterns are not affected greatly by camber near the wing tip.

The separation lines for the apex camber model illustrate an interesting "kink" which appears at 20° angle of attack and is present up to 30° angle of attack. This peculiar behavior is believed to occur in the following way. The flow is attached at the apex leading edges, so that no vortices are formed in this region. As the flow follows the highly cambered apex region, primary separation takes place on the curved surface and the resulting separation stream-surface flows over the center portion of the wing, without reattachment.

The aft portion of the wing, being only very slightly cambered, exhibits separation at the edges at low angles and a pair of leading-edge vortices is formed, emanating from about the 50% chord location. These vortices pump air into the wing center section and induce reattachment of the flow beneath the vortices. The aft panel vortices are therefore presumed to be responsible for the kinked separation lines.

Water Vapor Patterns at Zero Sideslip. - The water vapor patterns shown in figures 41 through 47 were obtained by passing saturated steam through a 1/4" diameter copper tube attached to the models and fitted with a "tee" nozzle so that the steam was injected near the vortex cores. If the steam is injected very close to the center of the core, it becomes entrained and follows the core. Steam injected outside the core will be induced to coil about the core in a helical pattern. Thus after some preliminary experimentation, it was possible to determine a single location which gave satisfactory vortex core traces over the desired angle of attack range for the flat plate delta. The same technique was utilized for the cambered models, but with less satisfactory results. For these models the vortices do not increase in strength with distance from the apex in the same regular manner (theoretically linearly) as the flat plate delta, and vortex core definition becomes more difficult.

On the apex camber model, for example, at angles of attack below 20°, the vapor emitted was not entrained along the leading edges and hence does not mark a vortex type flow.

Comparison of the flat plate and conical camber model patterns, however, shows that they have essentially the same leading-edge vortex locations throughout the angle of attack range prior to bursting. Vortex "bursting" or "breakdown" is characterized by a rapid increase in core diameter and rapid turbulent diffusion within the core downstream from the bursting point. As a consequence, the water vapor may evaporate a short distance downstream from the bursting point, depending upon relative humidity and water vapor densities. Werle, (Ref. 16) has published a beautiful collection of photographs illustrating bursting phenomena as observed using colored dye traces in a water channel.

At $\alpha = 30°$, (Fig. 45) the flat plate model shows no bursting. The apex camber model exhibits bursting of both right and left panel vortices, at about the 75% chord location, and the conical camber model shows evidence of bursting on the right hand panel only.

Initial vortex bursting occured between 30° and 35° on the flat plate model. From the force data (fig. 7) the maximum C_L occurs at $\alpha = 35.5°$ to 37.5°, indicating a bursting angle in this range of values. From reference 12, the expected value of α at bursting would be 36°.

Thus the force data correlates very well with previous tests, but the steam photos indicate bursting at a slightly lower angle. It is believed that this discrepancy is due to increased tunnel upwash angle at the reduced dynamic pressure of the steam photo runs. Because of the rapid evaporation of the water vapor at high velocities, it was necessary to operate the tunnel at a greatly reduced speed ($q = 67$ newtons/m^2) for the steam photos. In any case, the amount of cambering utilized on the models of the present investigation was not responsible for a significant change in the initial vortex bursting boundary.

Effects of Sideslip on Vortex Patterns. - The effects of sideslip on the vortex flow patterns are illustrated by the series of tuft, oil flow and water vapor photos shown in figures 48 through 56. These tests were conducted at an angle of attack of 20° on all models, which corresponds to lift coefficients in the range of 0.7 to 0.8 for the models tested.

The oil flow patterns in this series for the flat plate model were obtained subsequent to cutting the model leading-edges to form nose flaps. The flaps were fitted with a set of brackets to permit zero camber, but the flap apexes had been removed to permit nose droop. Thus, the planform geometry was compromised slightly for this series, by the "notched" apex.

A general observation which is noted from examination of the oil flow photos is that the patterns developed on the flat plate and conical camber models are quite similar, while the patterns developed by the apex camber model are unique. For all models, as the yaw angle is increased, the secondary separation lines move toward the leading edge on the downwind edge and away from the leading edge on the upwind edge. At 30° sideslip condition, the vortex formed by the upwind edge is now located at nearly the mid-span location, while the downwind edge vortex does not produce sidewash on the upper surface, as evidenced by examination of the oil streak and tuft photos. The water vapor photos, on the other hand, show rather clearly that the downwind vortex is still present, but located well outboard of the wing leading edge, in a dir ction nearly streamwise. The "downwind leading edge" has in fact become a "trailing edge", as a result of the high sideslip angle.

The water vapor photo of the flat plate model at 10° sideslip (fig. 54) illustrates how sideslip influences bursting. Vortex bursting occurs at a lower angle of attack on the upwind edge with its lower effective sweep. Vortex bursting is delayed, on the other hand, on the downwind edge where the effective sweep has been increased. These results are in agreement with the observations of Hummel (Ref. 17).

The large vortex movements and changes in vortex strengths and in angle of attack for bursting noted above would be expected to give rise to strongly non-linear aerodynamic force and moment data as discussed in the section on force measurements.

With the apex camber model water vapor photos of this series a difficulty occurred which had been encountered with the pitch series for this model. The water vapor nozzle outlet does not always coincide with the vortex core location. This is illustrated by comparing the tuft and water vapor patterns of figure 48 and figure 54. The tufts indicate a vortex on the right wing panel, but the water vapor is streaming to the left. This is a result of the downwind vortex originating at the apex, while the other vortex seems to originate at near mid chord.

The characteristics of the flow fields in sideslip may be summarized as follows:

1) The vortices tend to assume a more nearly streamwise direction.

2) Bursting occurs asymmetrically in sideslip, with the upwind edge being more susceptible to bursting.

3) Conical cambering has little effect on the vortex field in sideslip, while apex cambering tends to give rise to premature bursting.

Cross-Flow Water Vapor Patterns. - A few photos were taken of the cross-flow vortex patterns. These were obtained by mounting a camera behind the wing trailing edge, and illuminating the water vapor with a slit of light perpendicular to the vortex cores. By successively positioning the light at various chordwise stations, the vortex development may be observed. A composite of such photos for a single angle of attack is shown in figure 57.

Surface Pressure Distributions

Zero Sideslip Case. - The pressure distributions over the wings at angles of attack up to 40° with zero sideslip are shown in figures 58 through 69. The flat plate wing exhibits the upper surface suction peaks located slightly inboard from the leading edges, as is characteristic of vortex flows. It is seen that the conical camber wing behaves very much like the flat plate wing. Evidently the leading-edge vortices, once formed, are not influenced greatly by conical camber. In contrast to this, the apex camber model exhibits a large reduction in suction near the apex, and a corresponding aft shift of the longitudinal pressure peak. All the wings exhibit two spanwise pressure peaks at the rear chordwise stations. This is attributed to the formation of a secondary vortex very close to the leading-edge.

Longitudinal Load Distribution. - Spanwise pressure integrations on the flat plate delta wing were carried out at each chordwise station to obtain a local normal force coefficient defined in the following way:

$$C_{N_L} \equiv \frac{\int_{-a}^{a} \Delta C_p \, dy}{b/2} . \qquad \text{(Equation 2)}$$

This integration is carried out numerically by summing the pressure difference over the panels in the spanwise direction:

$$C_{N_L} = \sum_{i=1}^{n} \Delta C_{Pi} \, \Delta(2y_i/b) . \qquad \text{(Equation 3)}$$

The results of these integrations are presented in figure 70. These results are compared to results from other sources (Refs. 18 and 19) at $\alpha = 20°$ in figure 71.

Integrated Force Data. - Total pressure forces were also obtained by C_p integration over the entire surface. Figures 72 through 74 show the comparisons of the integrated pressure forces with the measured force data for the flat plate. For these comparisons, the angle of attack and drag coefficient have been corrected for wind tunnel wall effects. (See Appendix C, Ref. 9, for details.) The lift and drag due to lift compare quite favorably. The pitching moments calculated from pressure integrations compared quite favorably with measured pitching moments, with the exception of one point near the vortex bursting angle of attack.

Effects of Sideslip on Pressure Distributions. - Pressure distributions for the three wings in sideslip are shown in figures 75 through 77. As expected, the pressure peak of the leading wing panel moves inboard and the pressure peak of the trailing wing panel moves outboard, resulting in an asymmetric loading. At large sideslip angles the balance housing on the pressure side of the wings is responsible for a slight buildup of pressure on the upwind side and reduced pressure on the downwind side of the housing.

Combined Flow Field Results

Results from oil streak patterns, water vapor patterns and pressure distributions are combined in figures 78 through 80. This series illustrates how the suction pressure peaks are located beneath the vortex cores, and the secondary separation lines are located just outboard of the vortex cores.

CONCLUSIONS

1. Leading-edge vortices play a dominant role in the forces developed by slender wings with camber as well as uncambered wings.

2. While it is not yet possible to predict camber effects quantitatively from a theoretical standpoint, the qualitative effects are predictable from observations of the leading-edge vortex development and particularly the positions of the leading-edge vortices as a function of angle of attack, angle of sideslip and camber of the wing surface.

3. Leading-edge camber has only a slight effect on angle of zero lift and total lift for slender sharp-edged wings at high angle of attack. Leading-edge camber does produce some reduction in drag due to lift at high angles.

4. Slender wing pitching moment characteristics are strongly influenced by leading-edge camber. Camber near the apex is especially effective in alleviating the destabilizing tendency common to uncambered slender wings at high angles of attack.

5. Pitching moment and drag improvements with a simple hinged leading-edge flap with constant percent chord were similar to those achieved with a curved apex cambered surface.

Aeronautical Engineering Department
Wichita State University
Wichita, Kansas

REFERENCES

1. Multhopp, H.: Methods for Calculating the Lift Distribution of Wings. R & M 2884, British ARC, Jan., 1950.

2. Lamar, John E.: A Modified Multhopp Approach for Predicting Lifting Pressures and Camber Shape for Composite Planforms in Subsonic Flow. NASA TN D-4427, 1968.

3. Wagner, Siegfried: On the Singularity Method of Subsonic Lifting Theory. AIAA Paper No. 69-37, 1969.

4. Polhamus, Edward C.: A Concept of the Vortex Lift of Sharp Edge Delta Wings Based on Leading Edge Suction Analogy. NASA TN D-3767, Dec., 1966.

5. Mechtly, E.A.: The International System of Units - Physical Constants and Conversion Factors (Revised). NASA SP-7012, 1969.

6. Abbott, I. H.; and Van Doenhoff, A. E.: Theory of Wing Sections. Dover Publications, 1958.

7. Blackwell, J. A., Jr.: Preliminary Study of Effects of Reynolds Number and Boundary Layer Transition Location on Shock-Induced Separation. NASA TN D-5003, January 1969.

8. Stahl, W.; Hartmann, K.; and Schneider, W.: Force and Pressure Measurements on a Slender Delta Wing at Transonic Speeds and Varying Reynolds Numbers. AGARD Specialists Meeting on "Facilities and Testing at Transonic Speeds and High Reynolds Number." AVA Gottingen, 1971.

9. Wentz, W. H., Jr.: Effects of Leading-Edge Camber on Low-Speed Characteristics of Slender Delta Wings - Techniques and Tabulated Data. NASA CR-112016, 1972.

10. Razak, K.; and Snyder, M. H.: A Review of the Planform Effects on the Low-Speed Aerodynamic Characteristics of Triangular and Modified Triangular Wings. NASA CR-421, April, 1966.

11. Polhamus, E. C.: Application of the Leading-Edge Suction Analogy of Vortex Lift to the Drag Due to Lift of Sharp-Edge Delta Wings. NASA TN D-4739, August 1968.

12. Wentz, W. H.; and Kohlman, D. L.: Vortex Breakdown on Slender Sharp-Edged Wings. AIAA Journal of Aircraft, Vol. 8, No. 3, March, 1971.

13. Shanks, Robert E.: Low-Subsonic Measurements of Static and Dynamic Stability Derivatives of Six Flat-Plate Wings Having Leading-Edge Sweep Angles of 70° to 84°. NASA TN D-1822, July, 1963.

14. Wentz, W. H.; and McMahon, M. C.: Further Experimental Investigations of Delta and Double Delta Wings Flow Fields at Low Speeds. NASA CR-714, February, 1968.

15. Davenport, E. E.; and Huffman, J. K.: Experimental and Analytical Investigation of Subsonic Longitudinal and Lateral Aerodynamic Characteristics of Slender Sharp-Edge 74° Swept Wings. NASA TN D- 6344, July 1971.

16. Werle, H.: Sur L'Eclatement Des Tourbillons. O.N.E.R.A. (France) Tech Note No. 175, 1971.

17. Hummel, D.: Untersuchungen uber das Aufplatzen der Wirbel an Schlanken Deltaflugeln. Z Flugwiss, 13 (1965), Heft 5.

18. Kirkpatrick, D. L. I.: Analysis of the Static Pressure Distribution on a Delta Wing in Subsonic Flow. R & M No. 3619, British ARC, 1970.

19. Nangia, R. K.; and Hancock, G. J.: Delta Wings with Longitudinal Camber at Low Speed. ARC 31 588 (Queen Mary's College), 1969.

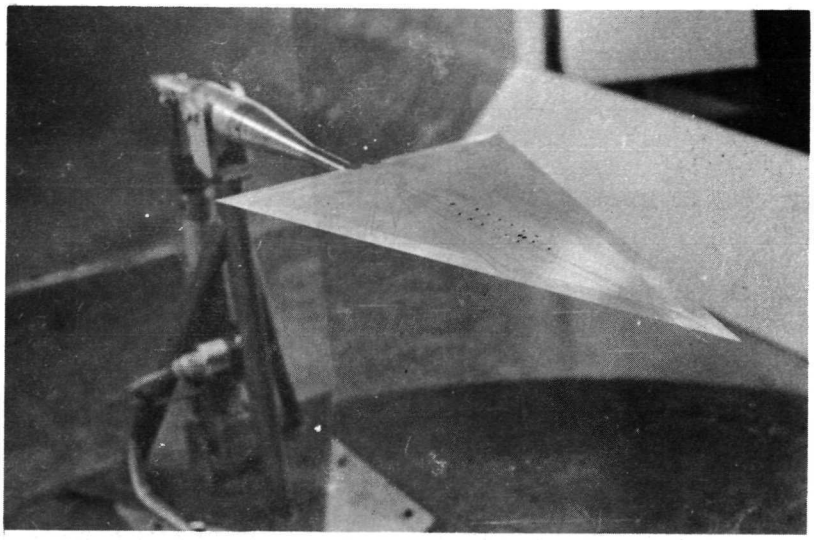

(a) Model and Support Stand

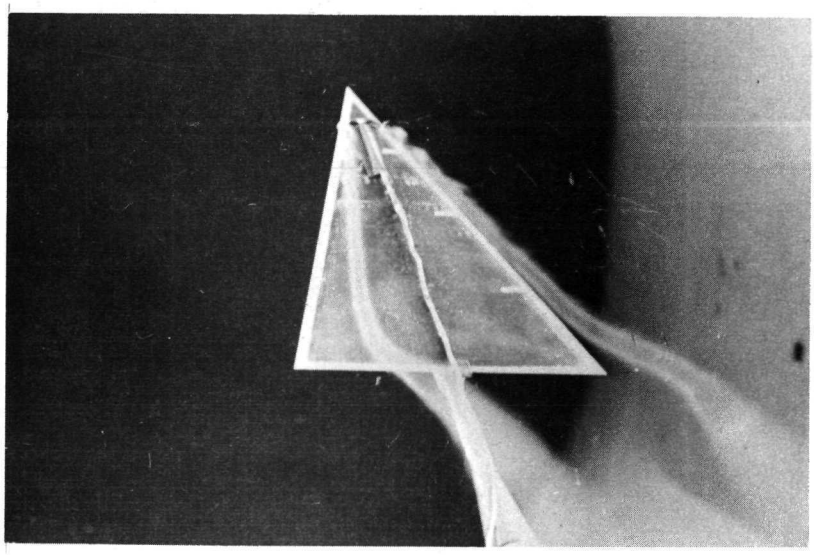

(b) Water Vapor Vortices

Figure 1 - Model Installation

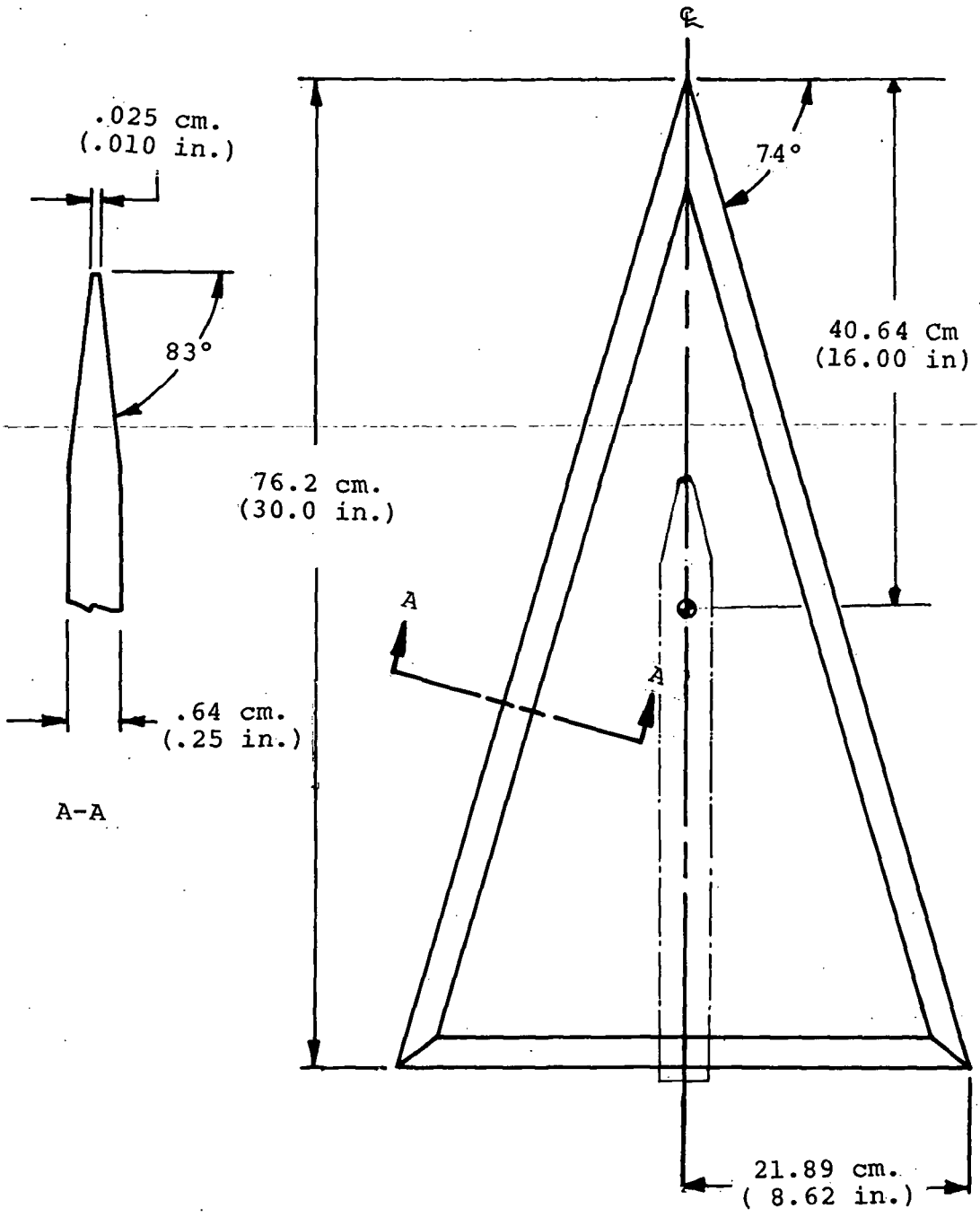

Figure 2 - Model Geometry - Flat Plate Delta Wing

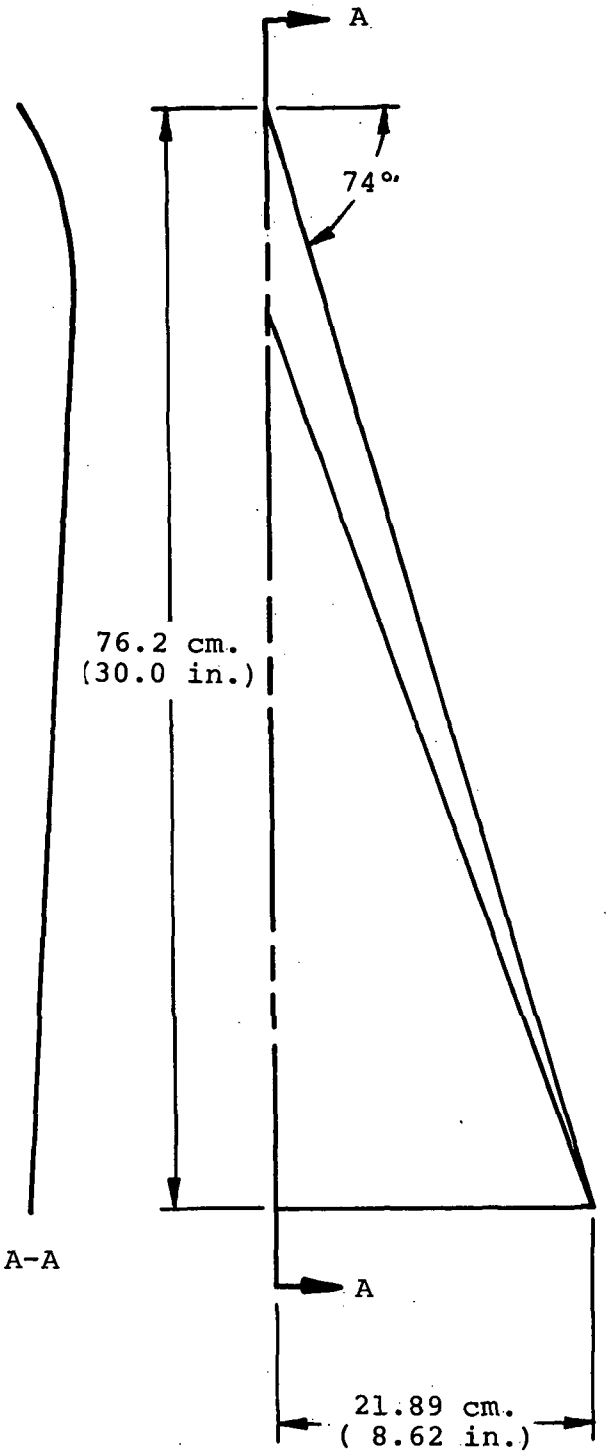

Figure 3 - Model Geometry - Apex Camber Delta Wing

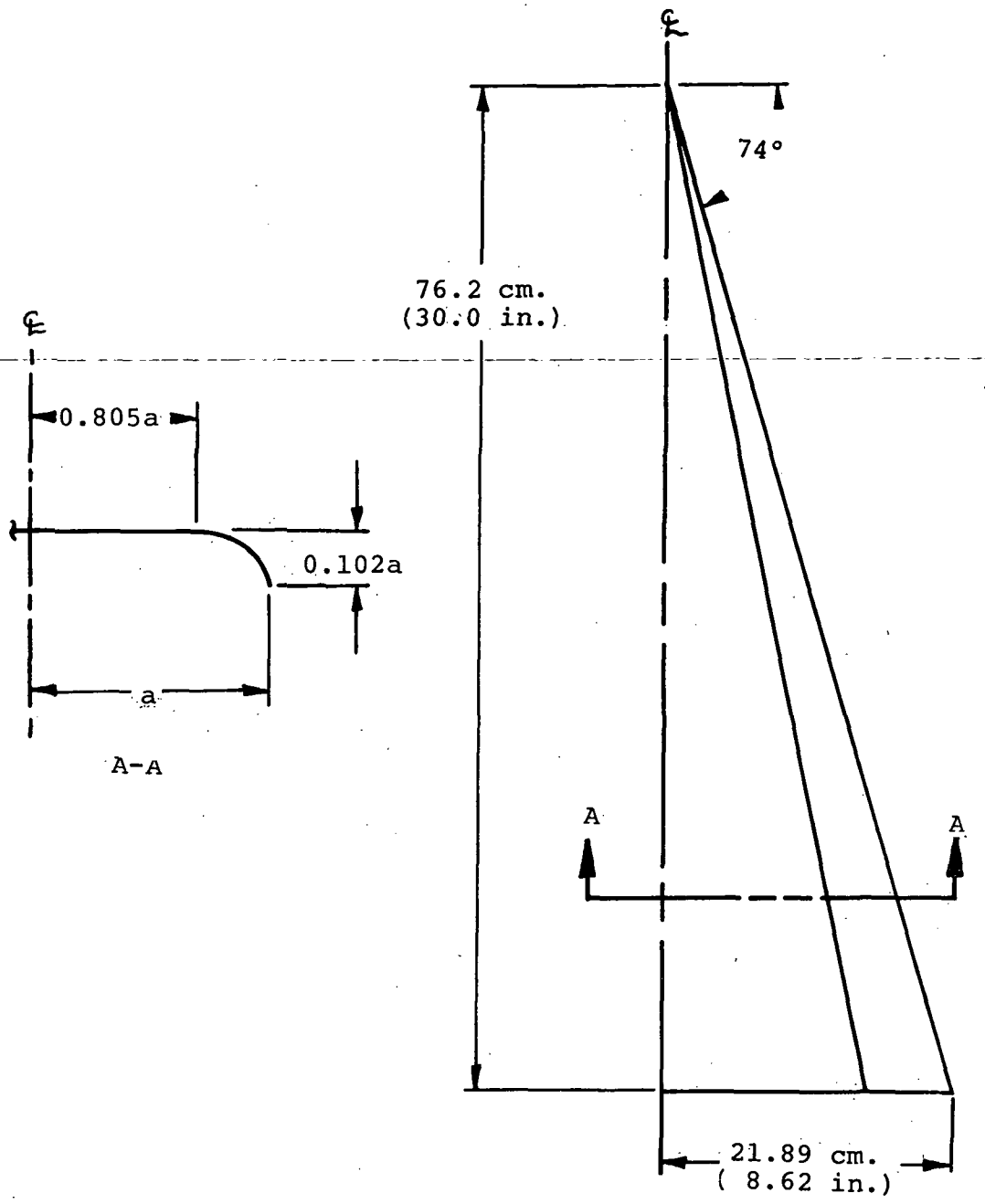

Figure 4 - Model Geometry - Conical Camber Delta Wing

× Upper Surface

⊙ Lower Surface

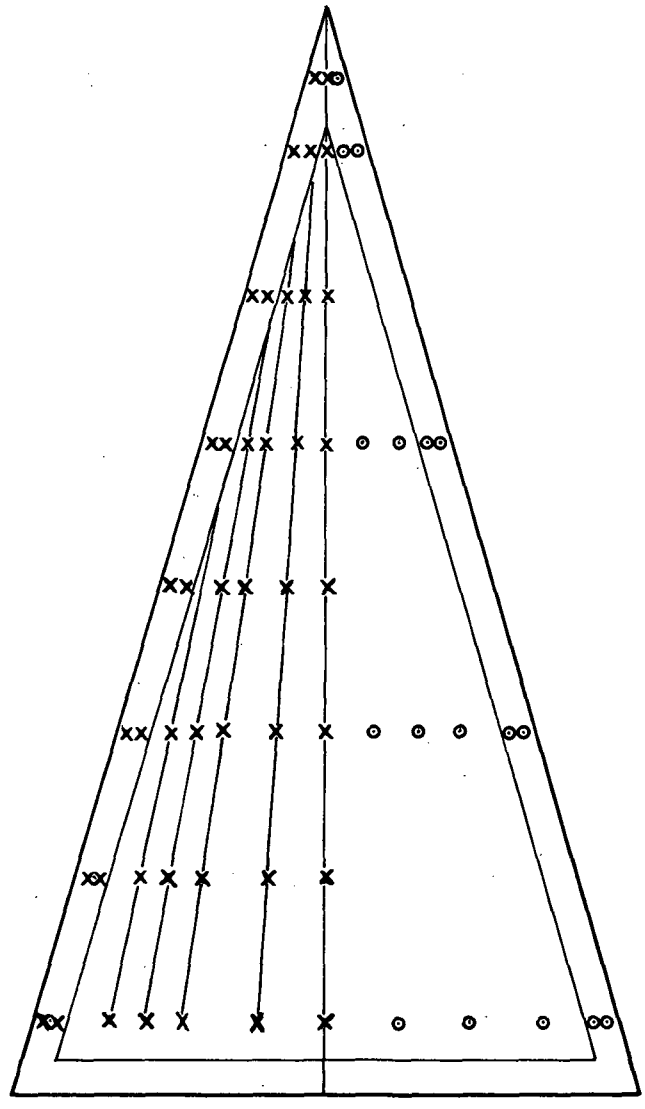

Figure 5 - Pressure Tap Locations

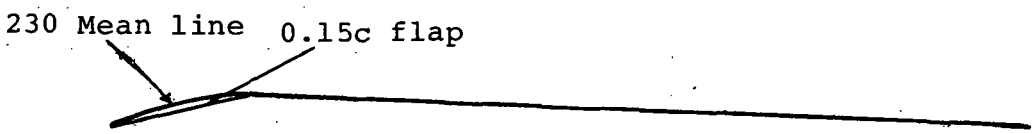

Mean lines

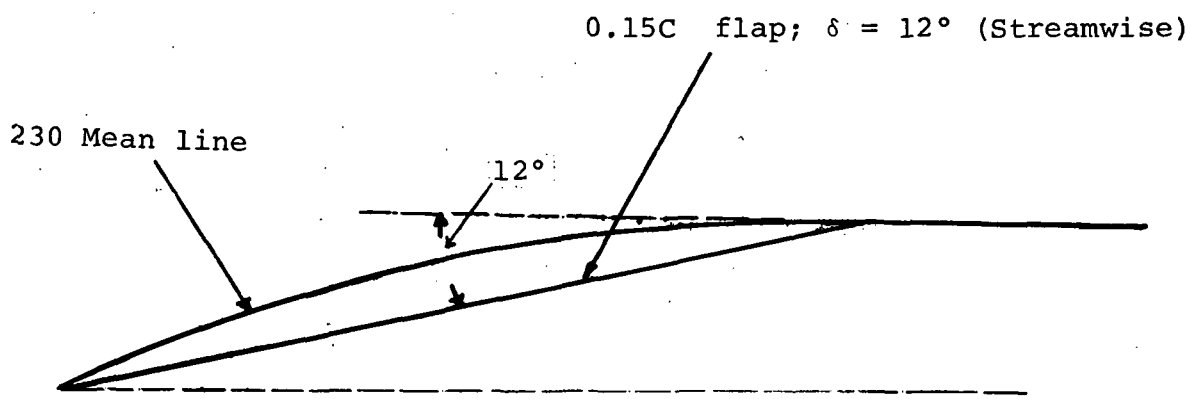

Details of Leading Edge

Figure 6 Geometry of mean line and leading edge flap.

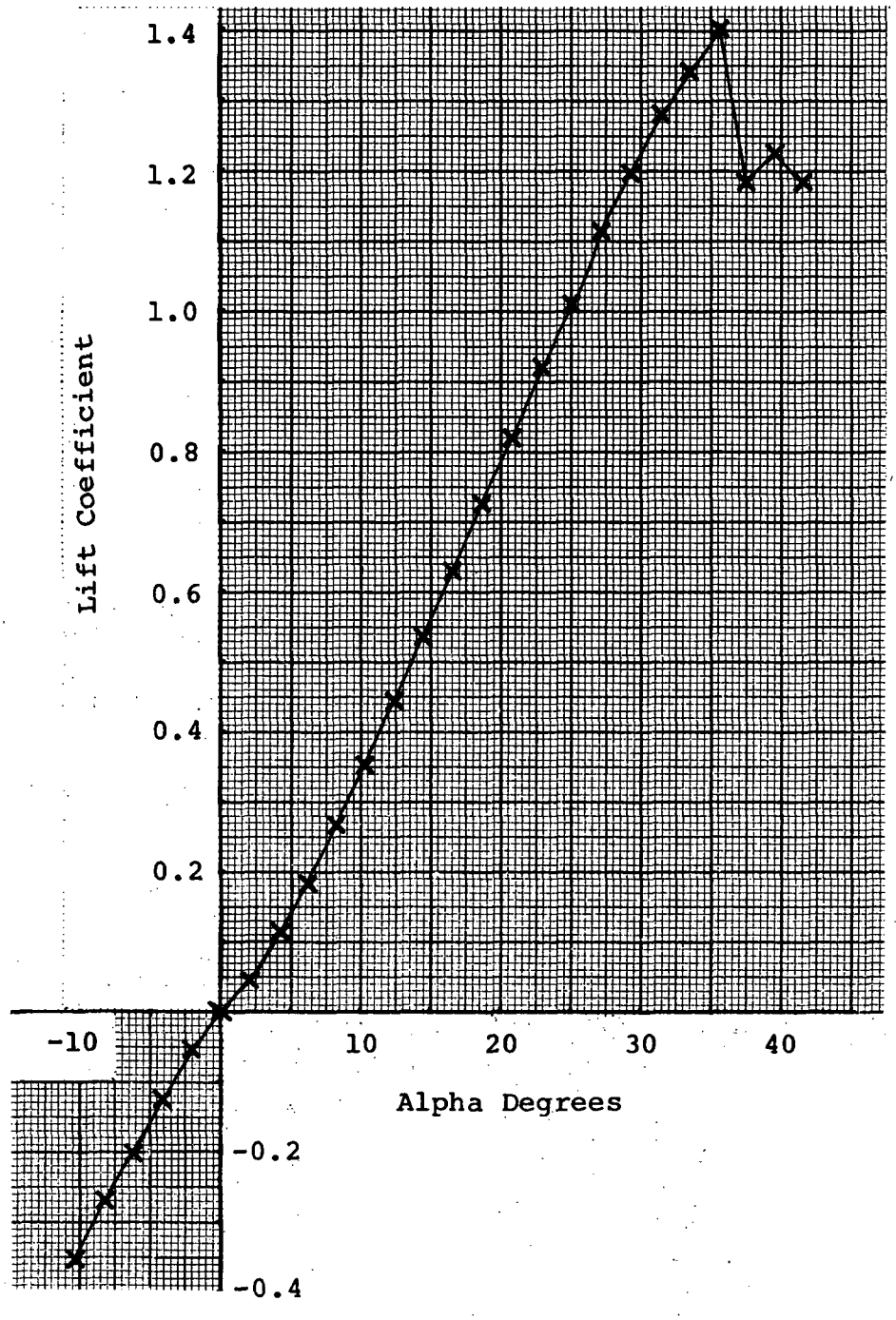

Figure 7 - Lift Characteristics - Flat Plate Model

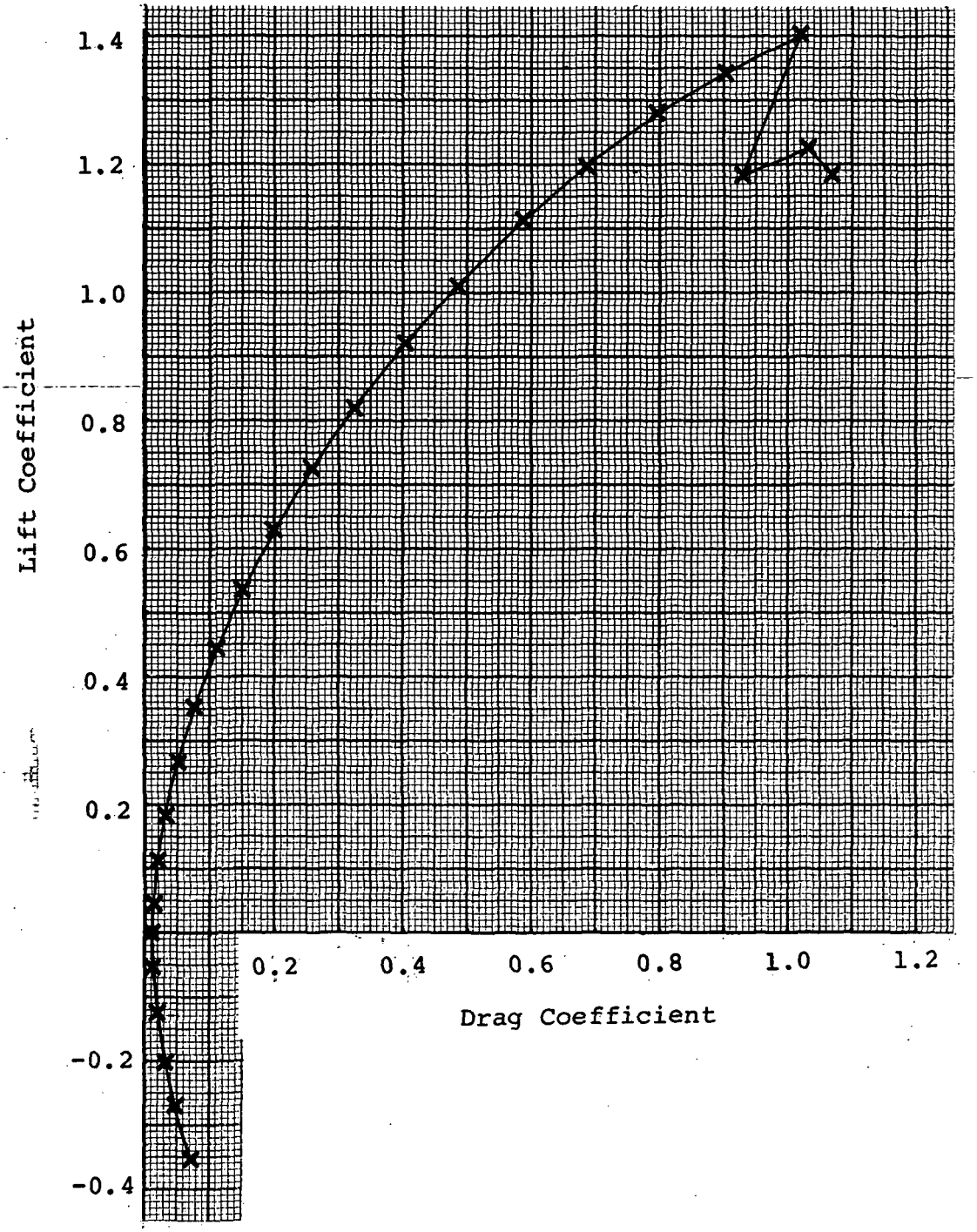

Figure 8 - Drag Characteristics - Flat Plate Model

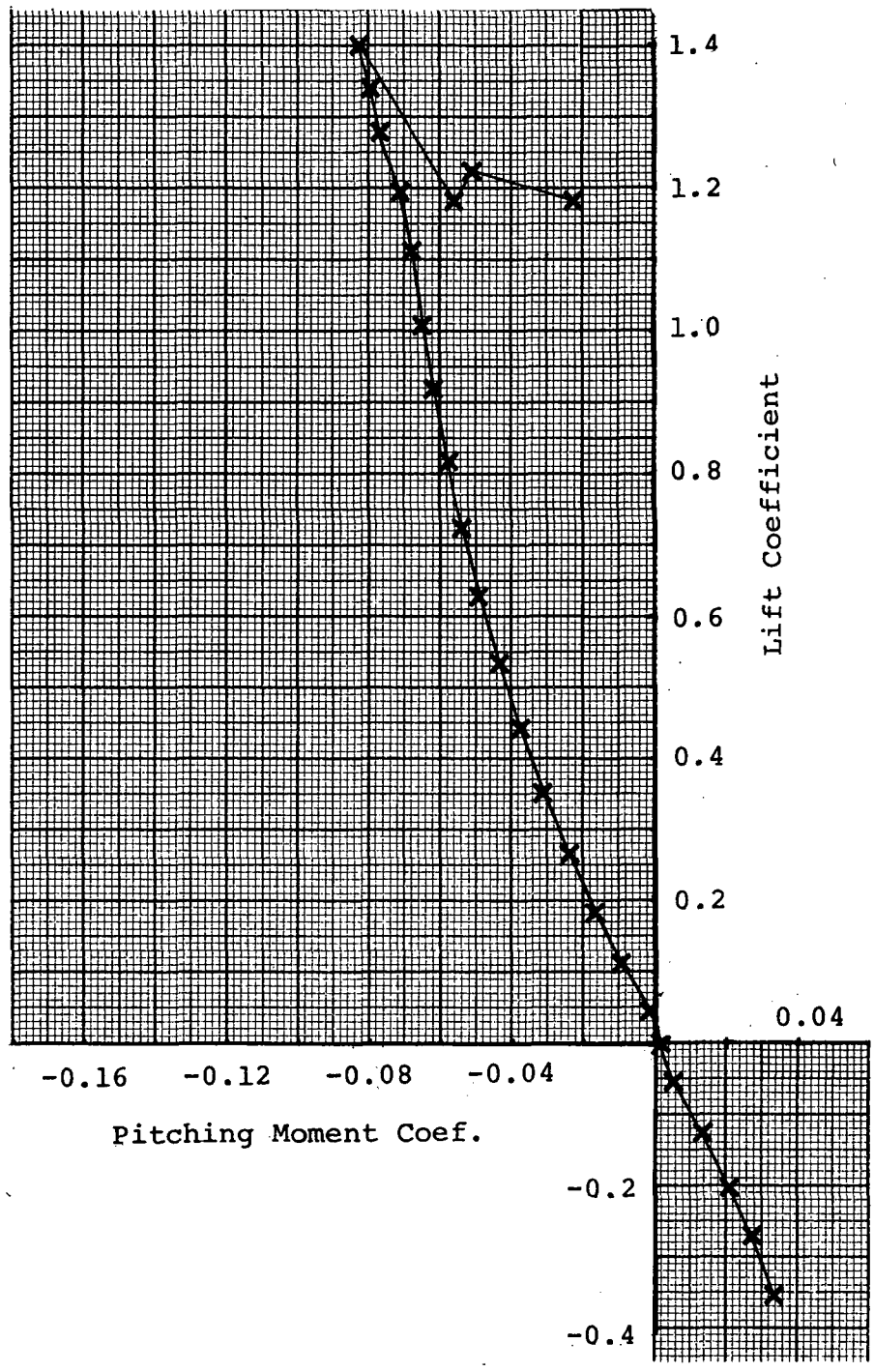

Figure 9 - Pitching Characteristics - Flat Plate Model

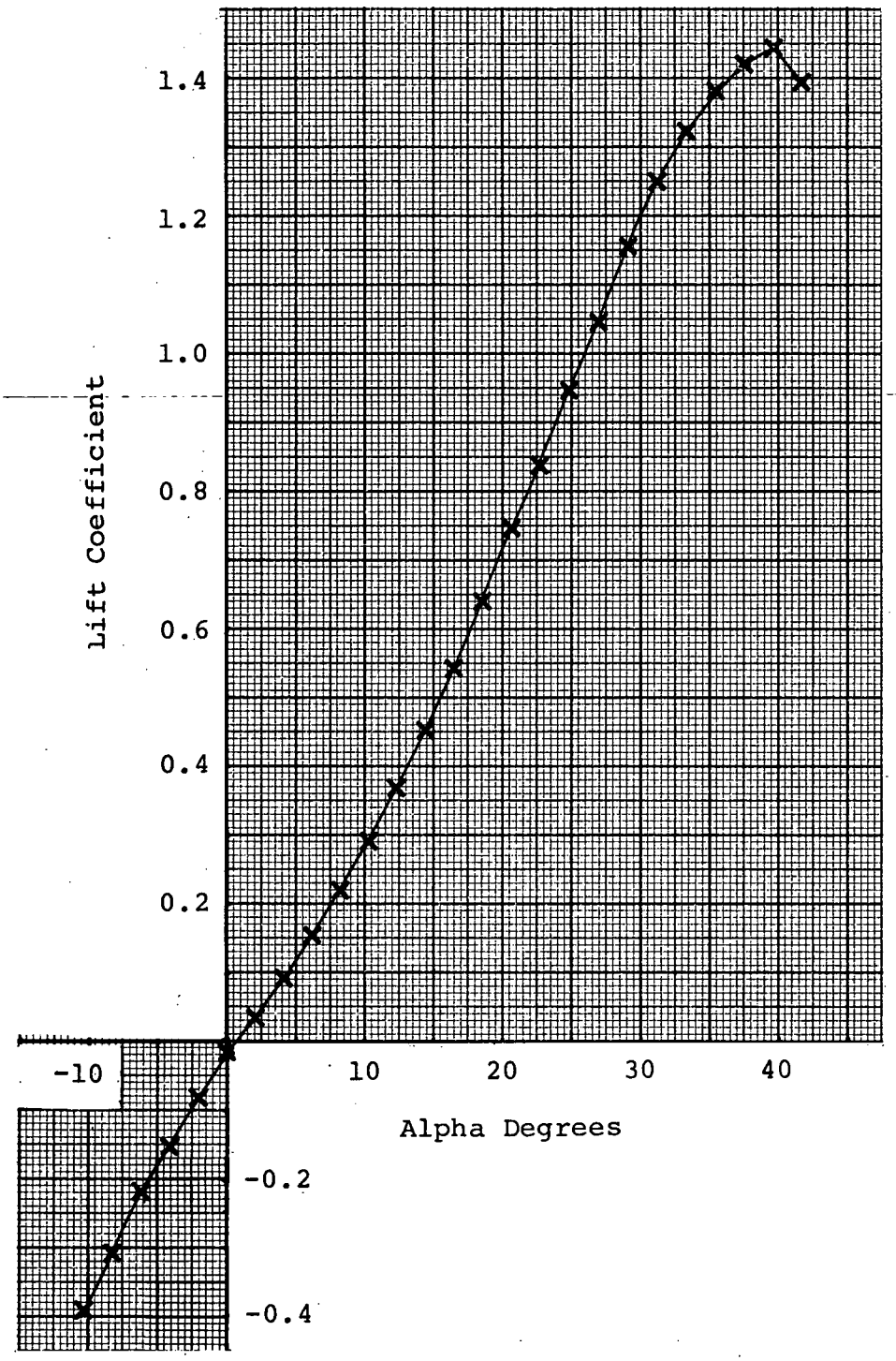

Figure 10 - Lift Characteristics - Apex Camber Model

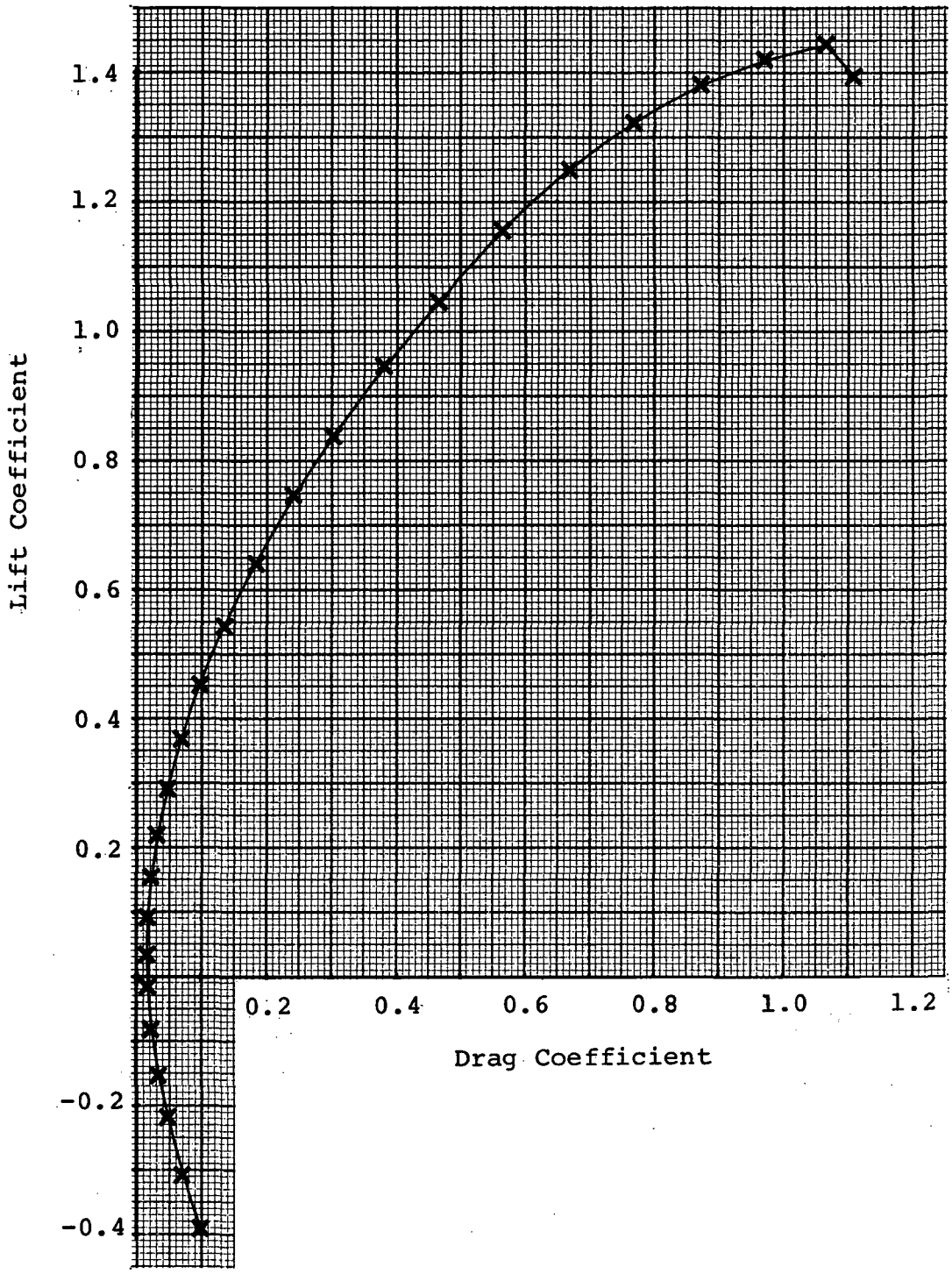

Figure 11 - Drag Characteristics - Apex Camber Model

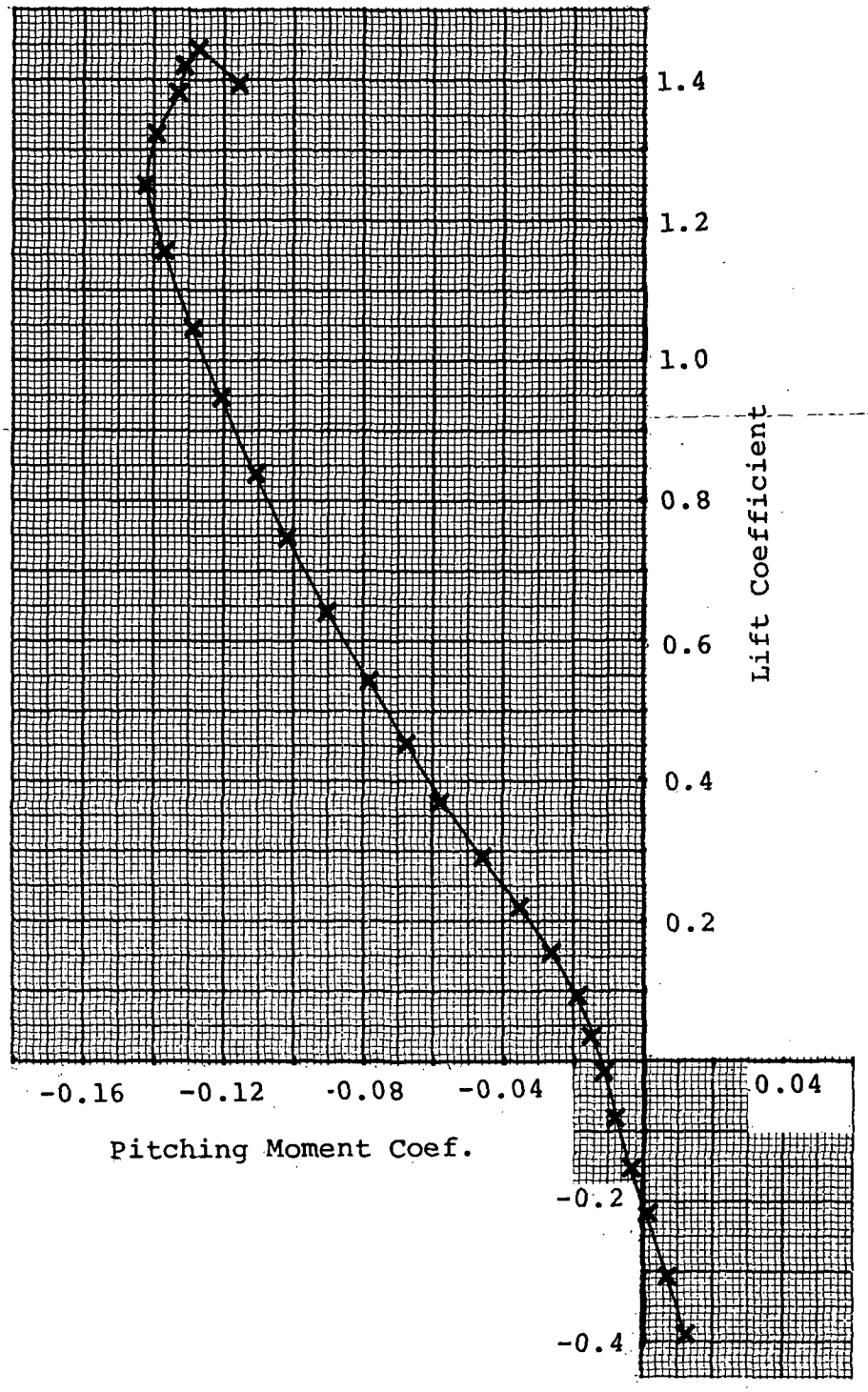

Figure 12 - Pitching Characteristics - Apex Camber Model

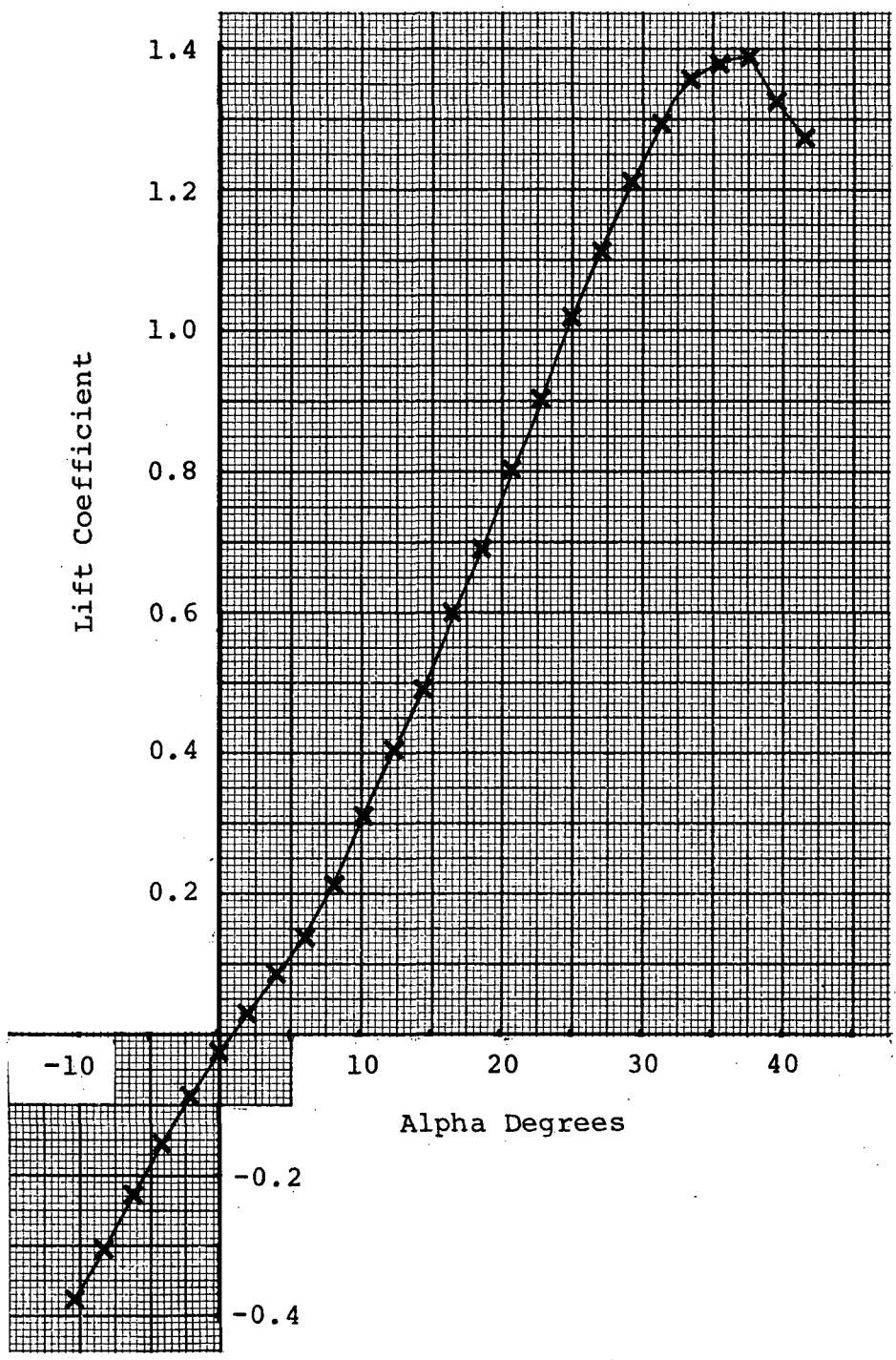

Figure 13 - Lift Characteristics - Conical Camber Model

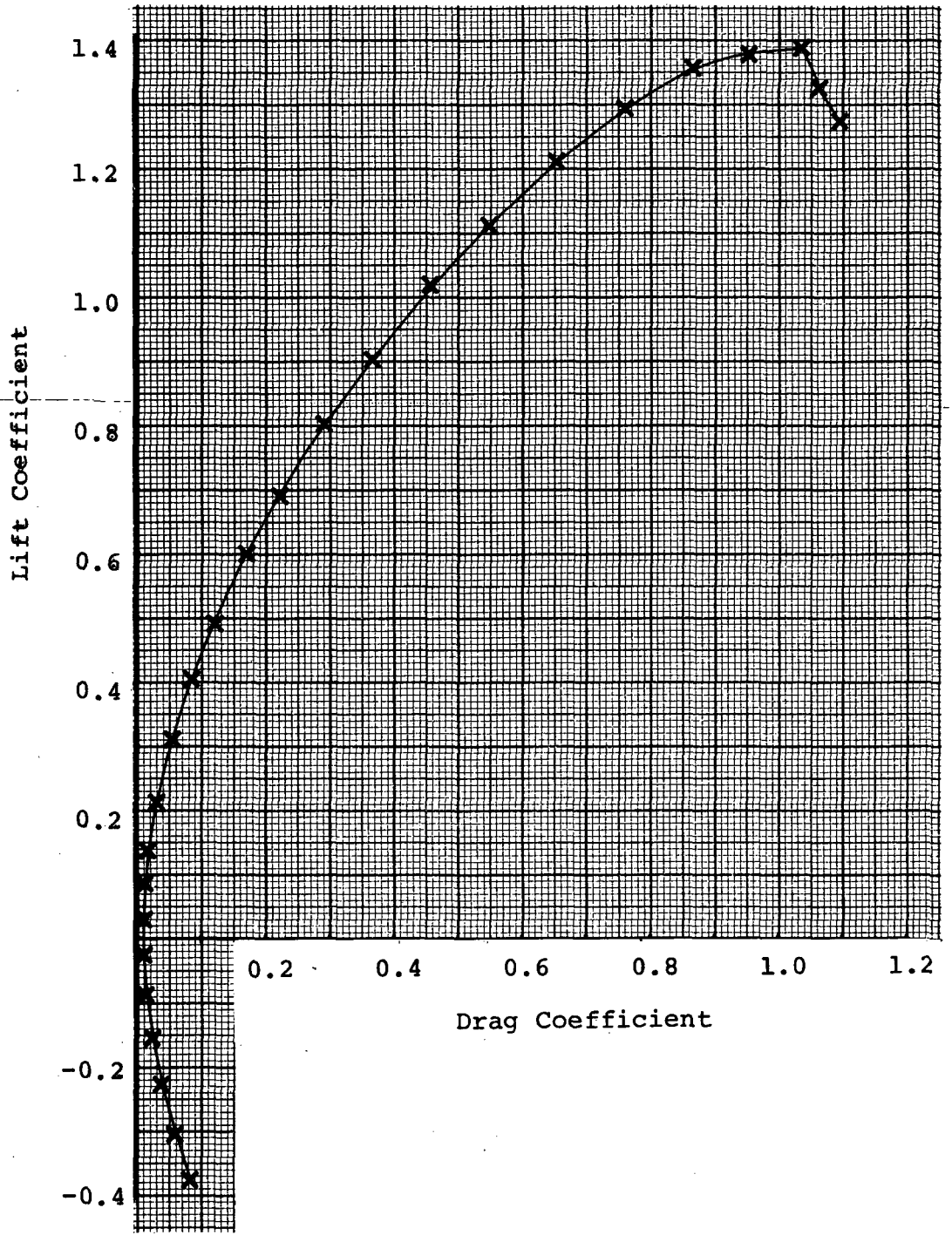

Figure 14 - Drag Characteristics - Conical Camber Model

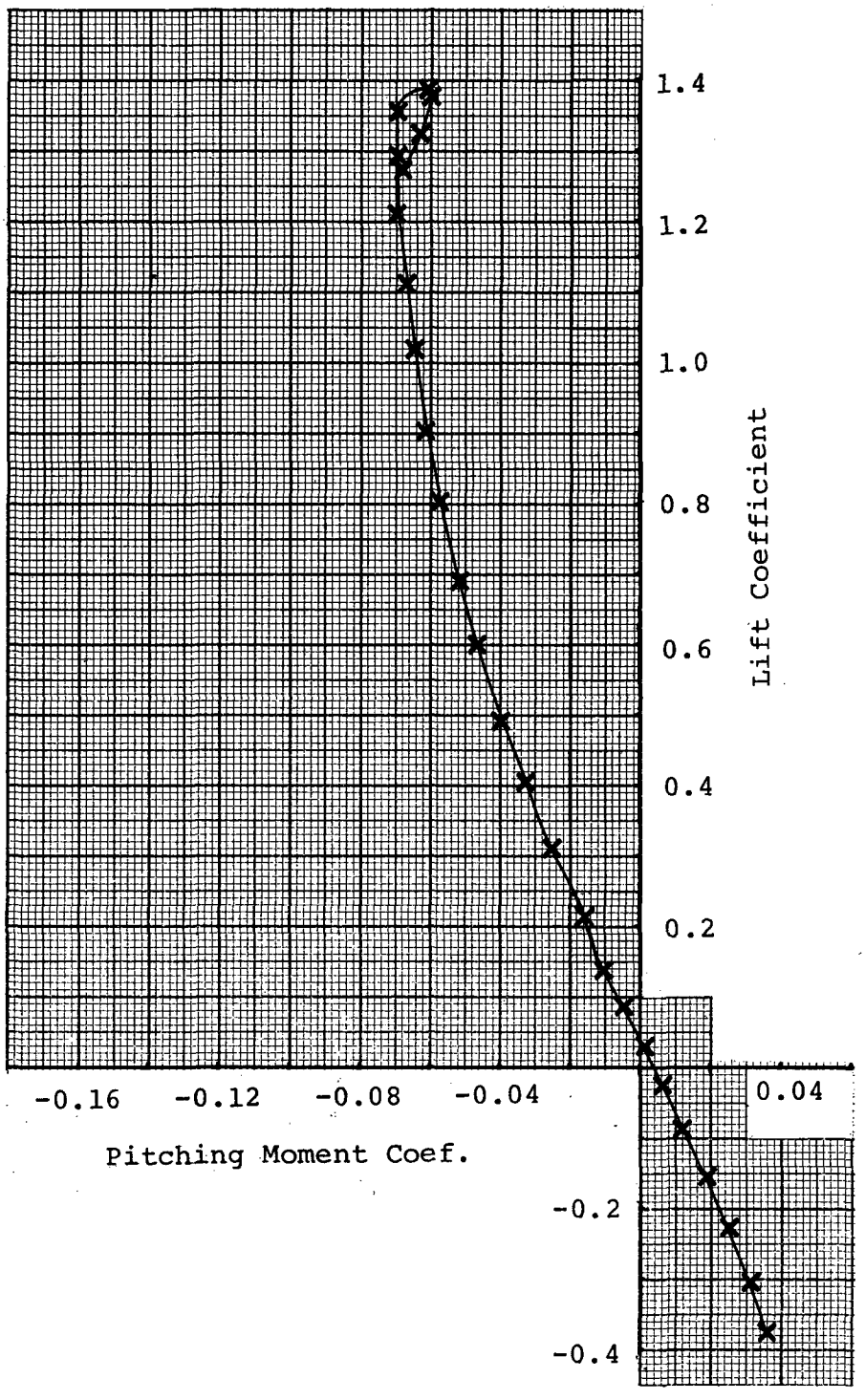

Figure 15 - Pitching Characteristics - Conical Camber Model

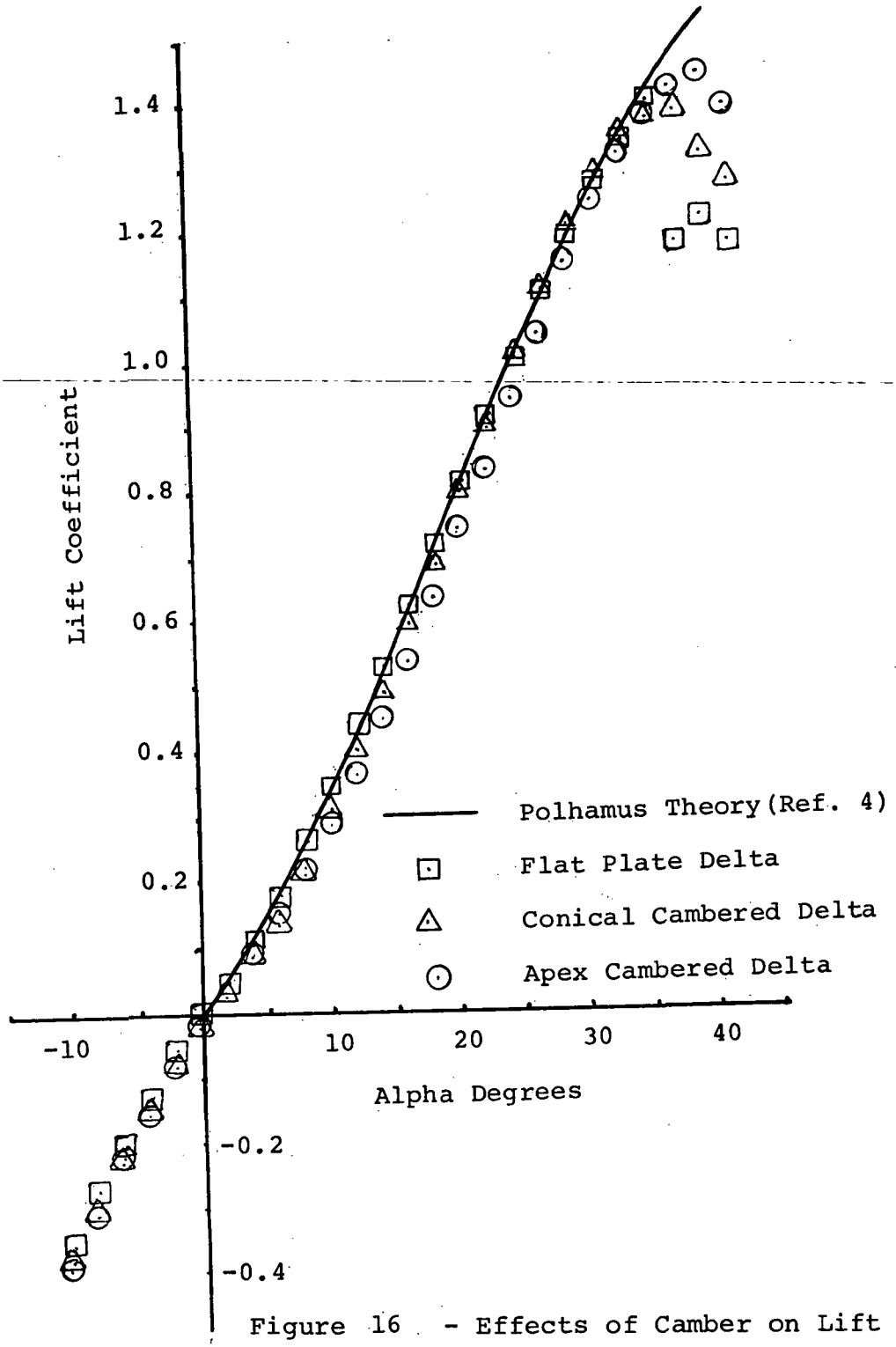

Figure 16 - Effects of Camber on Lift

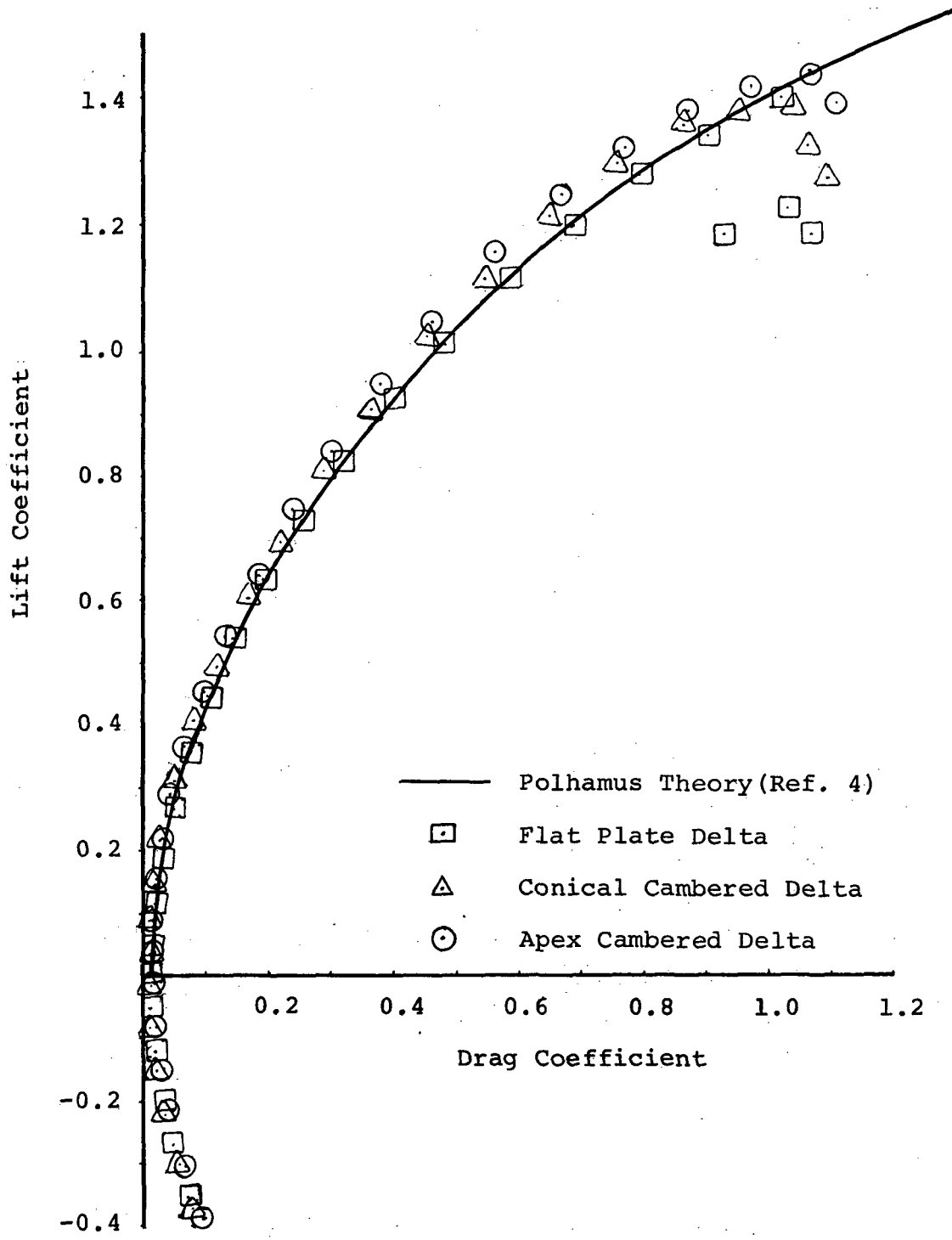

Figure 17 - Effects of Camber on Drag

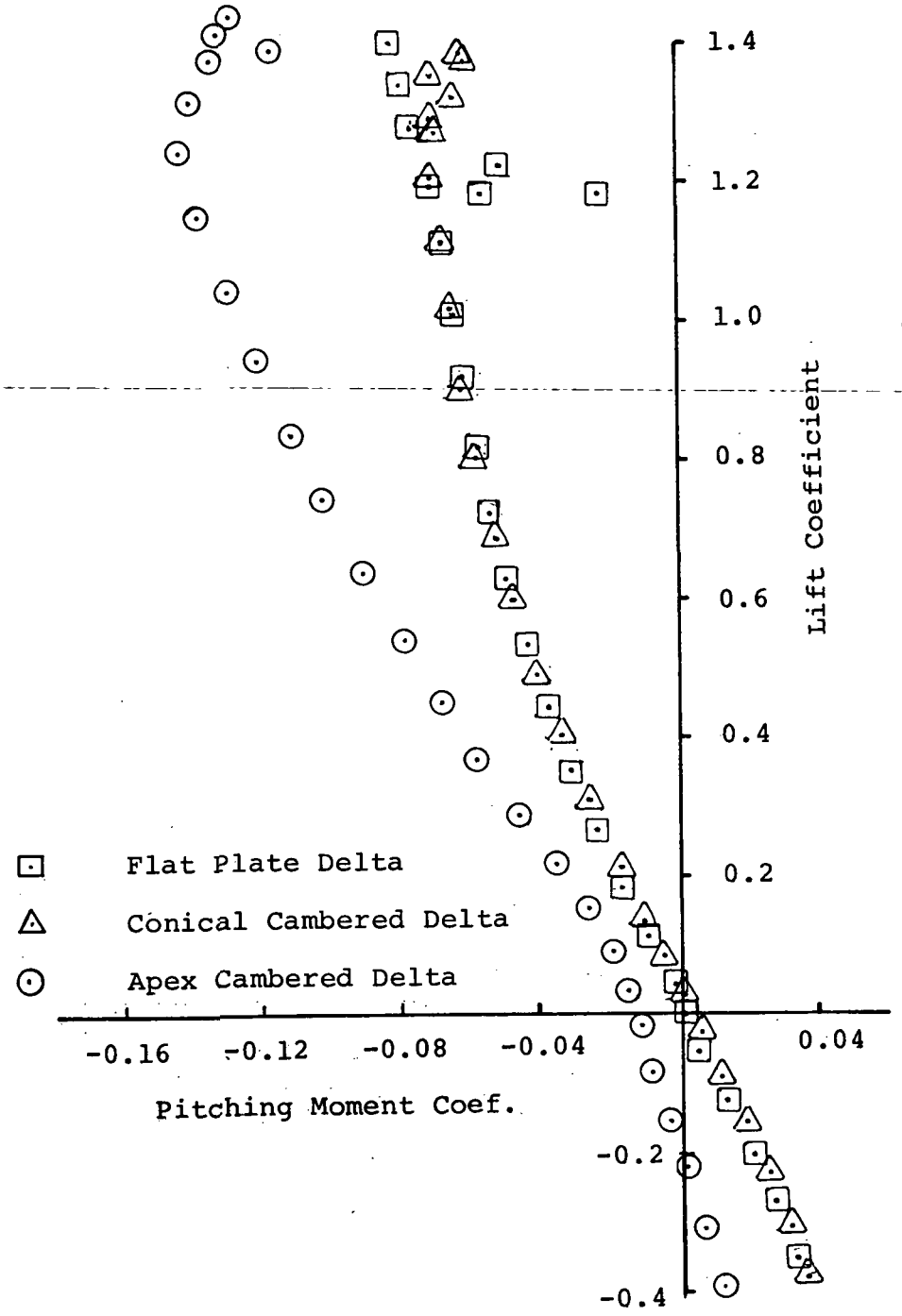

Figure 18 - Effects of Camber on Pitching Characteristics

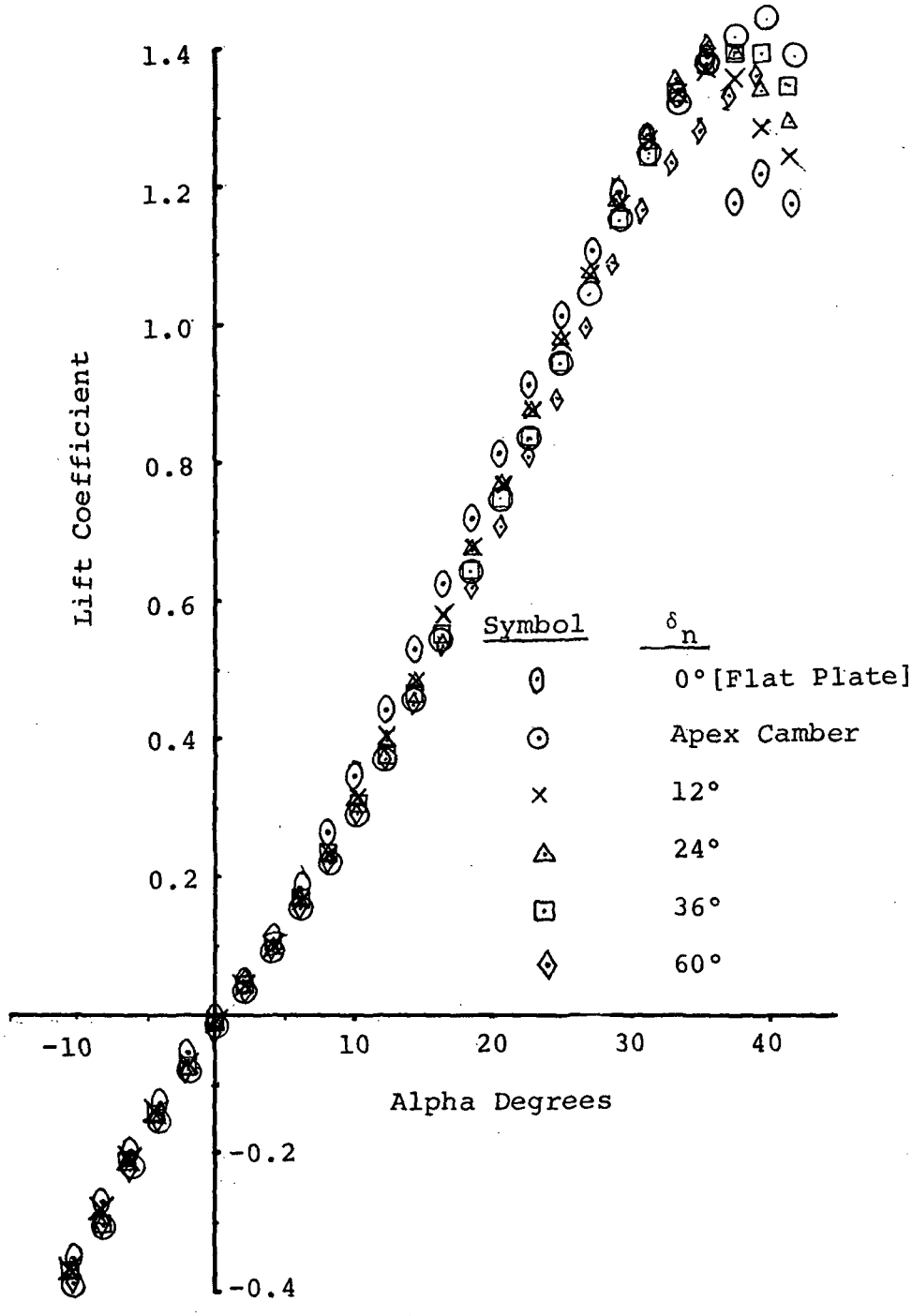

Figure 19 - Effects of Leading-Edge Flaps on Lift

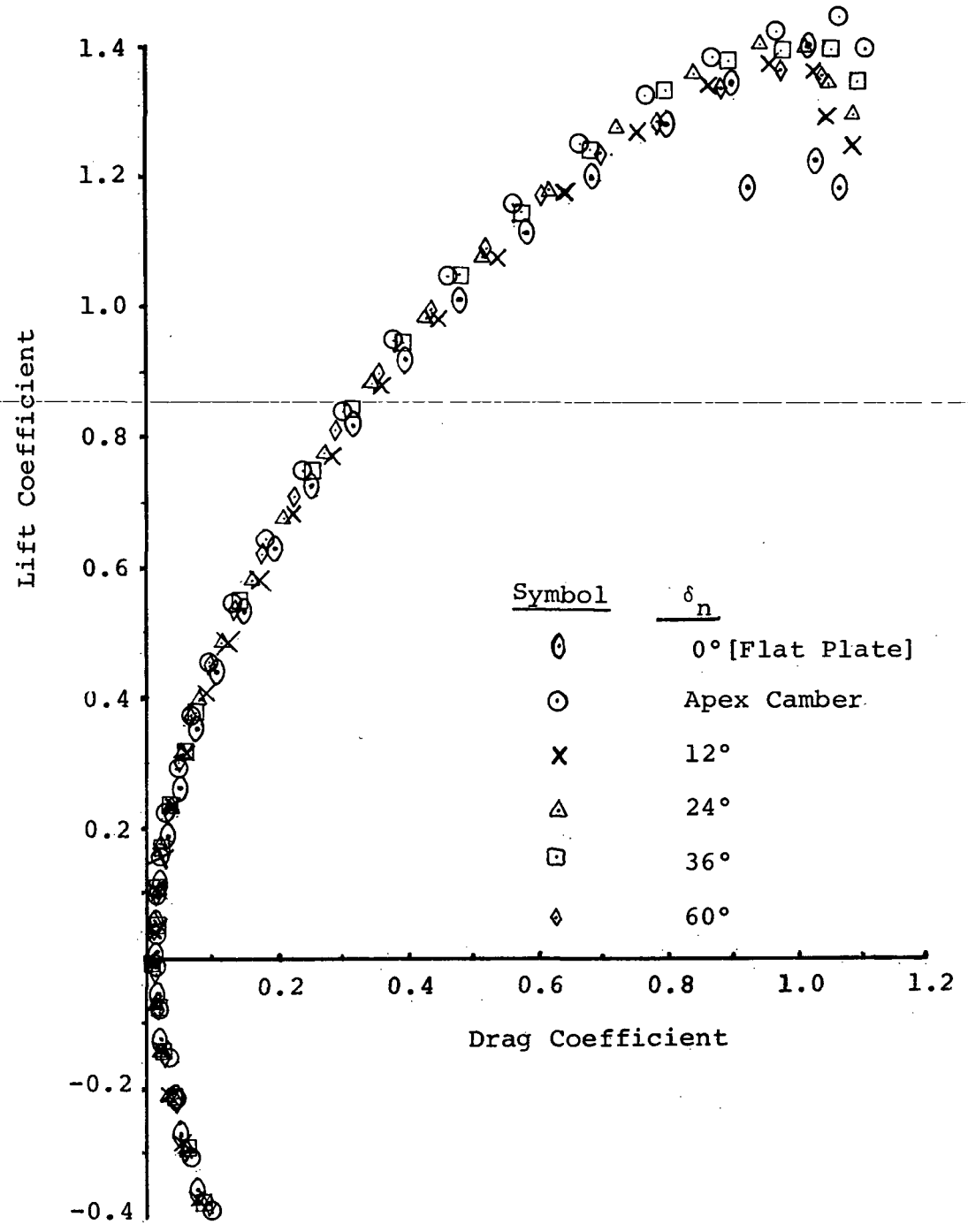

Figure 20 - Effects of Leading-Edge Flaps on Drag

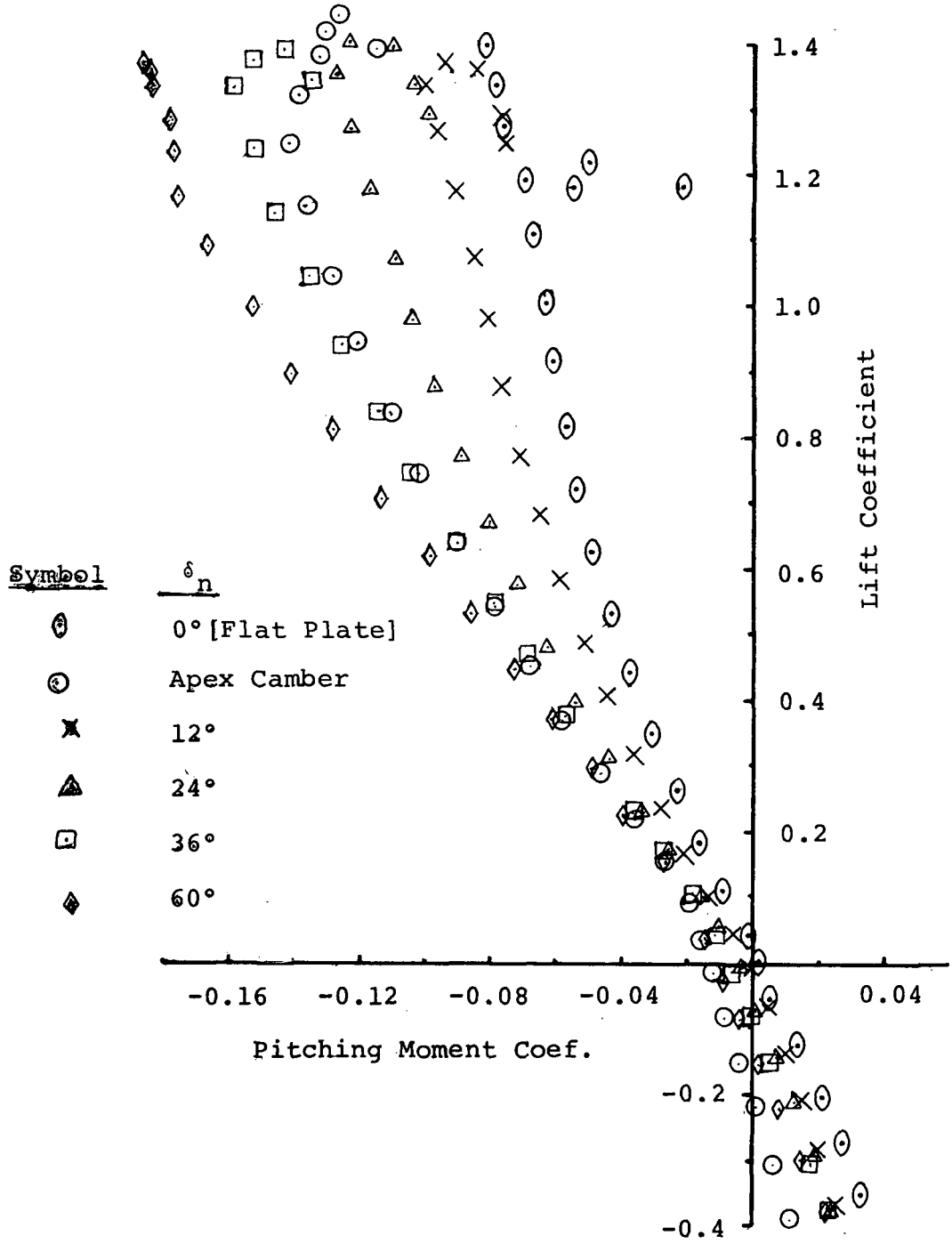

Figure 21 - Effects of Leading-Edge Flaps on Pitching Characteristics

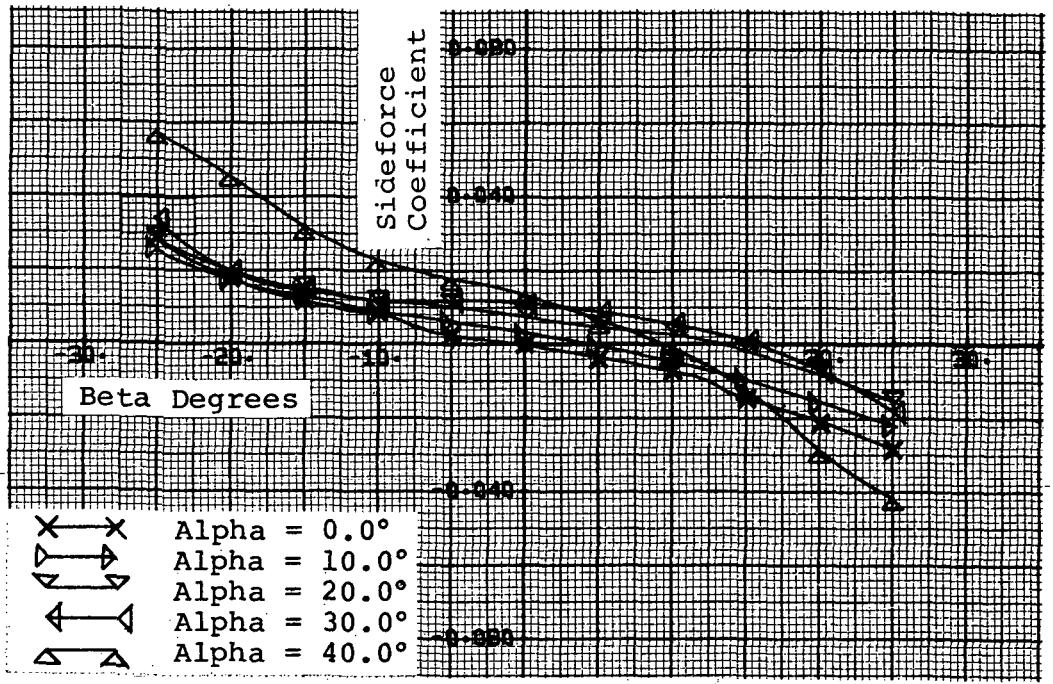

(a) Flat Plate Model

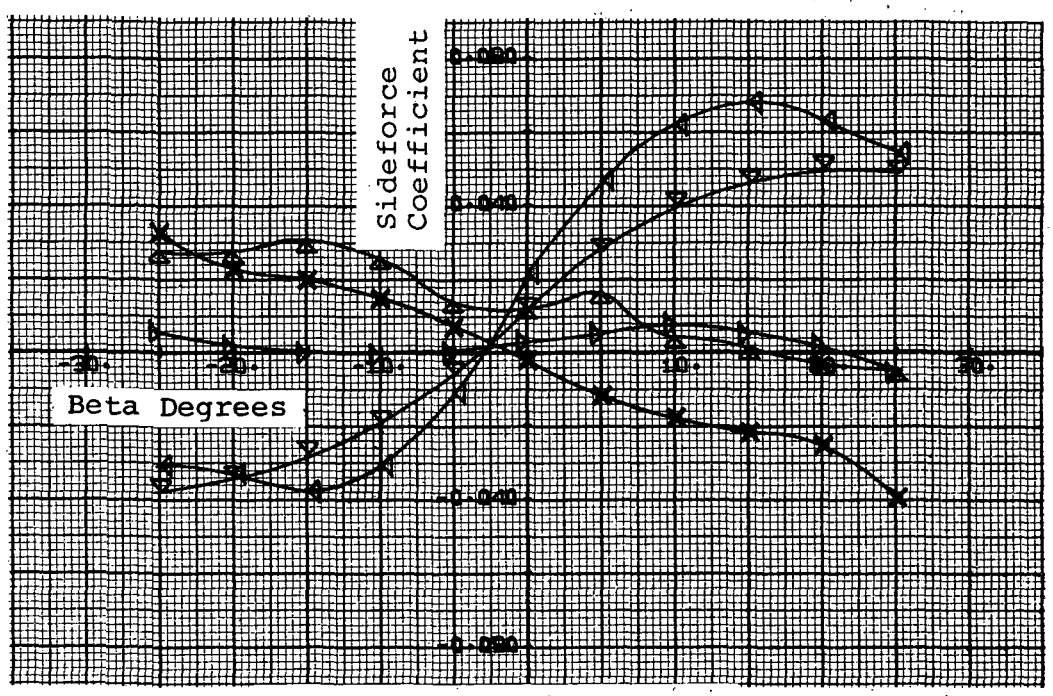

(b) Apex Camber Model

Figure 22 - Side Force Characteristics

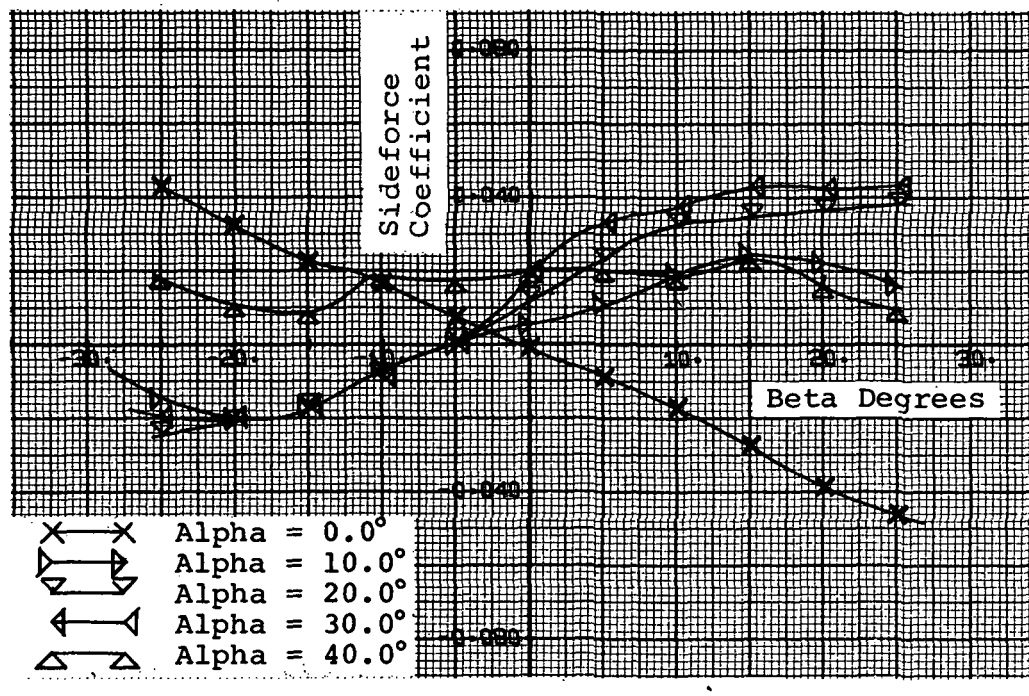

(c) Conical Camber Model

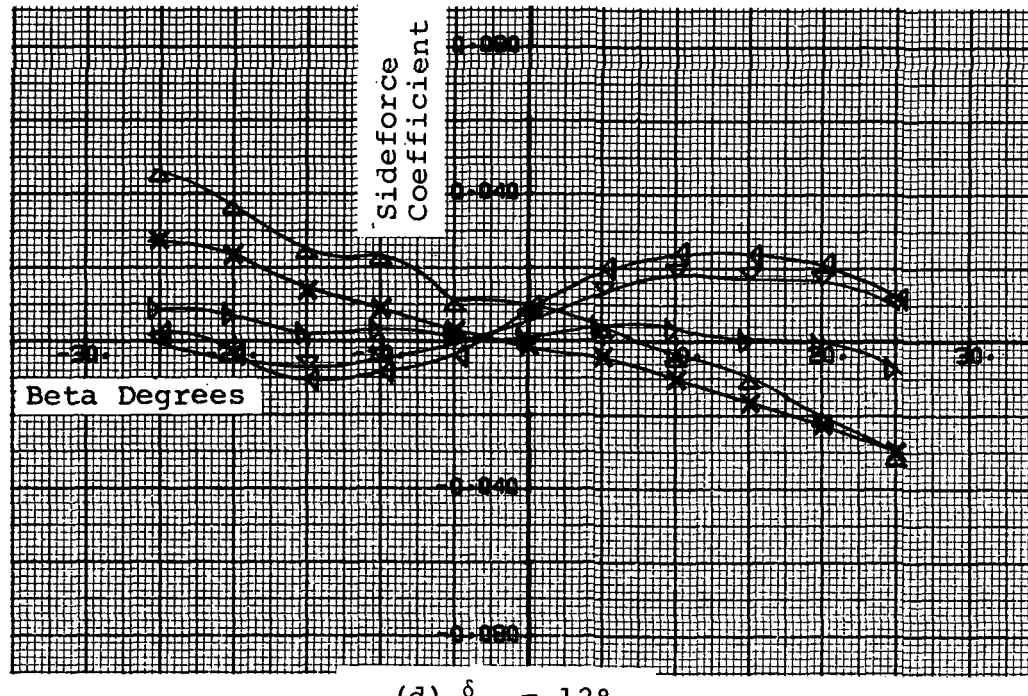

(d) $\delta_n = 12°$

Figure 22 - Side Force Characteristics (Continued)

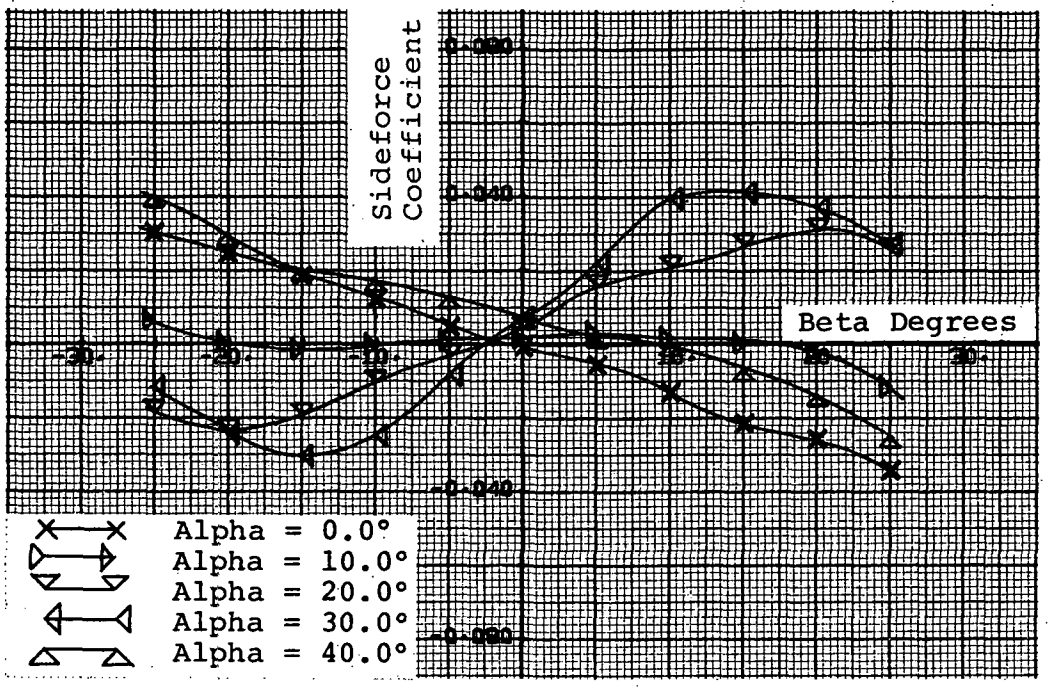

(e) δ_n = 24°

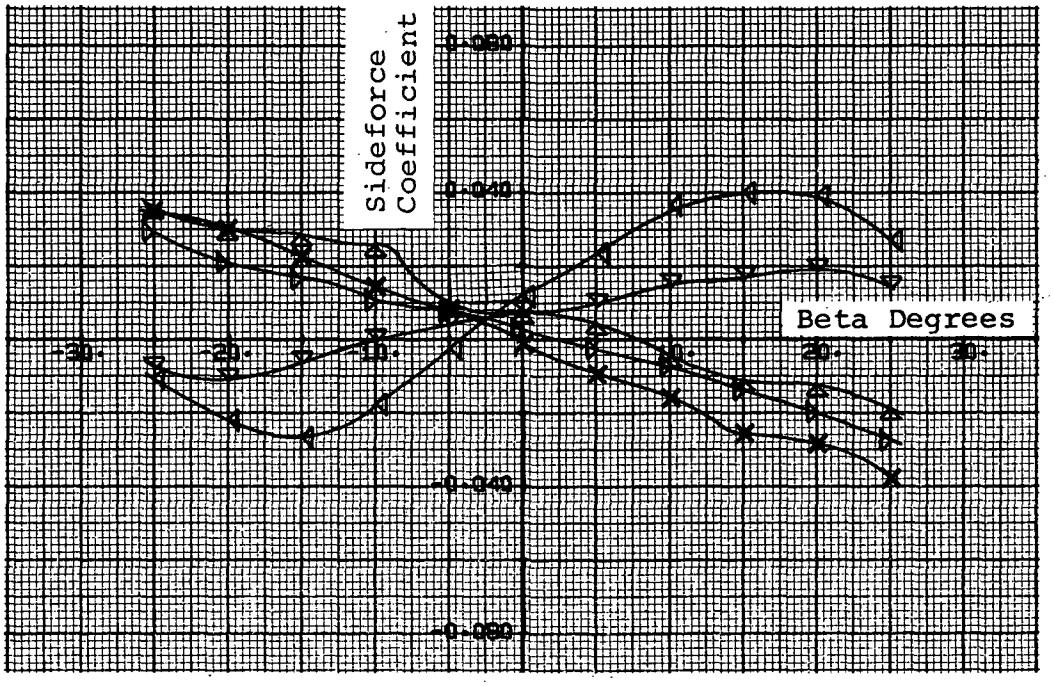

(f) δ_n = 36°

Figure 22 - Side Force Characteristics (Continued)

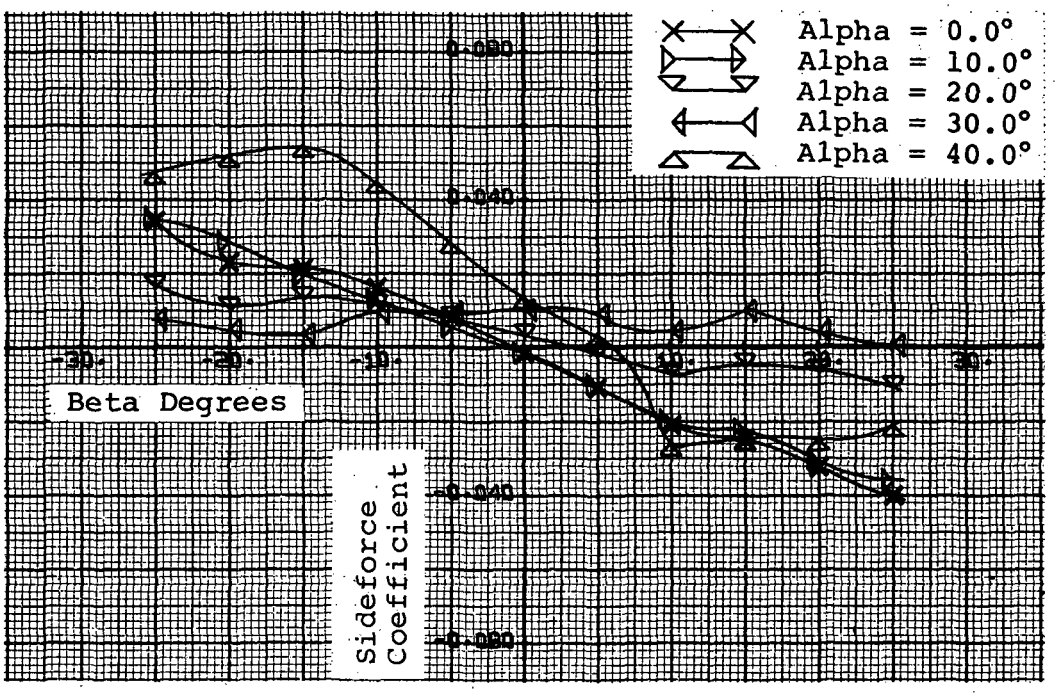

(g) $\delta_n = 60°$

Figure 22 - Side Force Characteristics (Concluded)

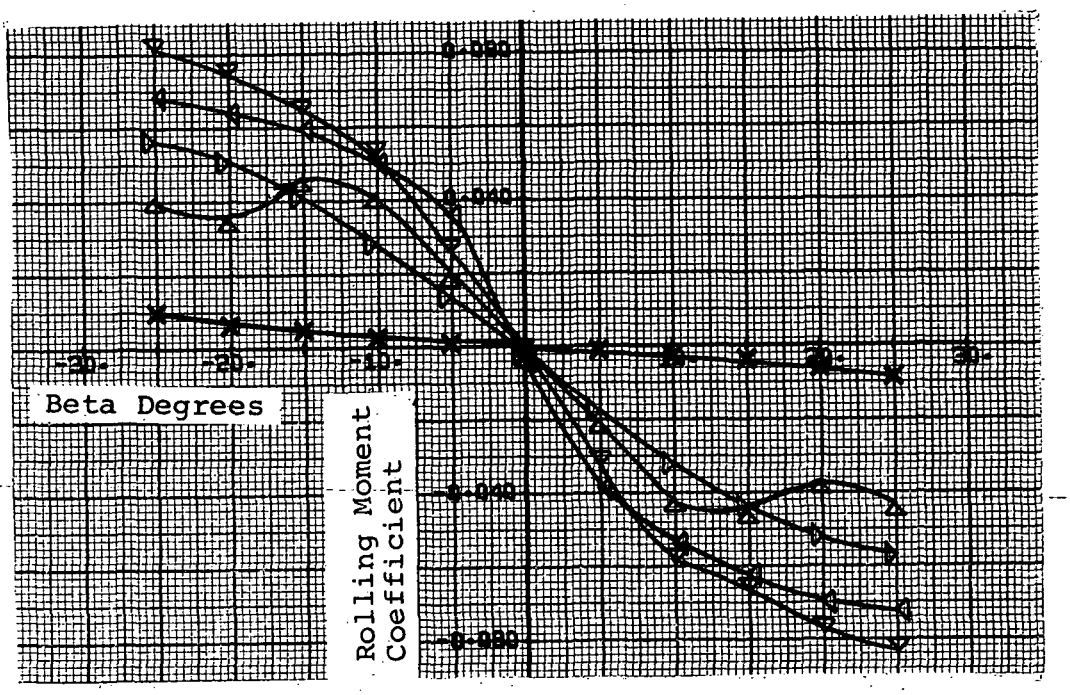

(a) Flat Plate Model

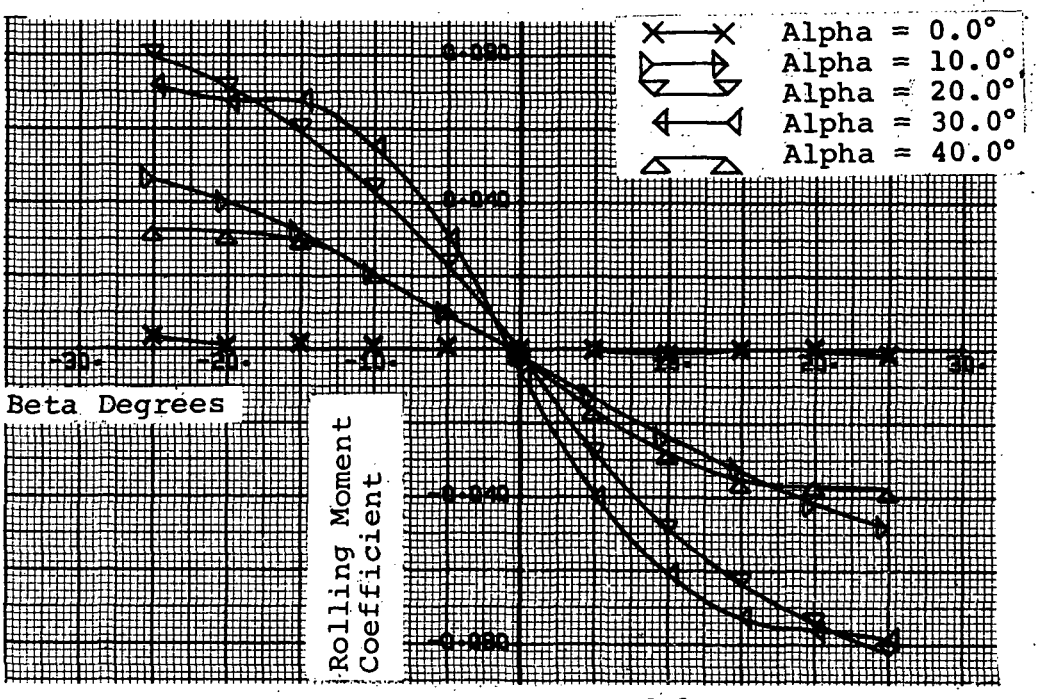

(b) Apex Camber Model

Figure 23 - Rolling Moment Characteristics

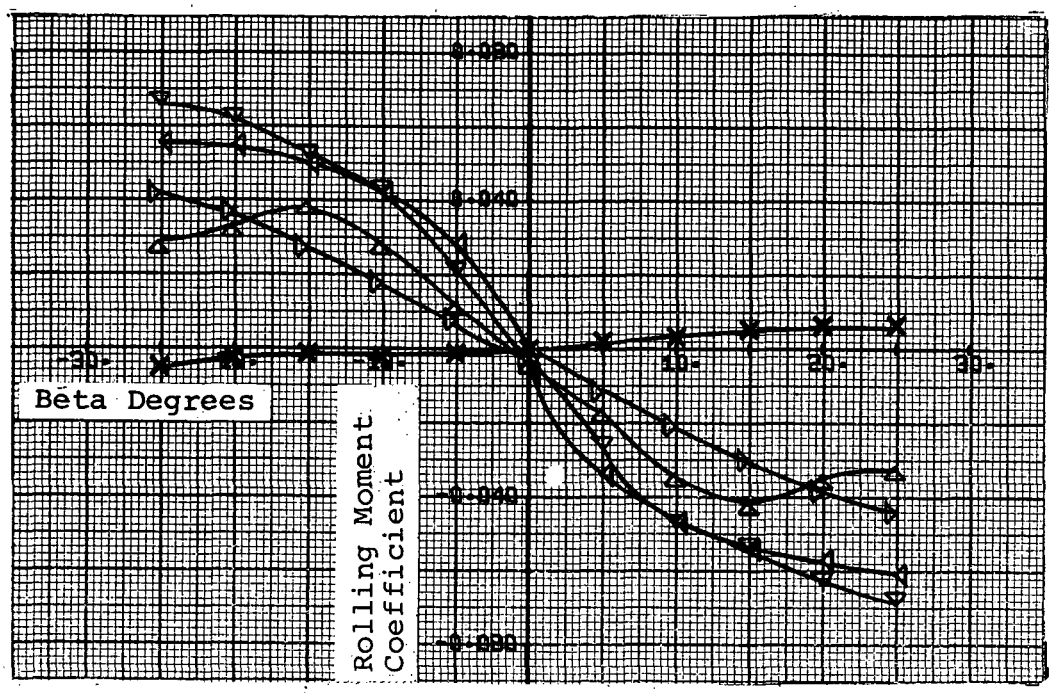

(c) Conical Camber Model

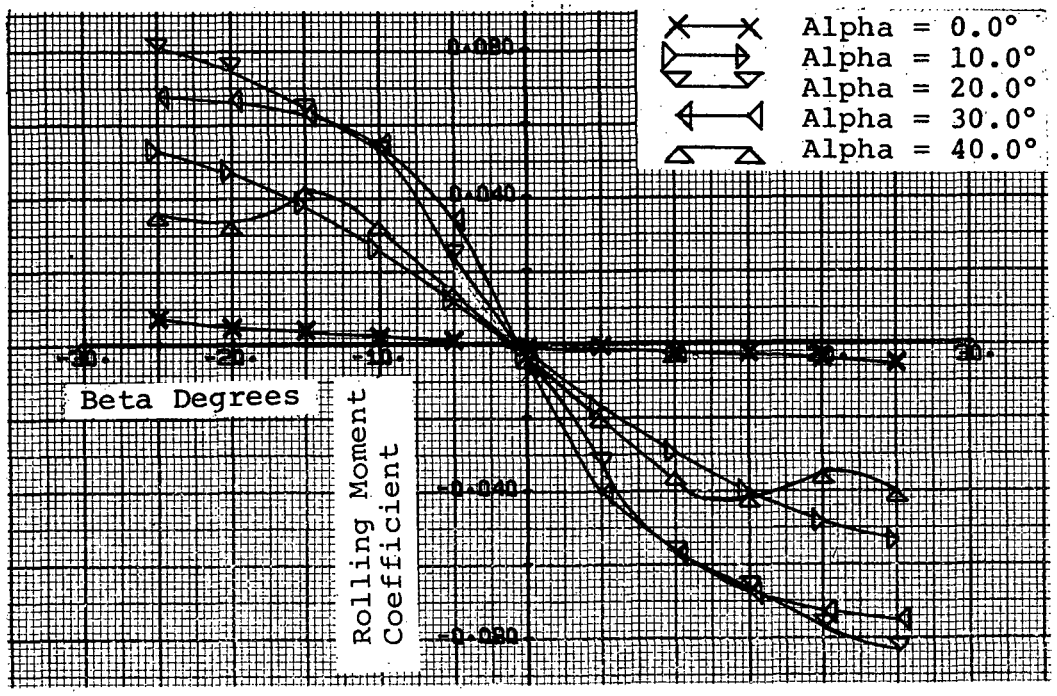

(d) δ_n= 12°

Figure 23 - Rolling Moment Characteristics (Continued)

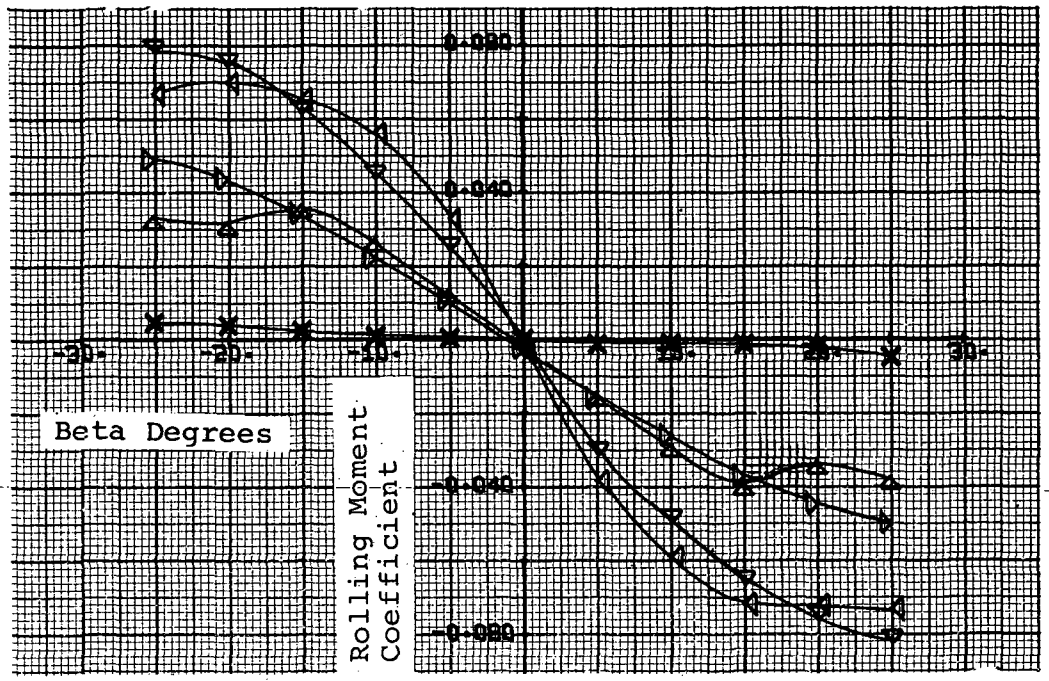

(e) δ_n = 24°

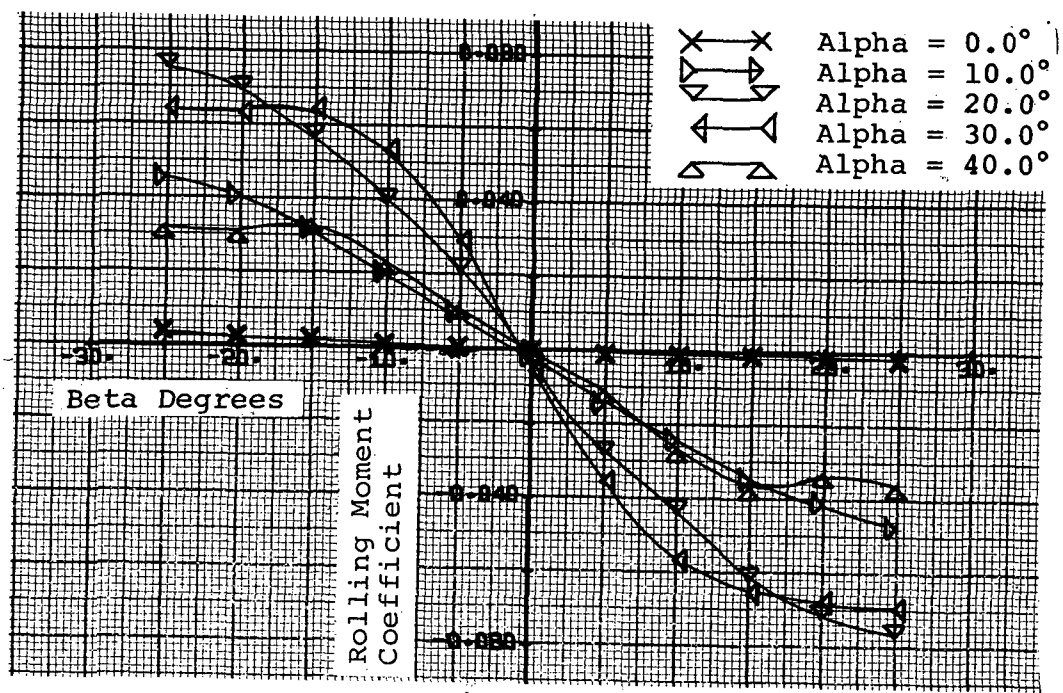

(f) δ_n = 36°

Figure 23 - Rolling Moment Characteristics (Continued)

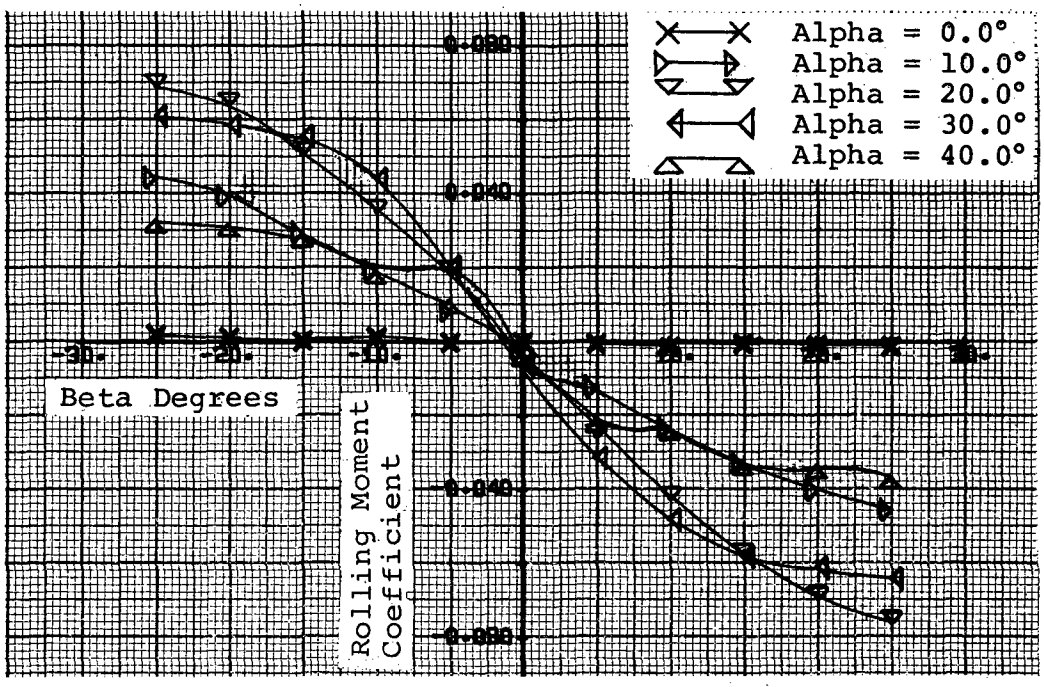

(g) δ_n = 60°

Figure 23 - Rolling Moment Characteristics (Concluded)

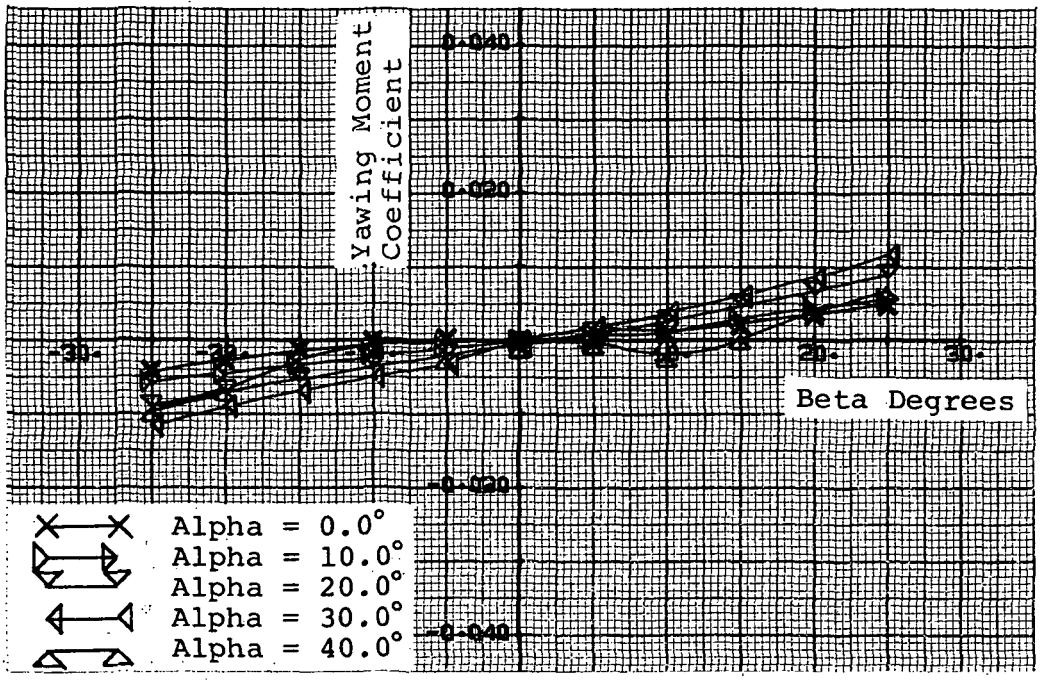

(a) Flat Plate Model

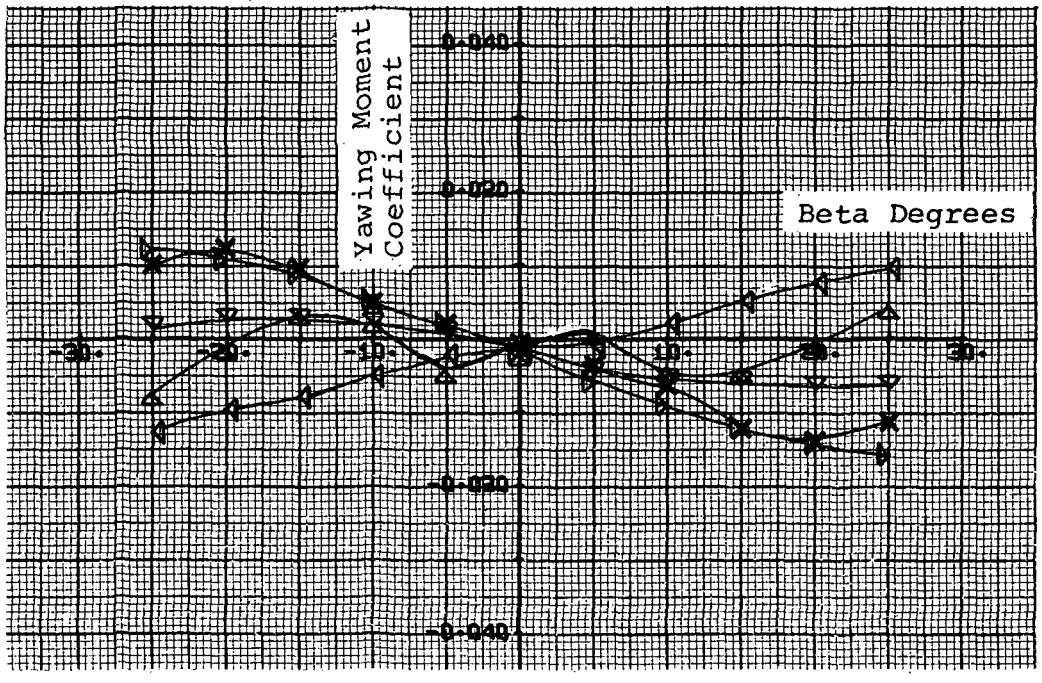

(b) Apex Camber Model

Figure 24 - Yawing Moment Characteristics

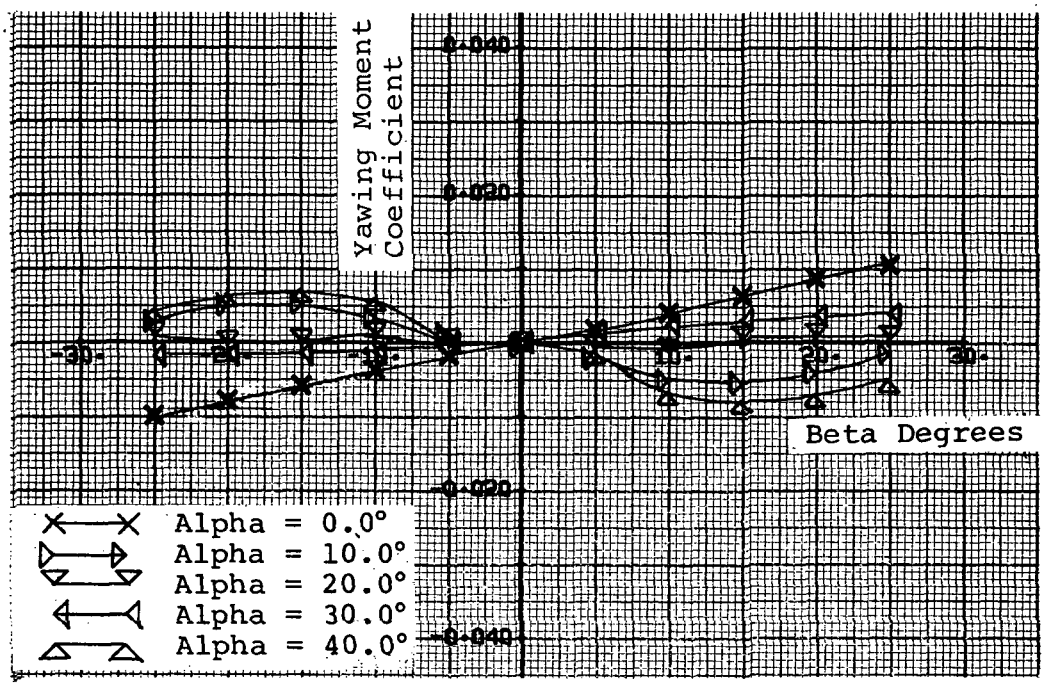

(c) Conical Camber Model

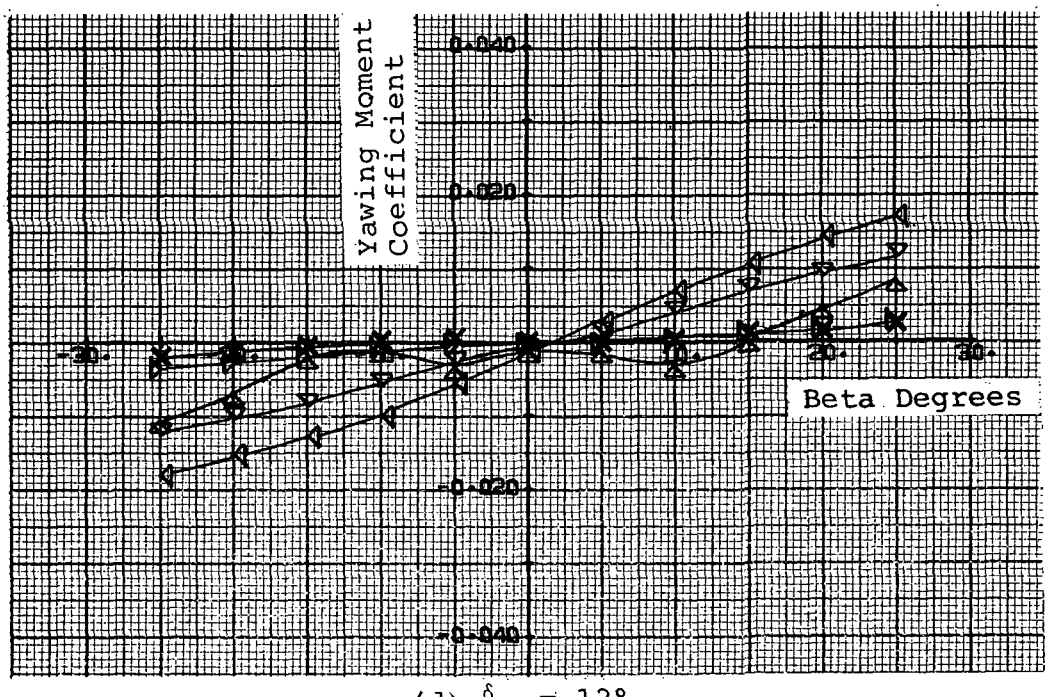

(d) δ_n = 12°

Figure 24 - Yawing Moment Characteristics (Continued)

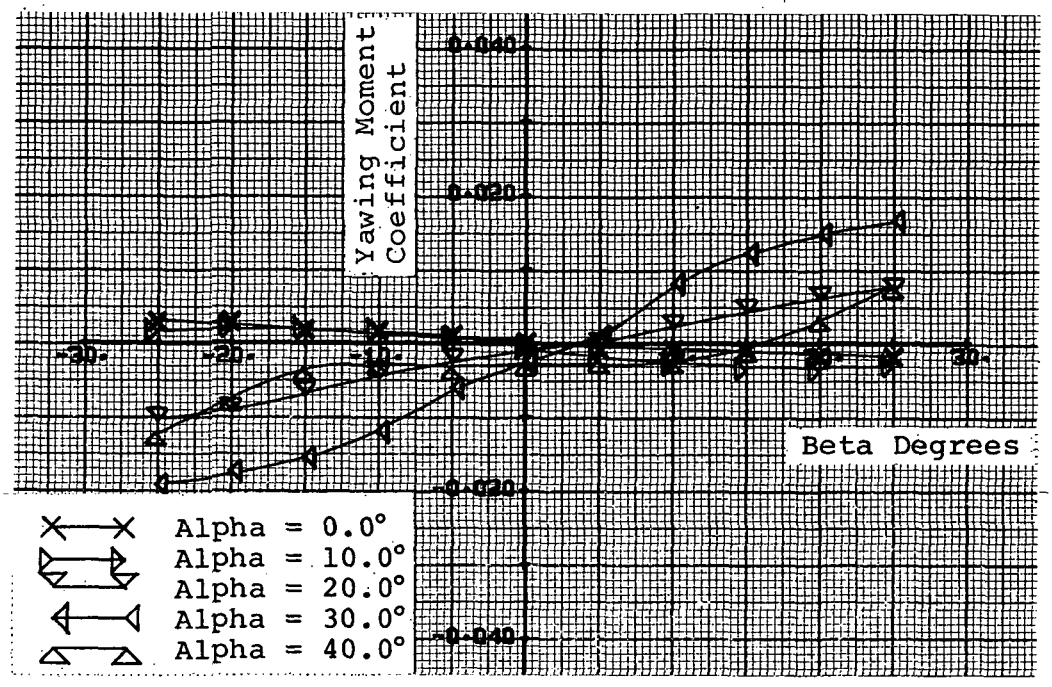

(e) $\delta_n = 24°$

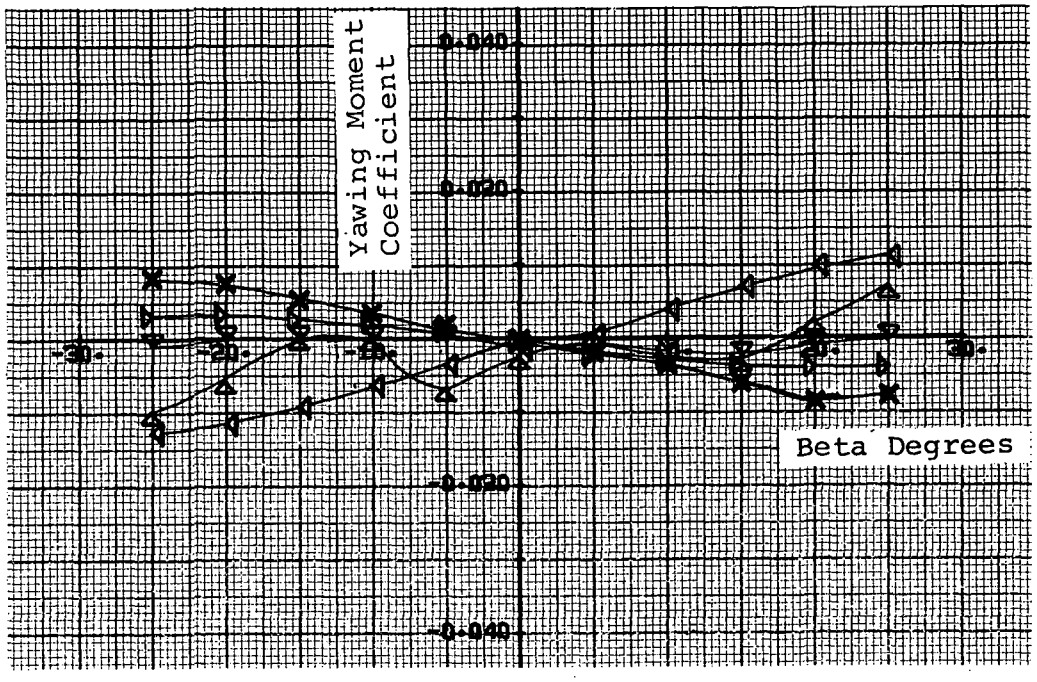

(f) $\delta_n = 36°$

Figure 24 - Yawing Moment Characteristics (Continued)

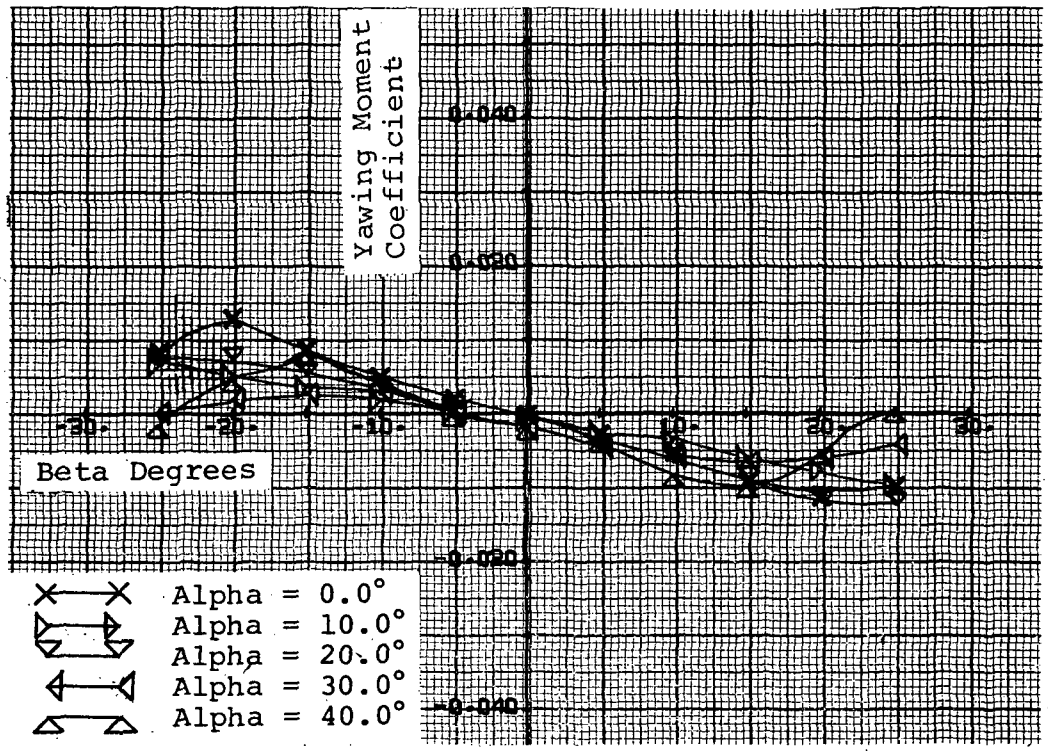

(g) $\delta_n = 60°$

Figure 24 - Yawing Moment Characteristics (Concluded)

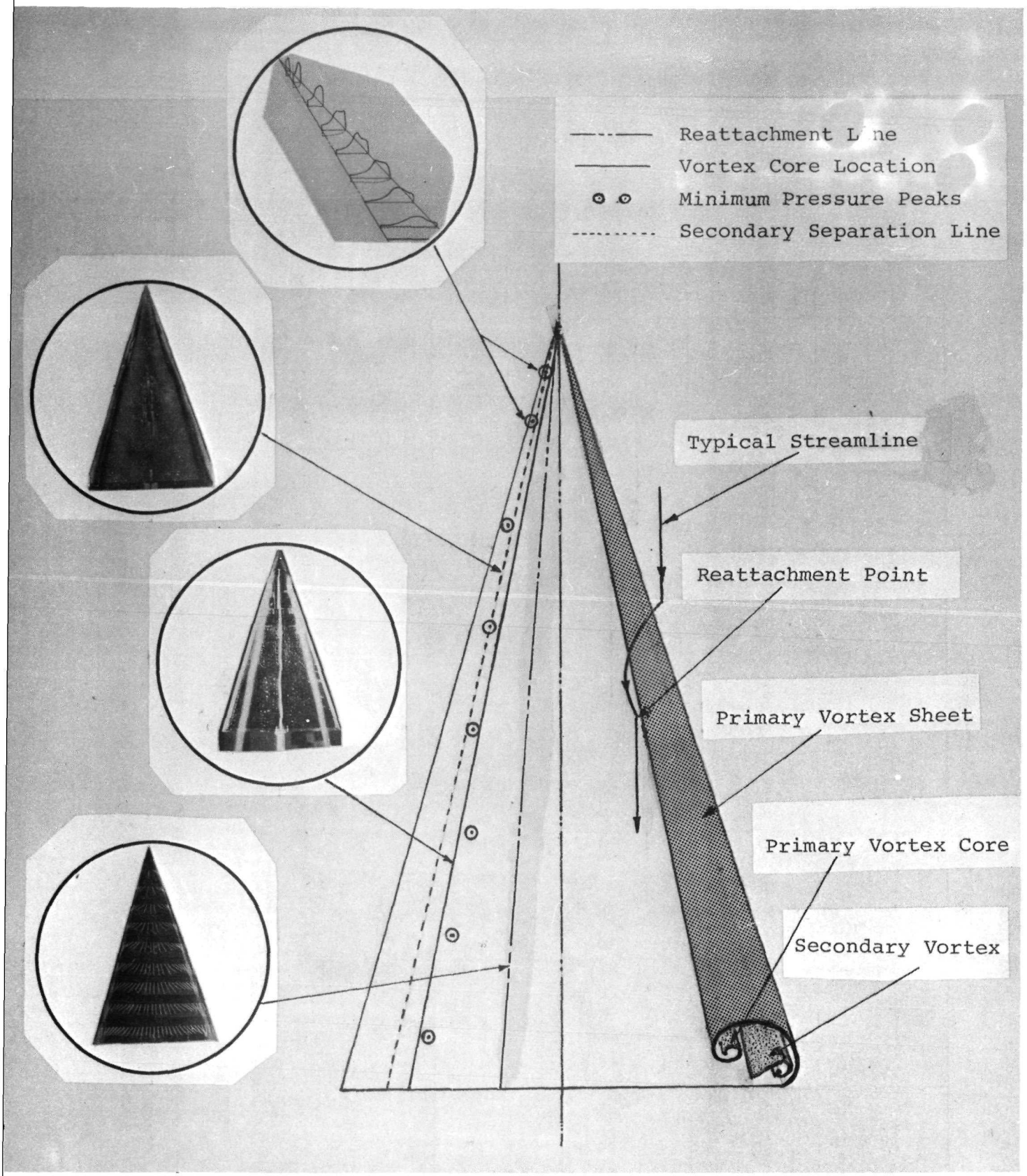

Figure 25 - Composite Analysis of Flow Field.

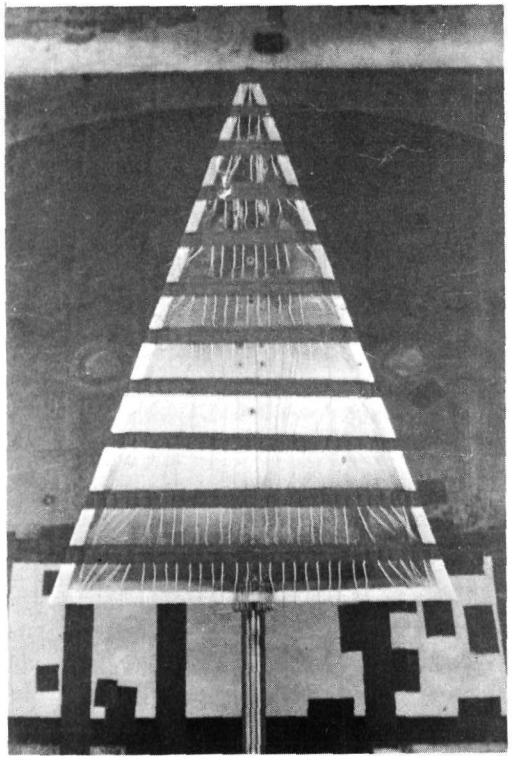

Flat Plate

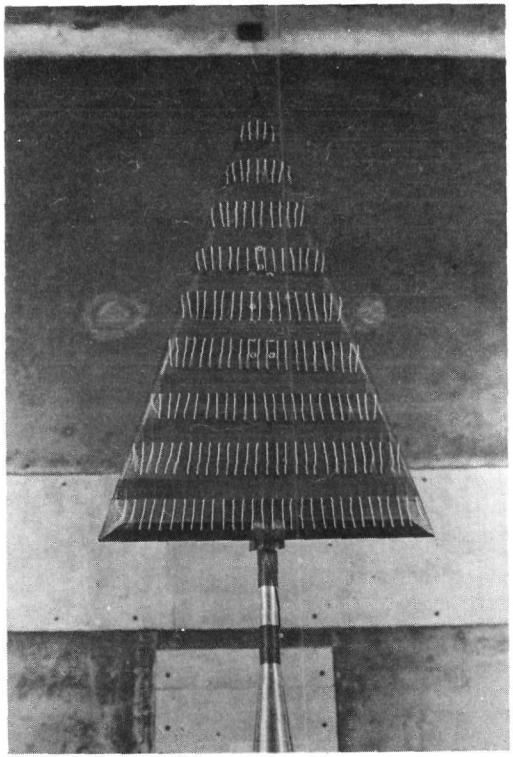

Apex Camber

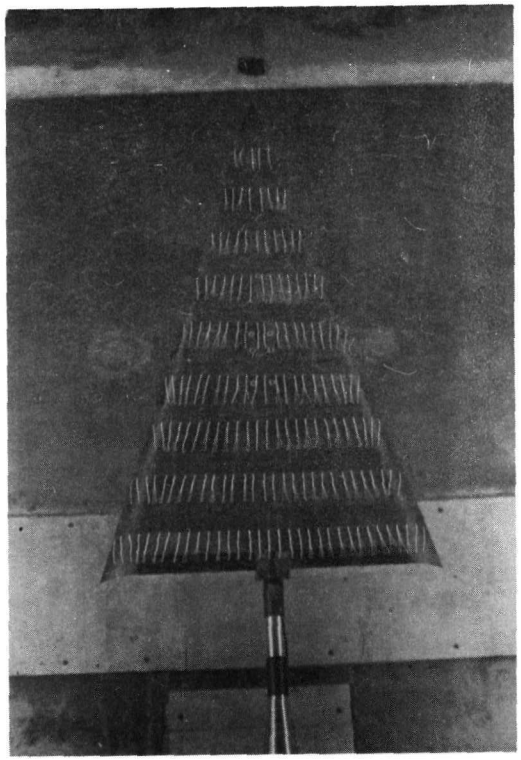

Conical Camber

Figure 26 - Tuft Patterns, $\alpha = 5°$

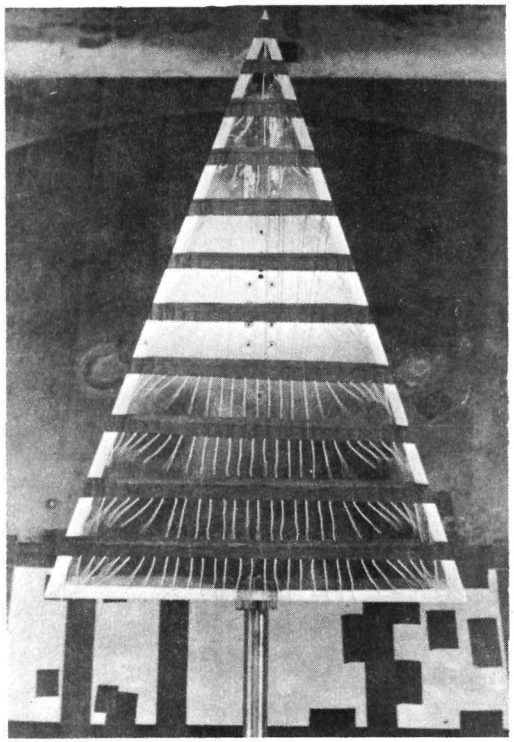

Flat Plate

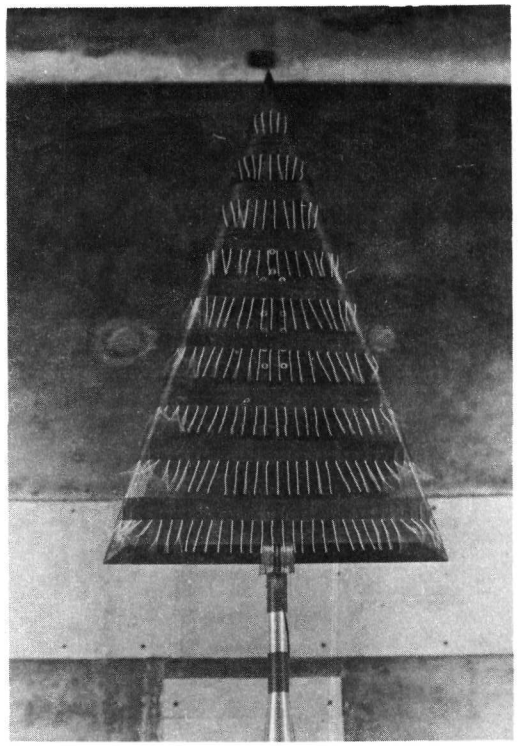

Apex Camber

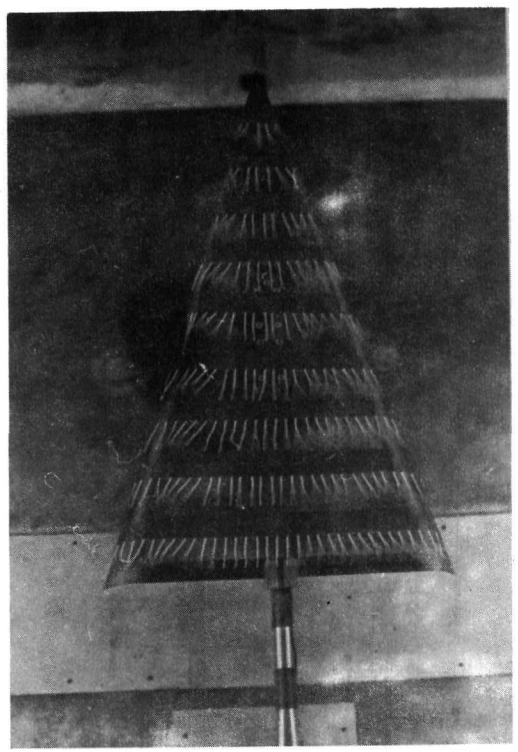

Conical Camber

Figure 27 - Tuft Patterns, $\alpha = 10°$

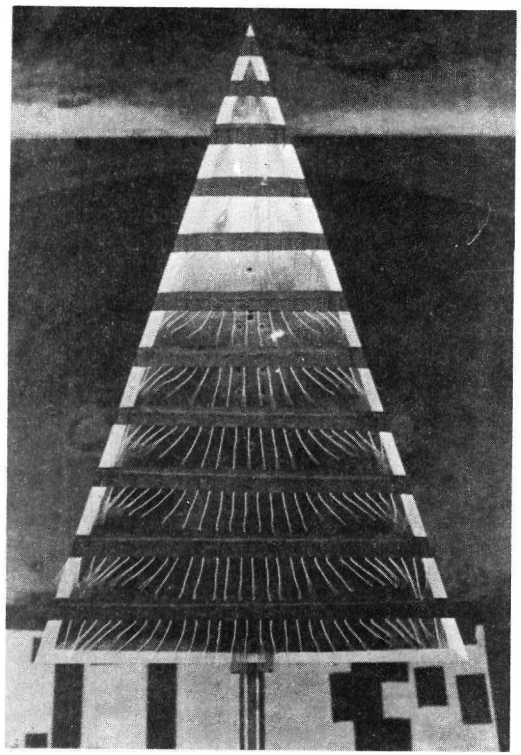

Flat Plate

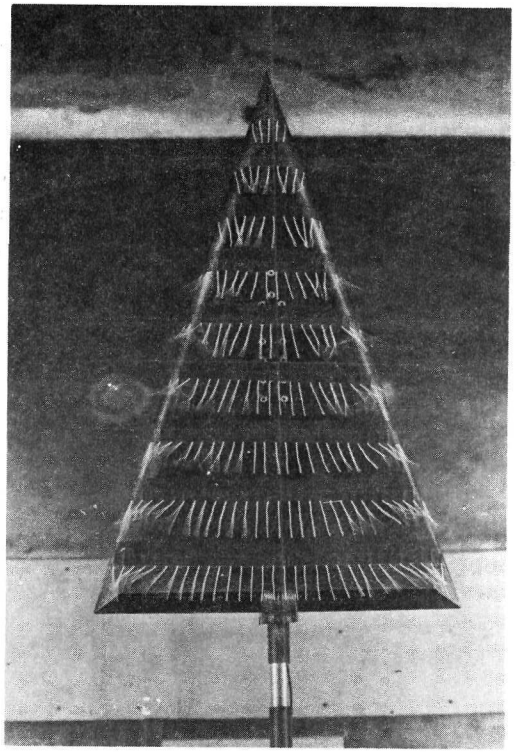

Apex Camber

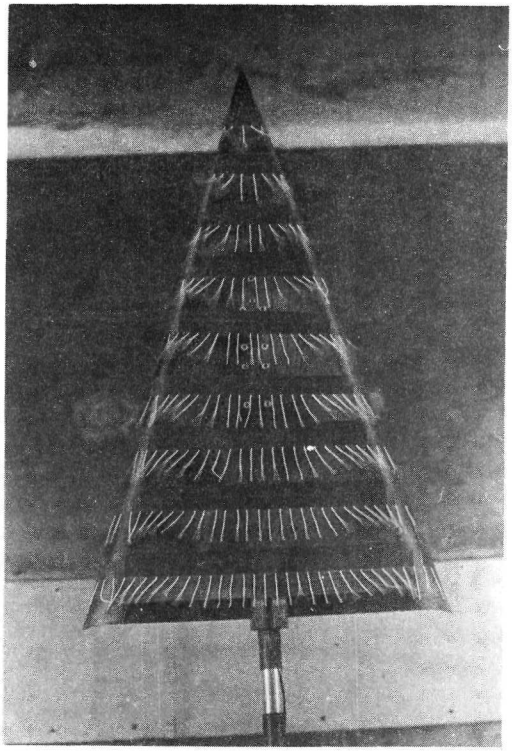

Conical Camber

Figure 28 - Tuft Patterns, $\alpha = 15°$

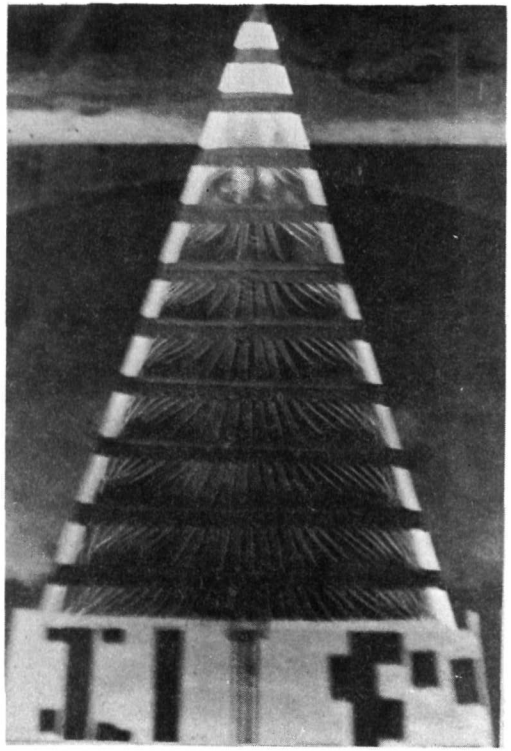

Flat Plate

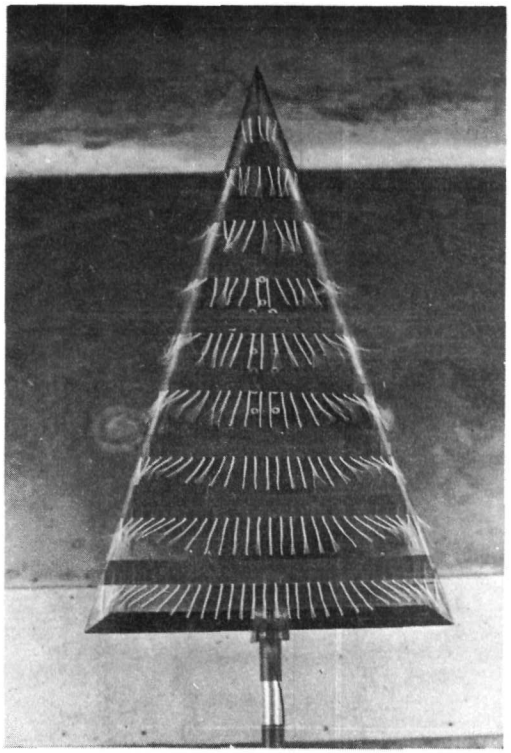

Apex Camber

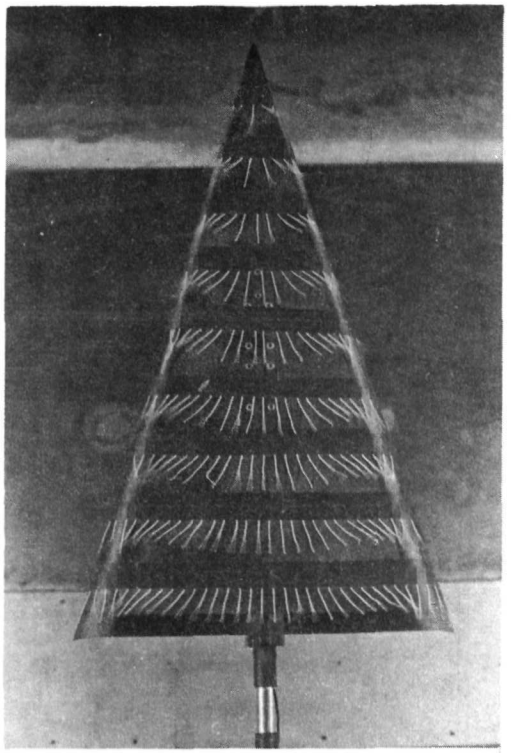

Conical Camber

Figure 29 - Tuft Patterns, $\alpha = 20°$

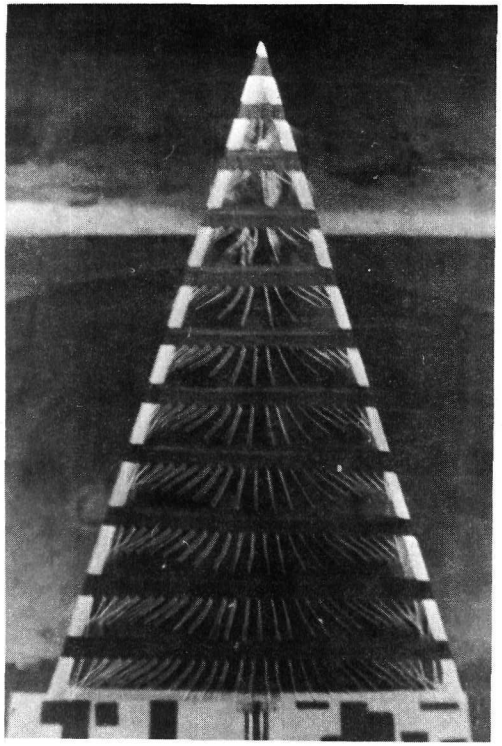

Flat Plate

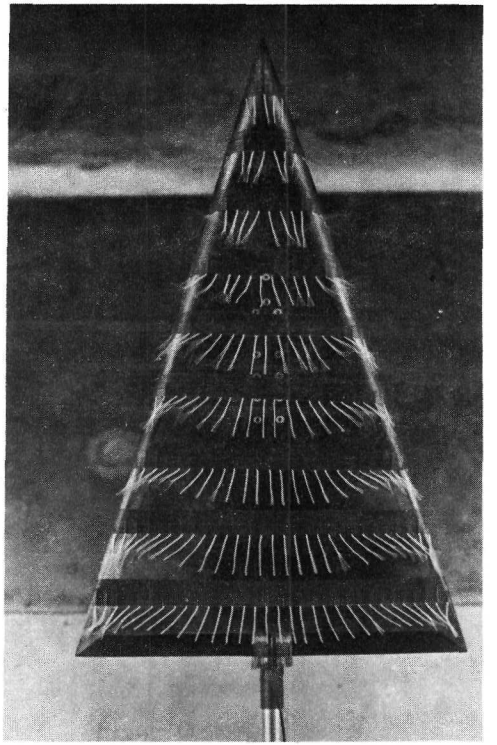

Apex Camber

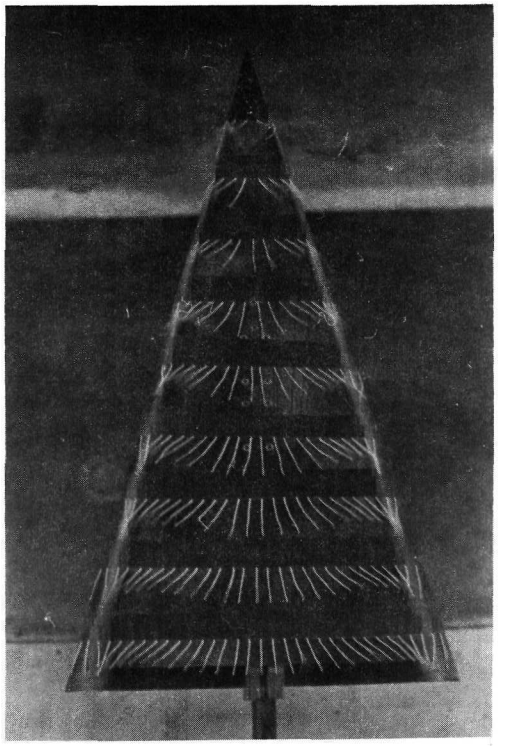

Conical Camber

Figure 30 - Tuft Patterns, $\alpha = 25°$

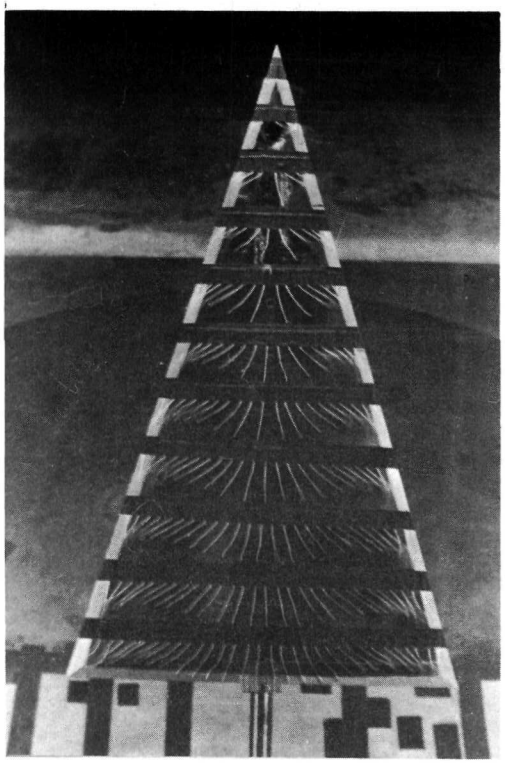

Flat Plate

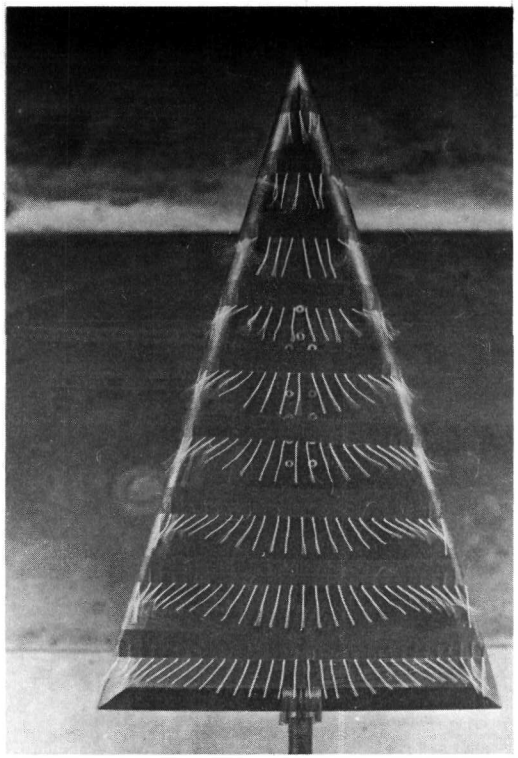

Apex Camber

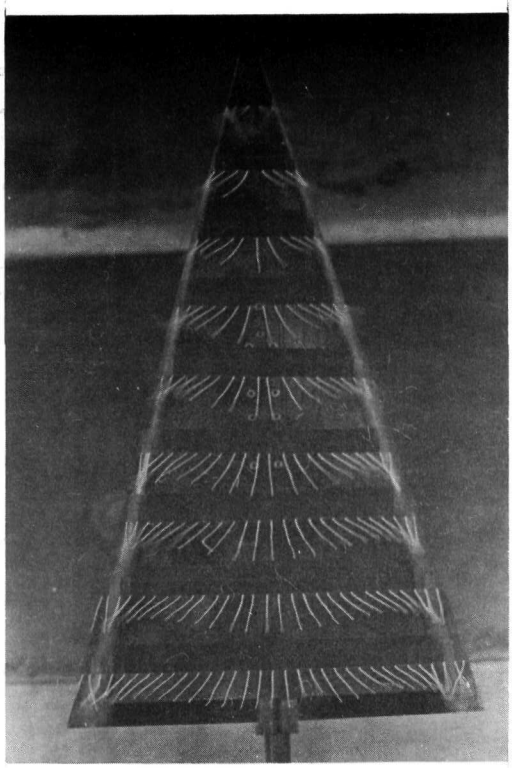

Conical Camber

Figure 31 - Tuft Patterns, $\alpha = 30°$

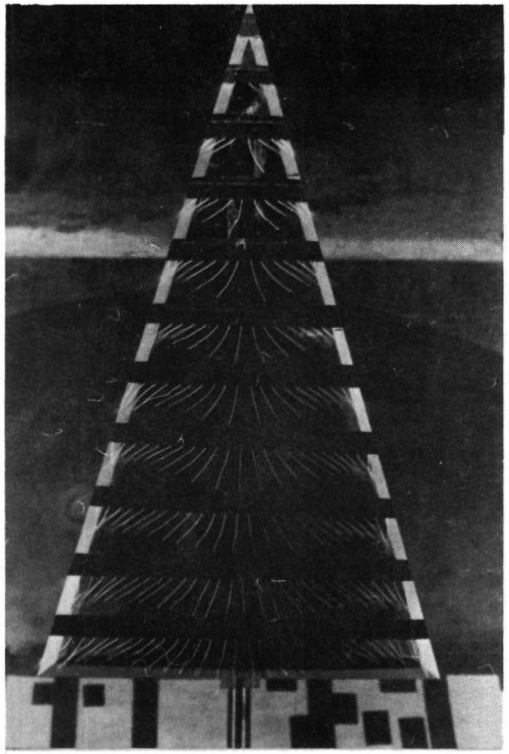

Flat Plate

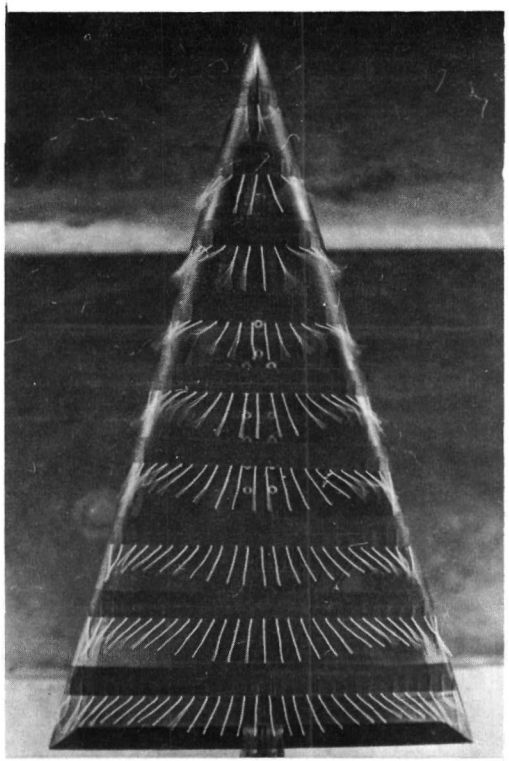

Apex Camber

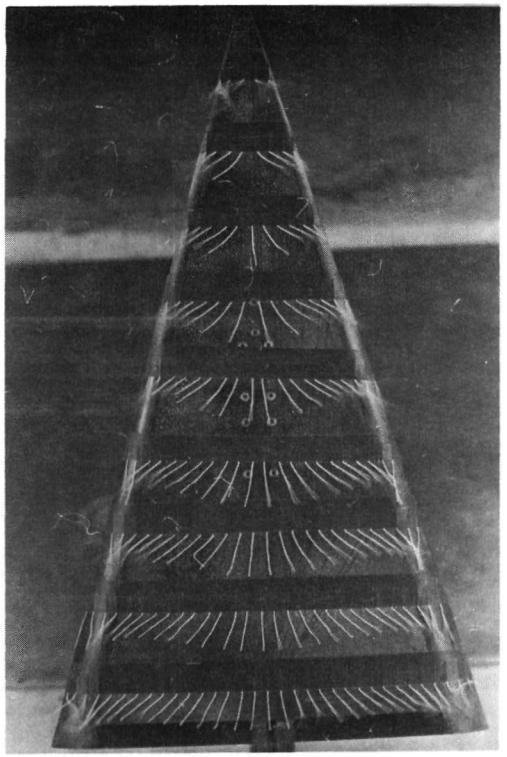

Conical Camber

Figure 32 - Tuft Patterns, $\alpha = 35°$

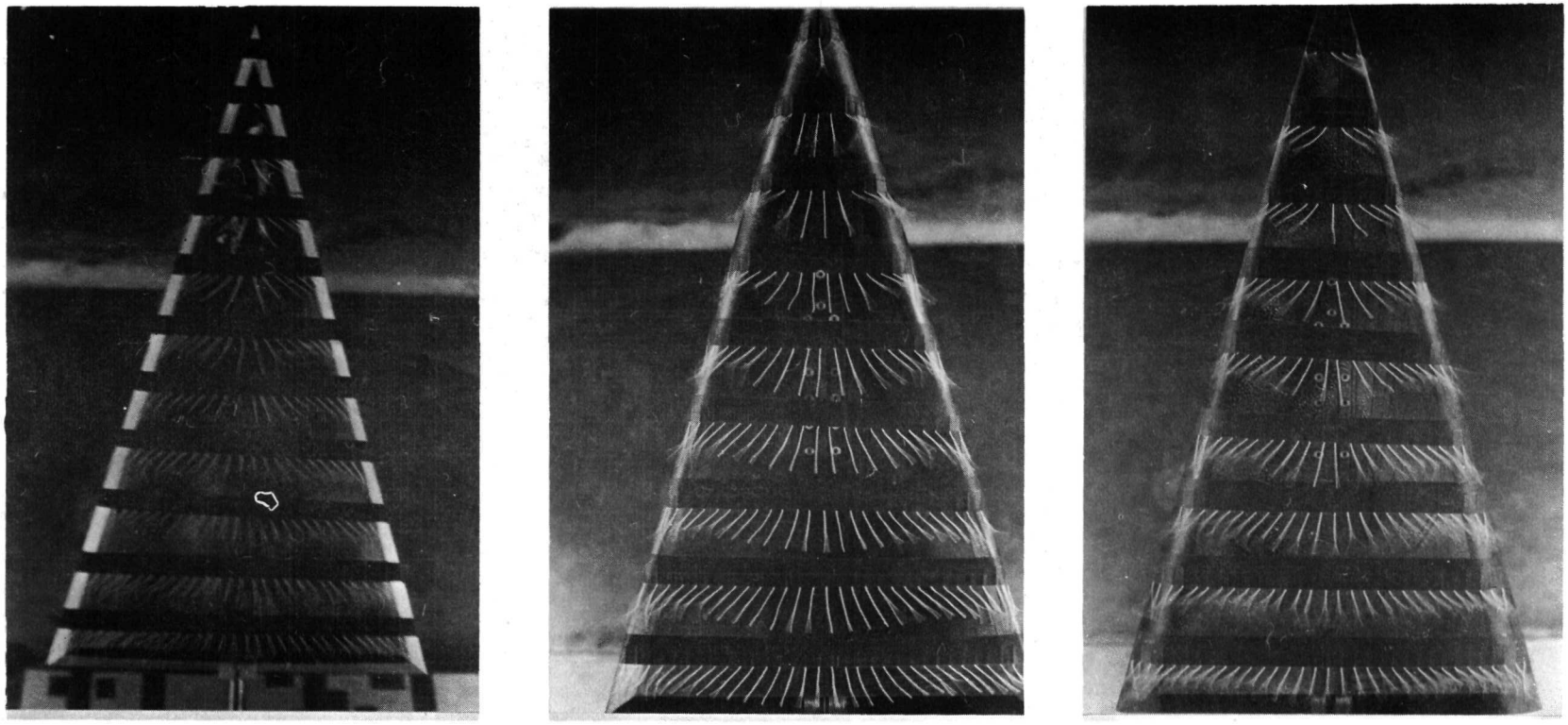

Flat Plate | Apex Camber | Conical Camber

Figure 33 - Tuft Patterns, $\alpha = 40°$

Figure 34 - Oil Flow Patterns, $\alpha = 10°$

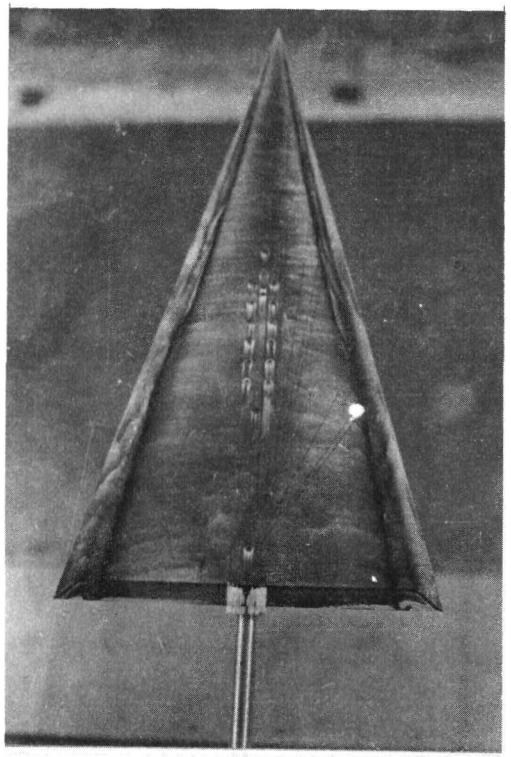

Flat Plate

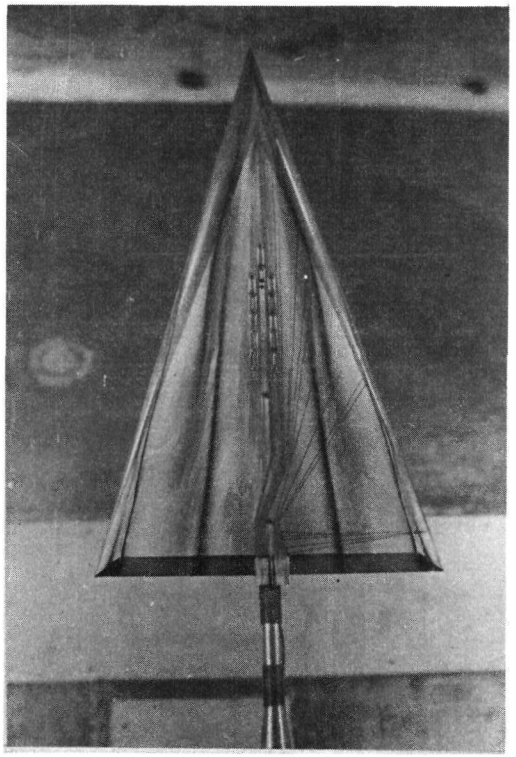

Apex Camber

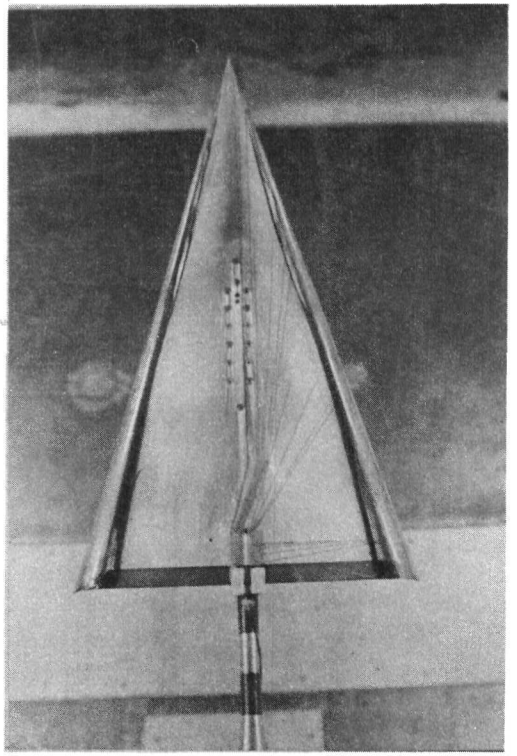

Conical Camber

Figure 35 - Oil Flow Patterns, $\alpha = 15°$

Figure 36 - Oil Flow Patterns, $\alpha = 20°$

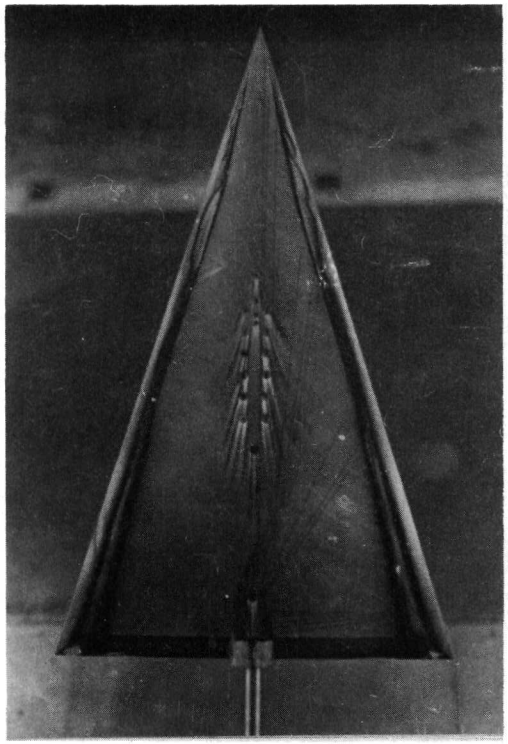

Flat Plate

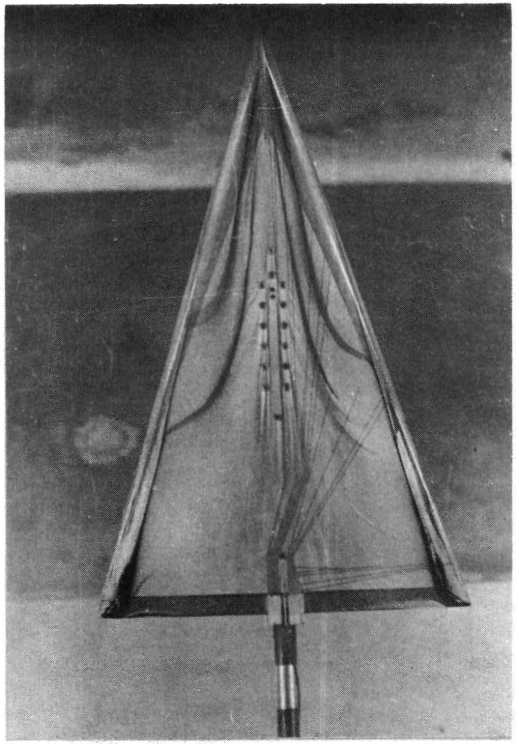

Apex Camber

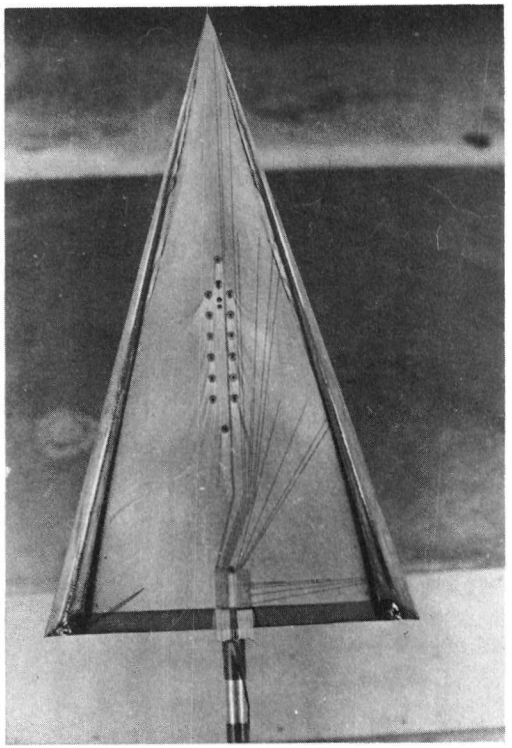

Conical Camber

Figure 37 - Oil Flow Patterns, $\alpha = 25°$

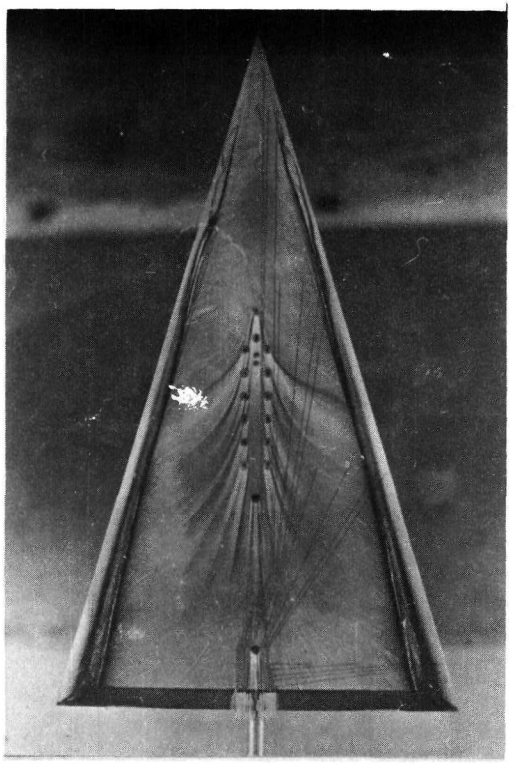

Flat Plate

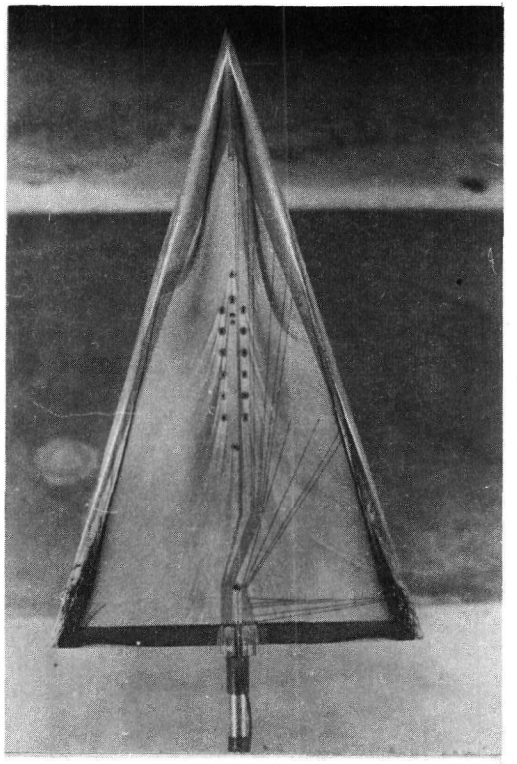

Apex Camber

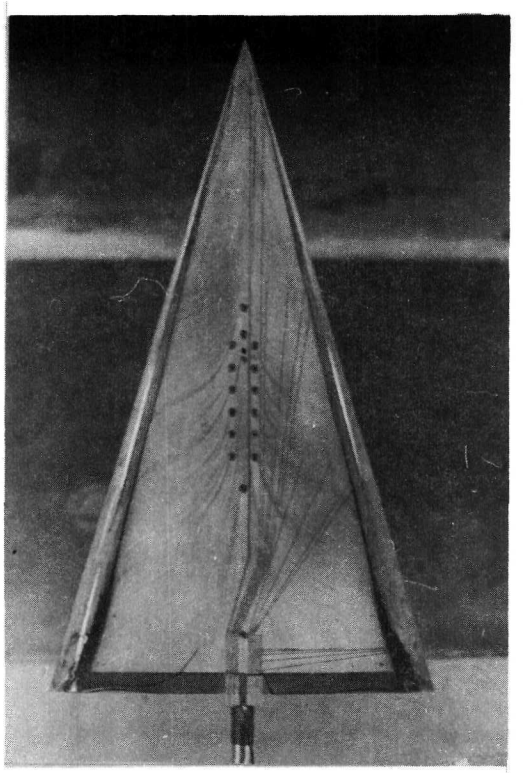

Conical Camber

Figure 38 - Oil Flow Patterns, $\alpha = 30°$

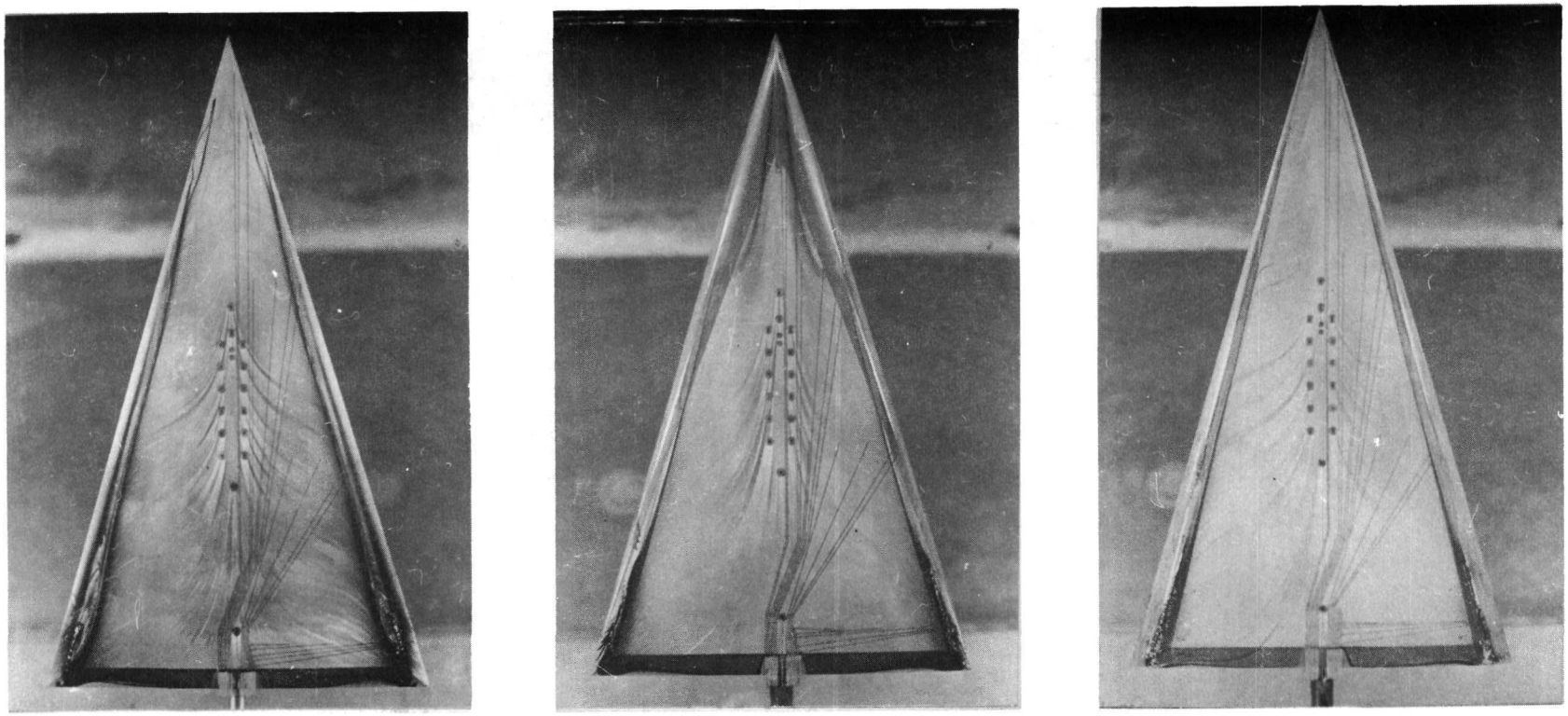

Flat Plate | Apex Camber | Conical Camber

Figure 39 - Oil Flow Patterns, $\alpha = 35°$

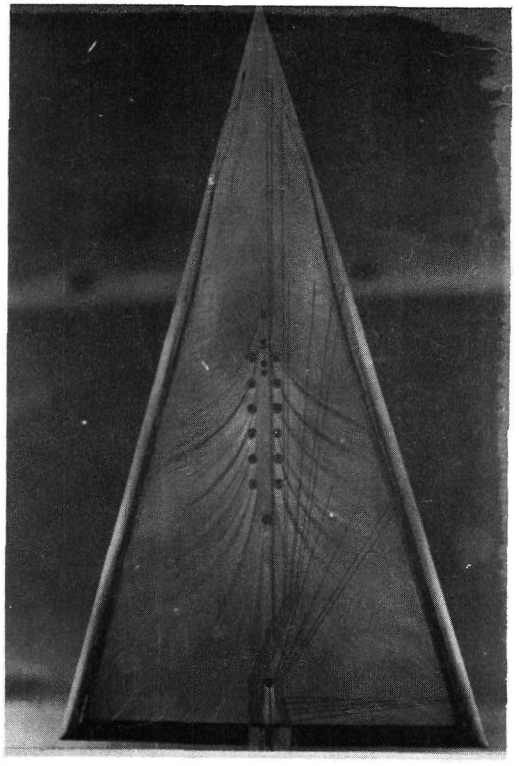

Flat Plate

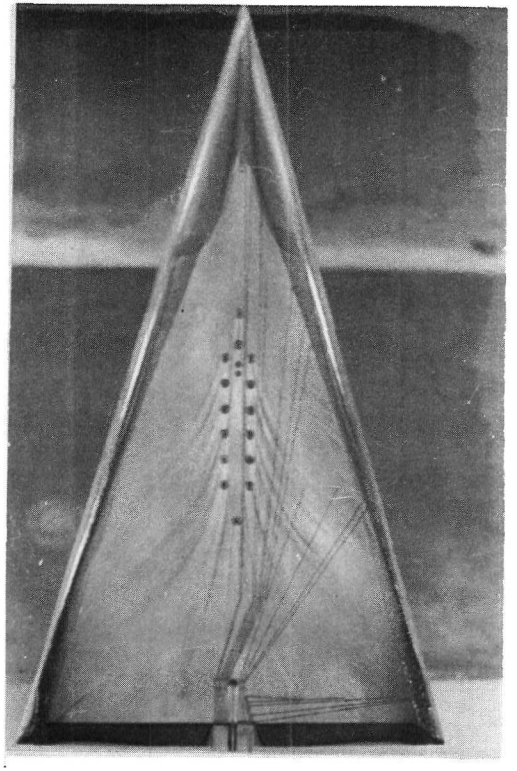

Apex Camber

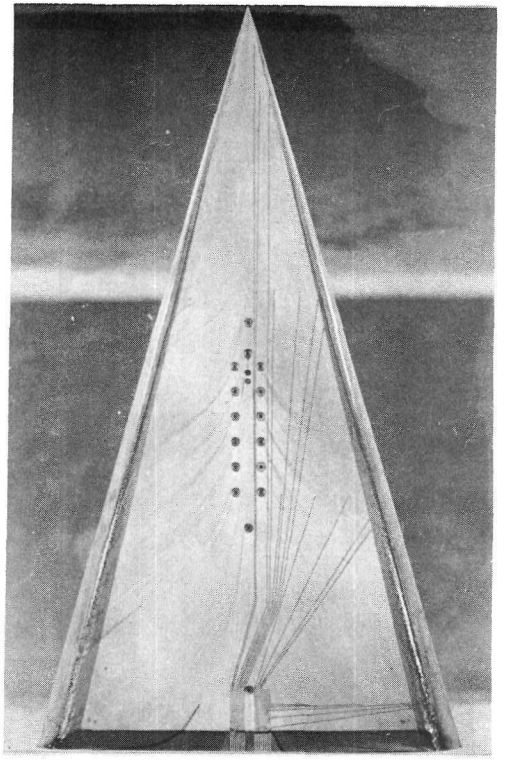

Conical Camber

Figure 40 - Oil Flow Patterns, $\alpha = 40°$

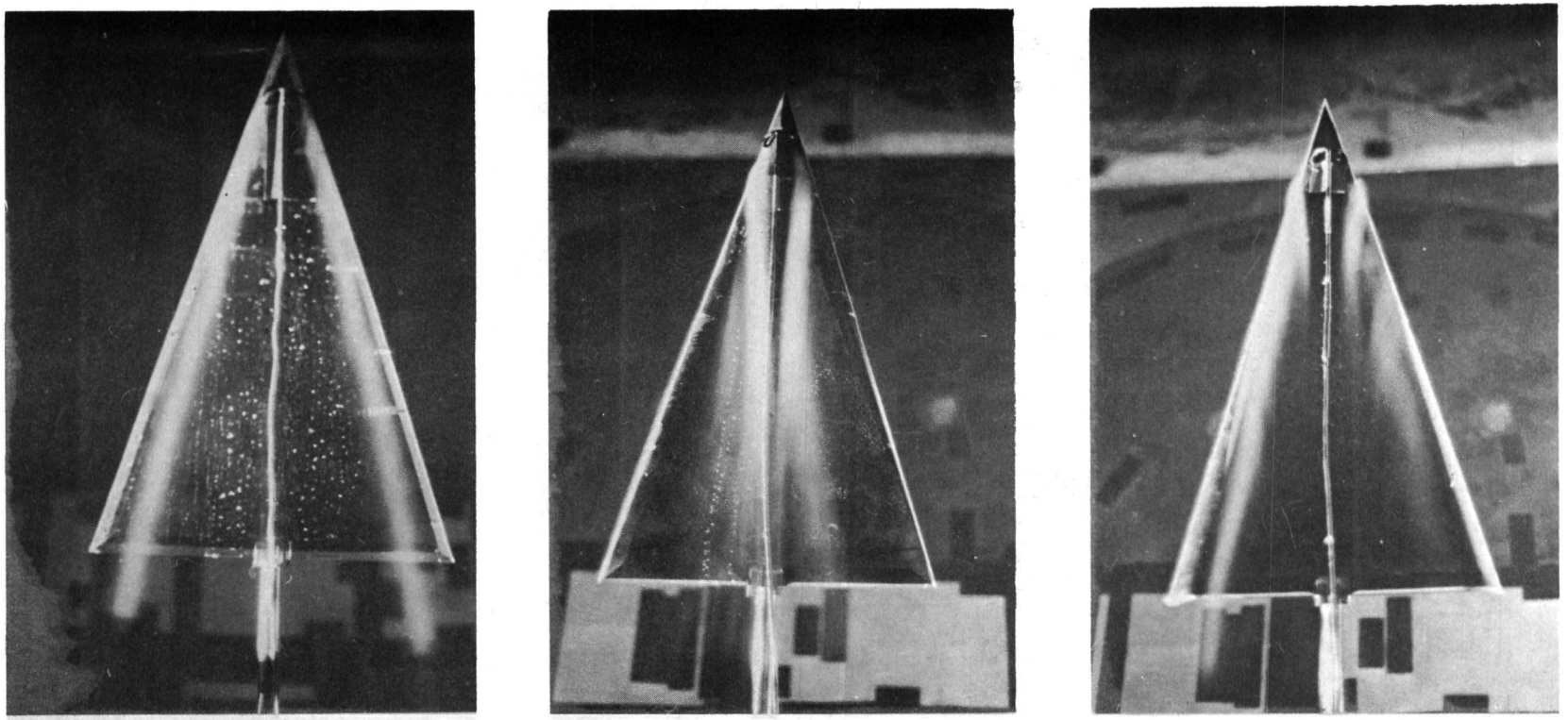

Flat Plate | Apex Camber | Conical Camber

Figure 41 - Water Vapor Patterns, $\alpha = 10°$

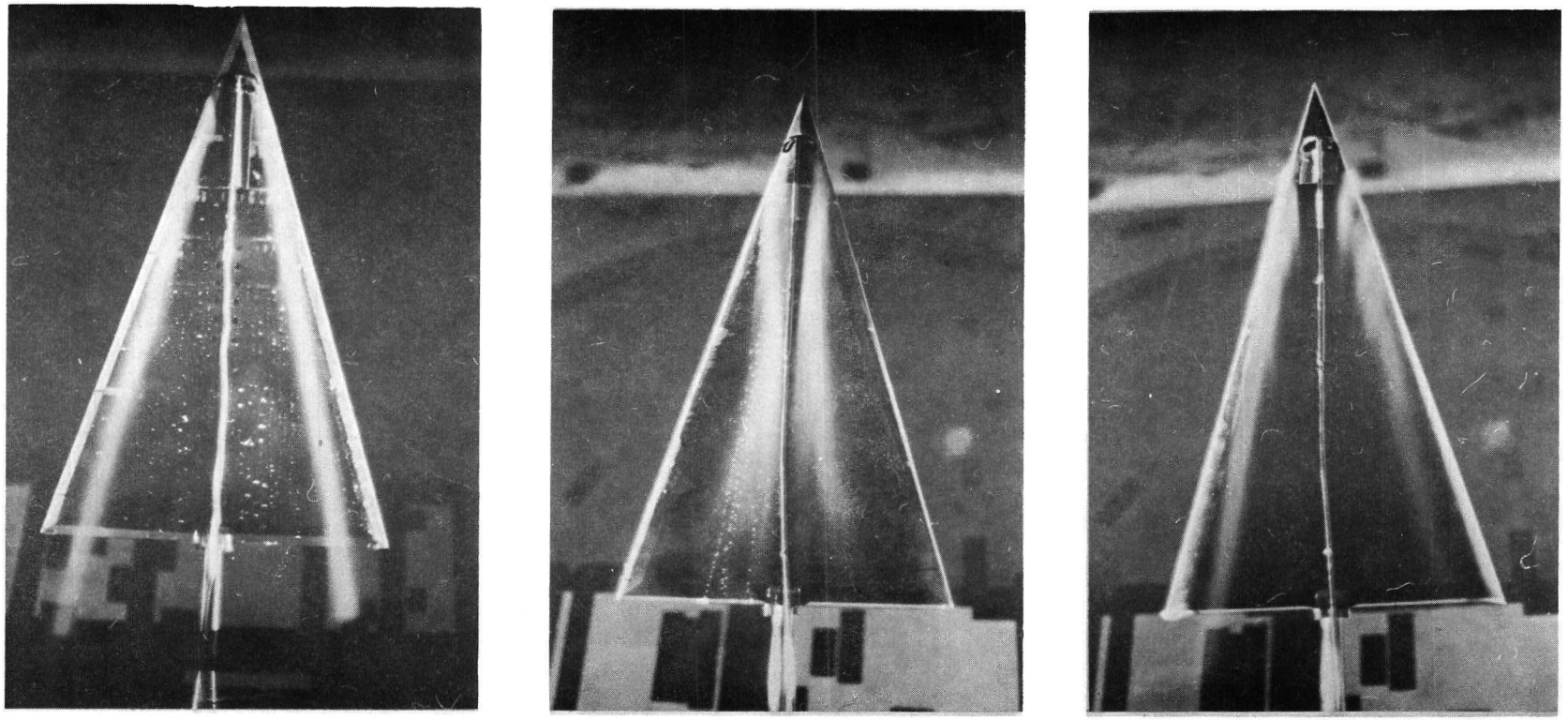

Flat Plate

Apex Camber

Conical Camber

Figure 42 - Water Vapor Patterns, $\alpha = 15°$

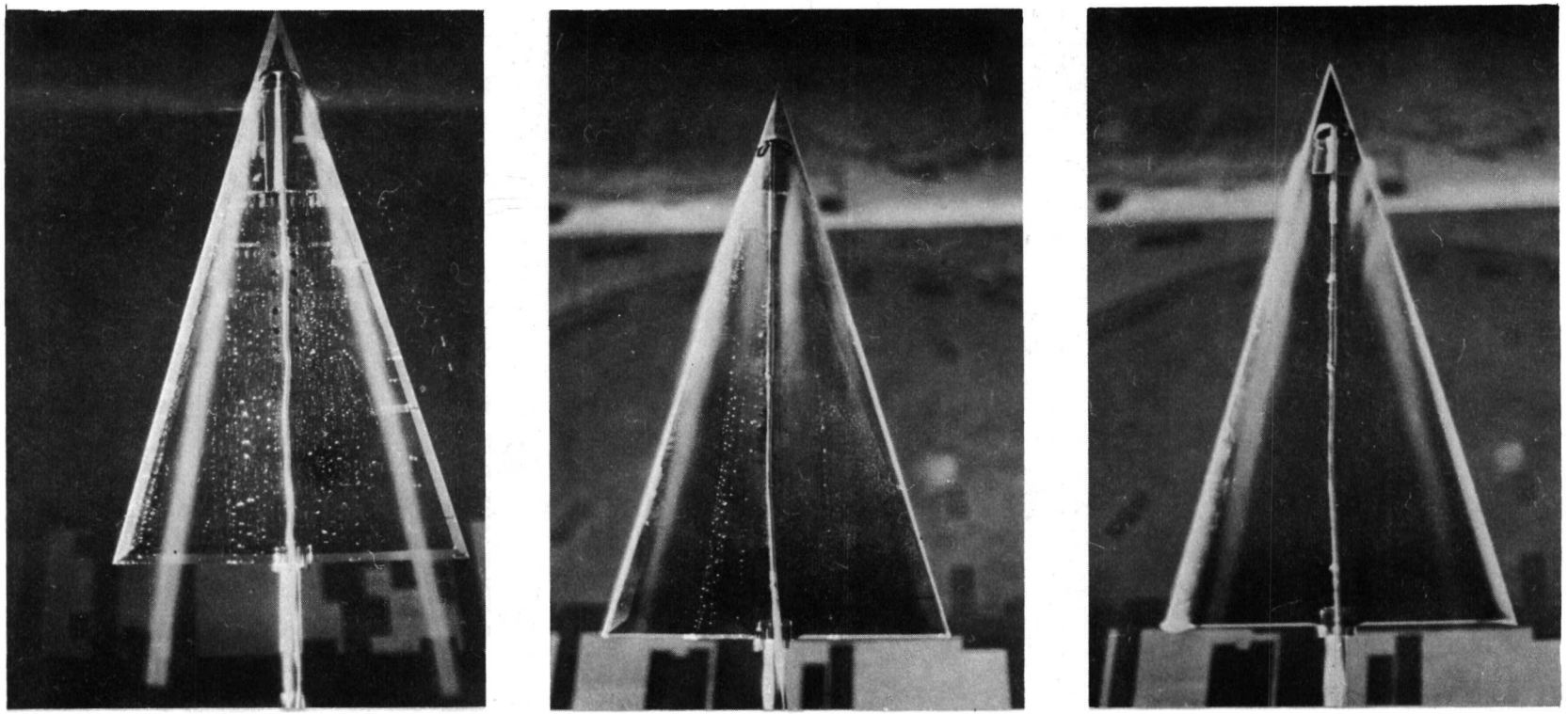

Flat Plate | Apex Camber | Conical Camber

Figure 43 - Water Vapor Patterns, $\alpha = 20°$

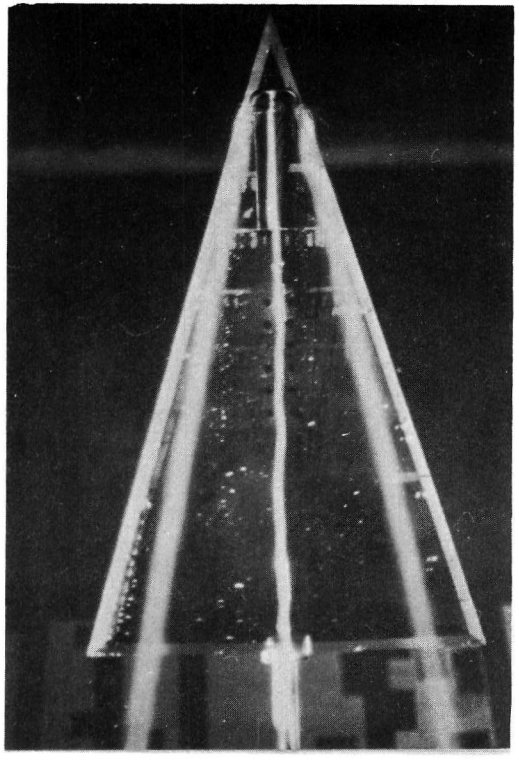

Flat Plate

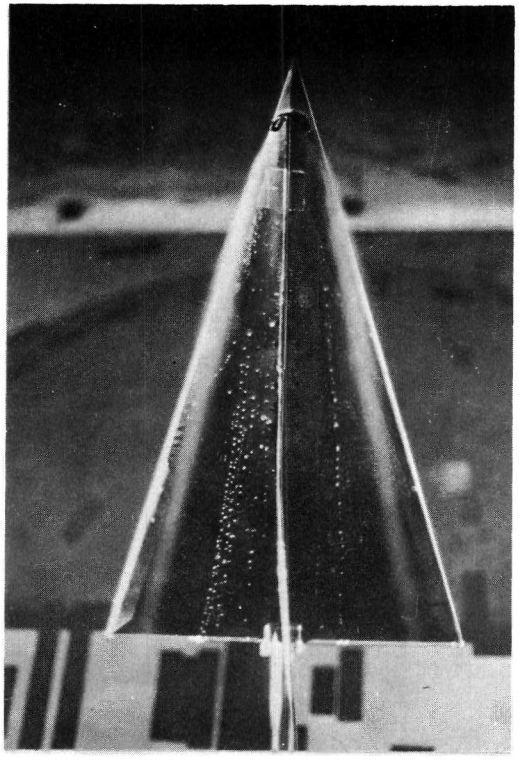

Apex Camber

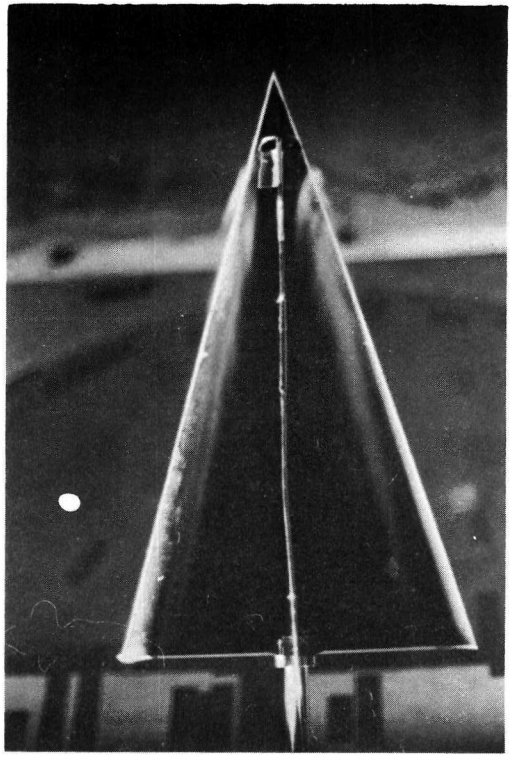

Conical Camber

Figure 44 - Water Vapor Patterns, $\alpha = 25°$

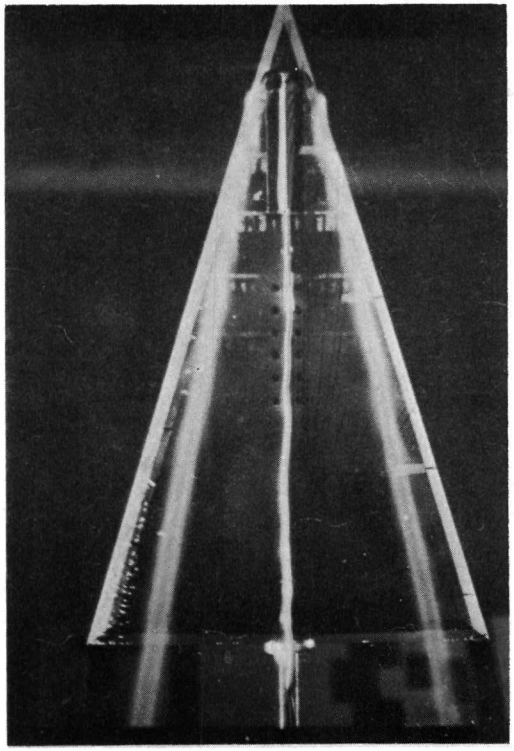

Flat Plate

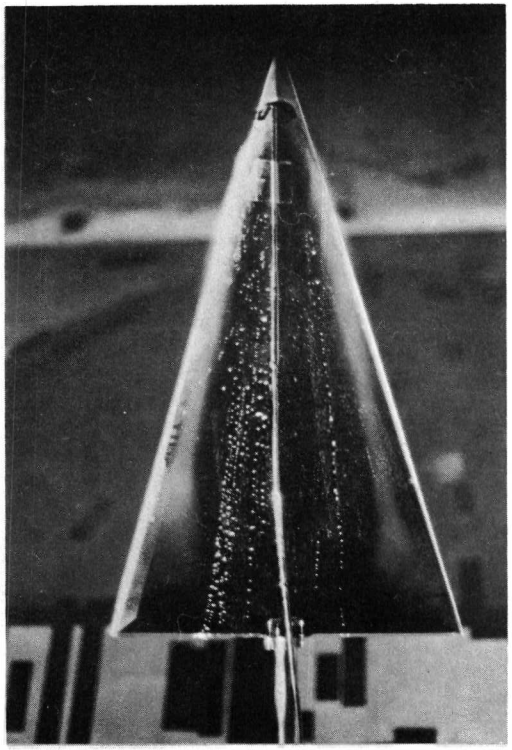

Apex Camber

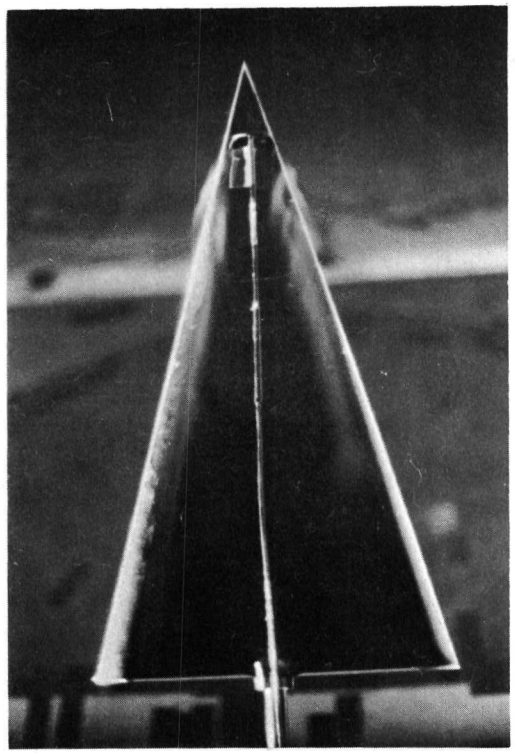

Conical Camber

Figure 45 - Water Vapor Patterns, $\alpha = 30°$

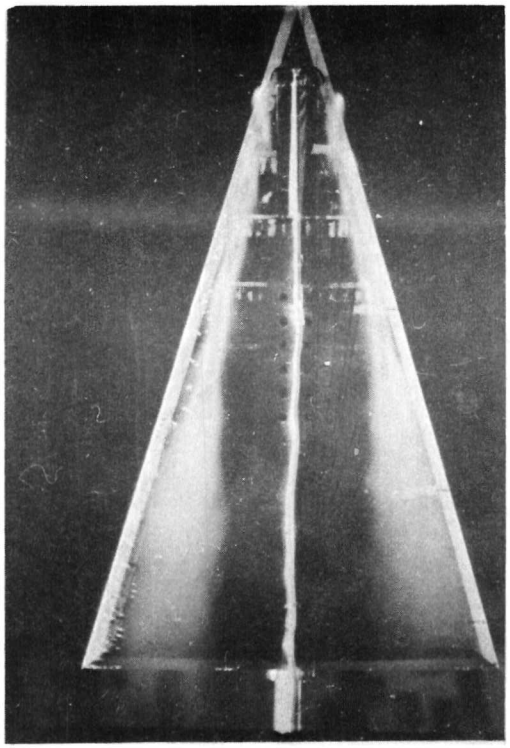

Flat Plate

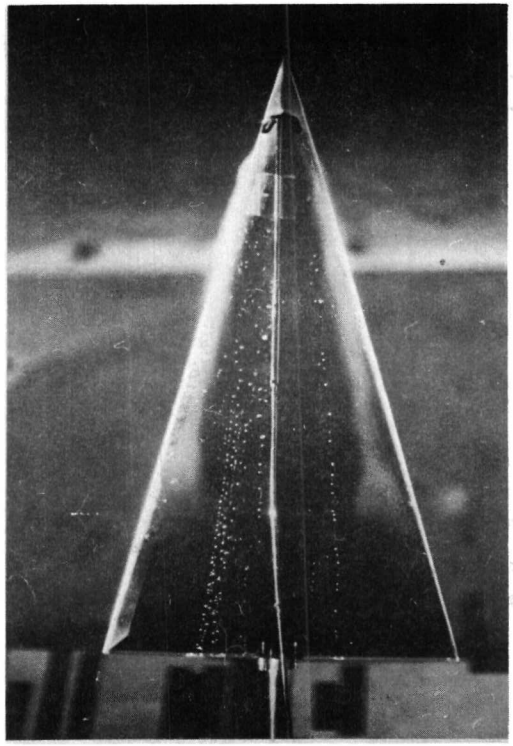

Apex Camber

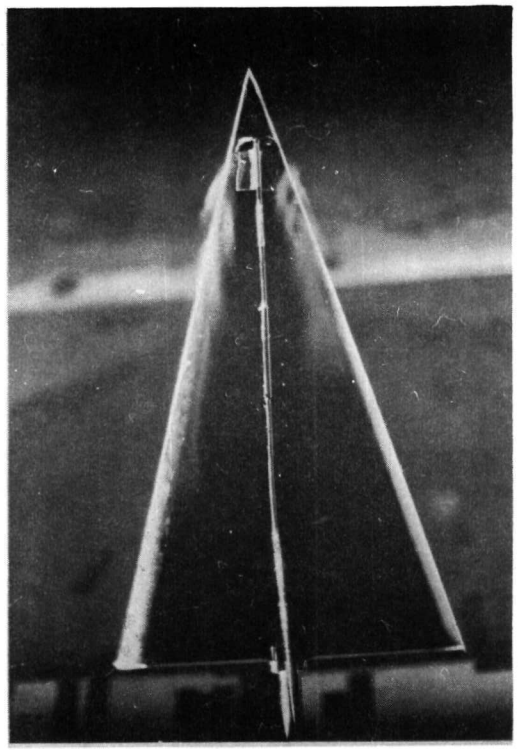

Conical Camber

Figure 46 - Water Vapor Patterns, $\alpha = 35°$

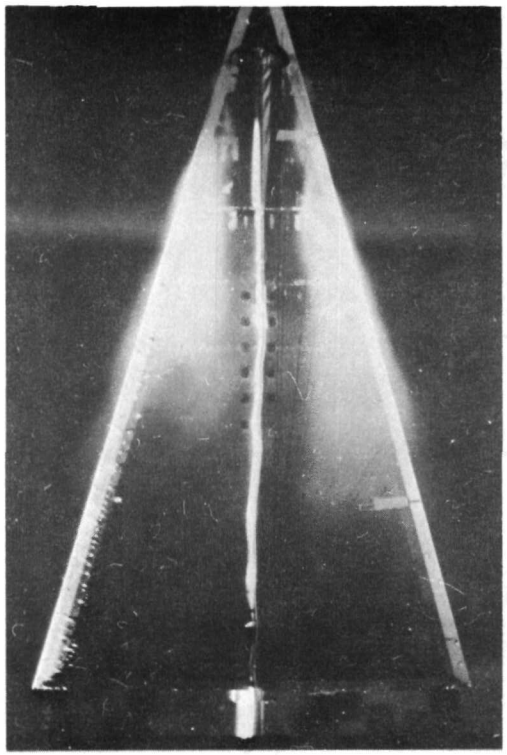

Flat Plate

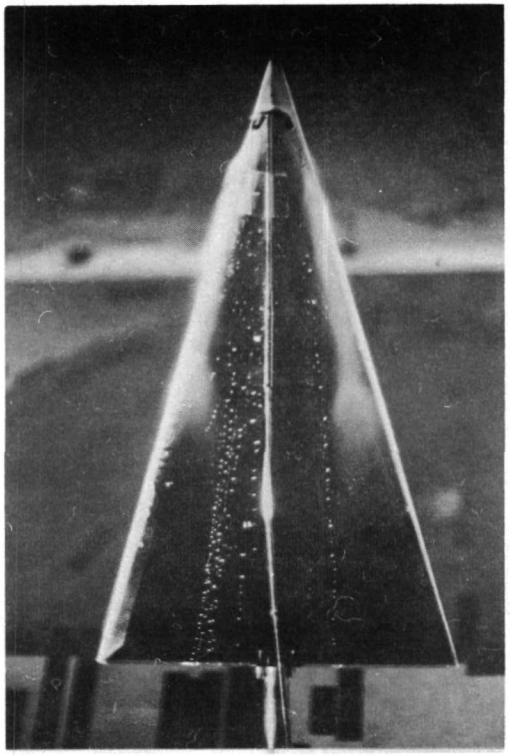

Apex Camber

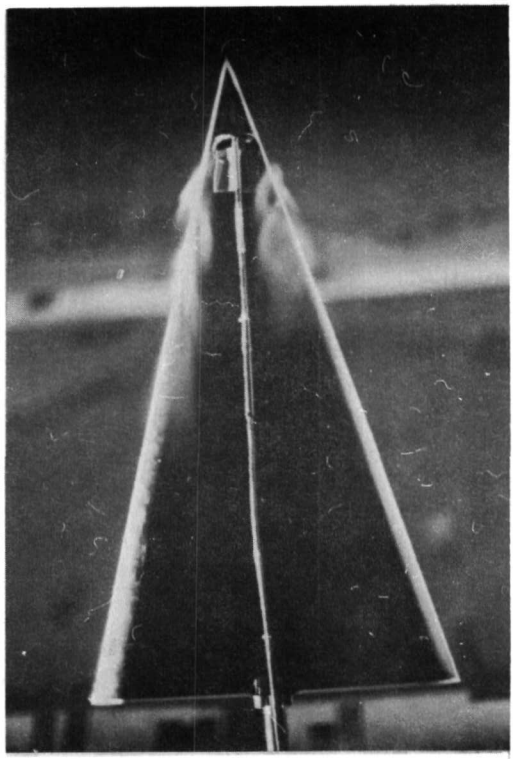

Conical Camber

Figure 47 - Water Vapor Patterns, $\alpha = 40°$

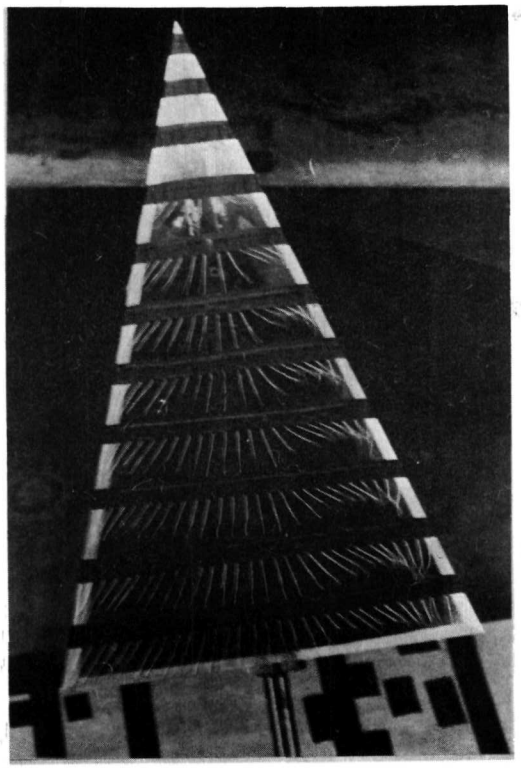

Flat Plate

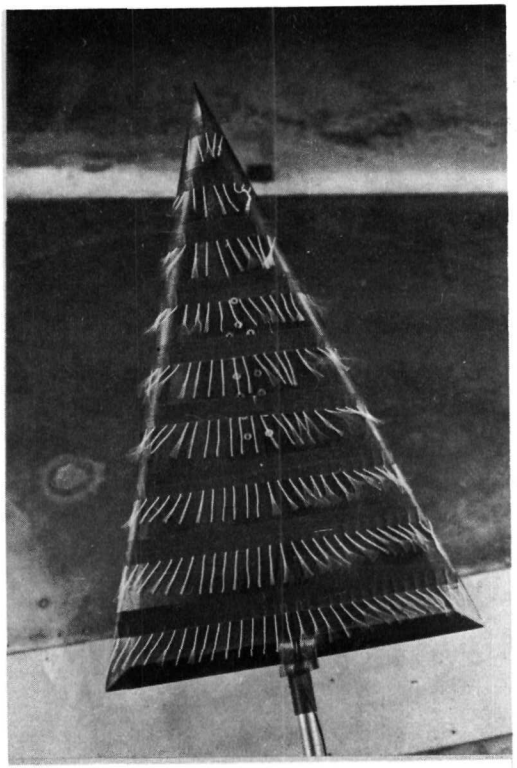

Apex Camber

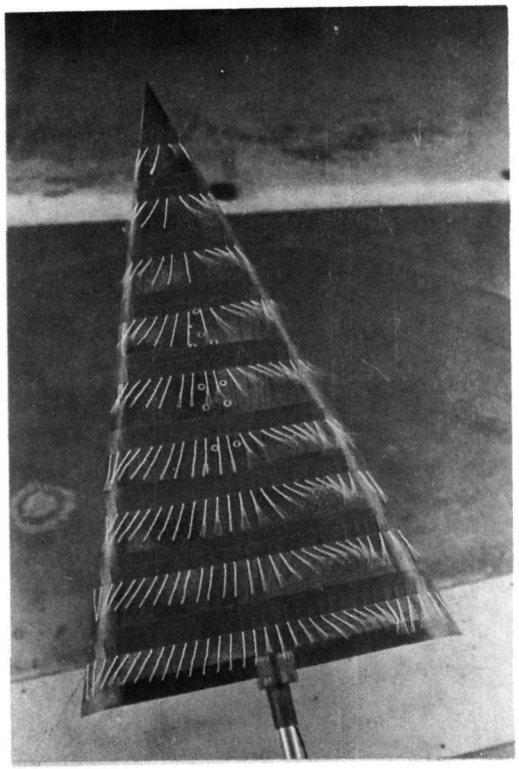

Conical Camber

Figure 48 - Tuft Patterns, $\alpha = 20°$, $\beta = 10°$

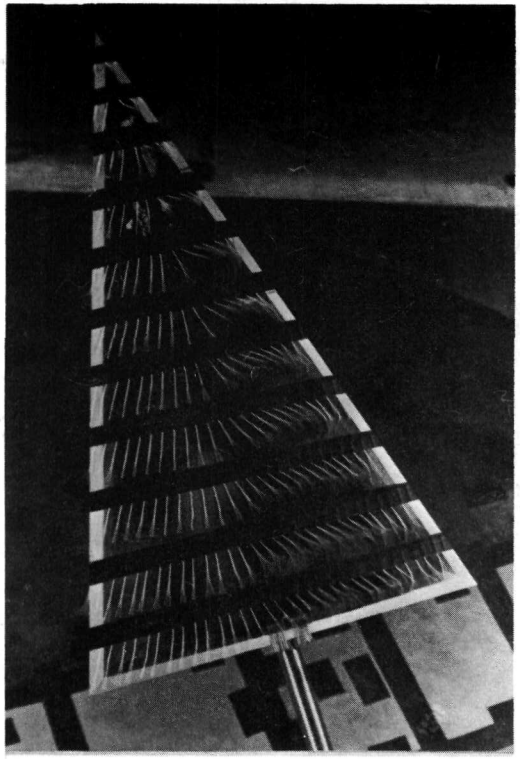

Flat Plate

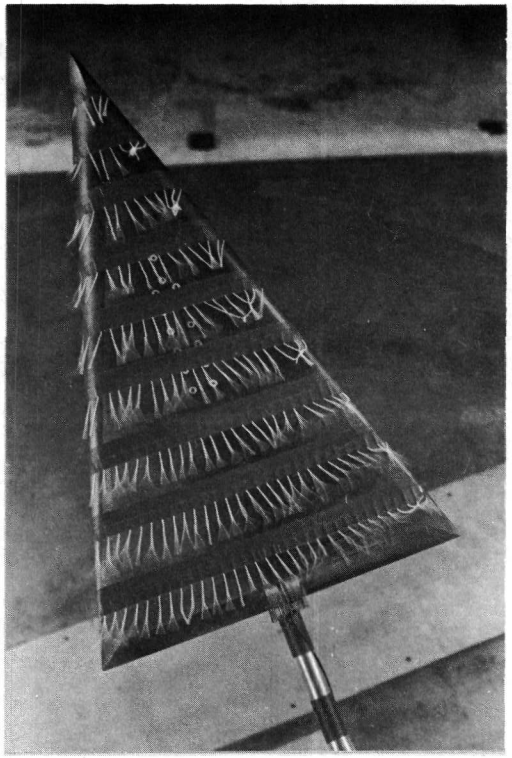

Apex Camber

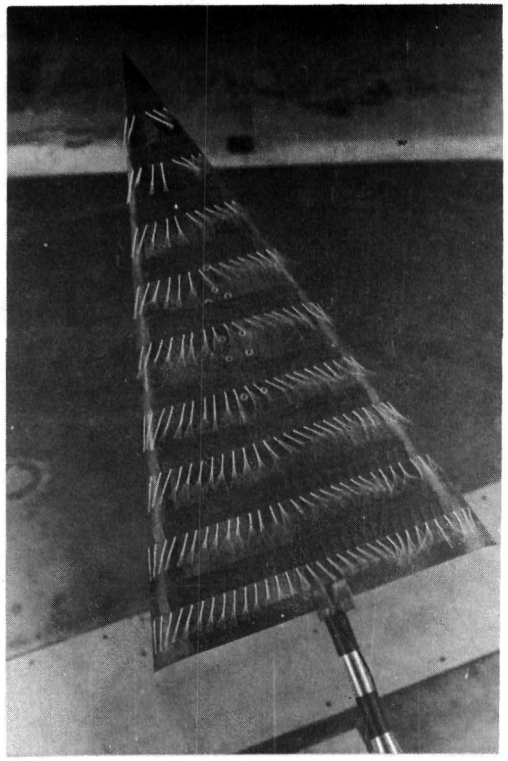

Conical Camber

Figure 49 - Tuft Patterns, $\alpha = 20°$, $\beta = 20°$

Flat Plate

Apex Camber

Conical Camber

Figure 50 - Tuft Patterns, $\alpha = 20°$, $\beta = 30°$

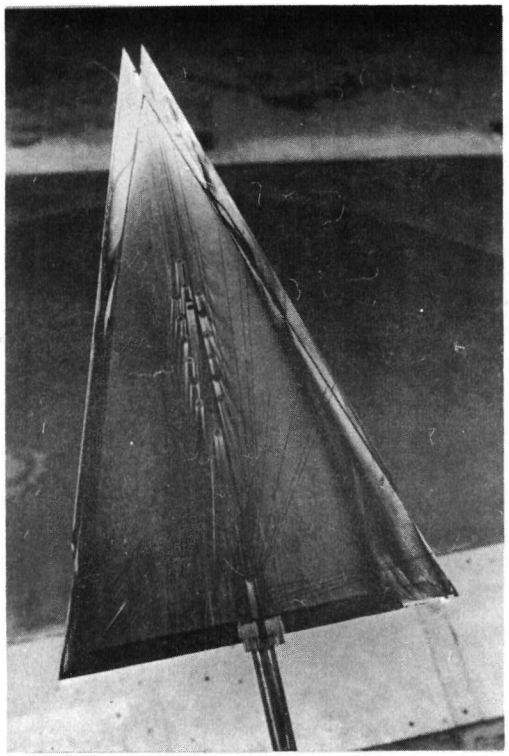

Flat Plate

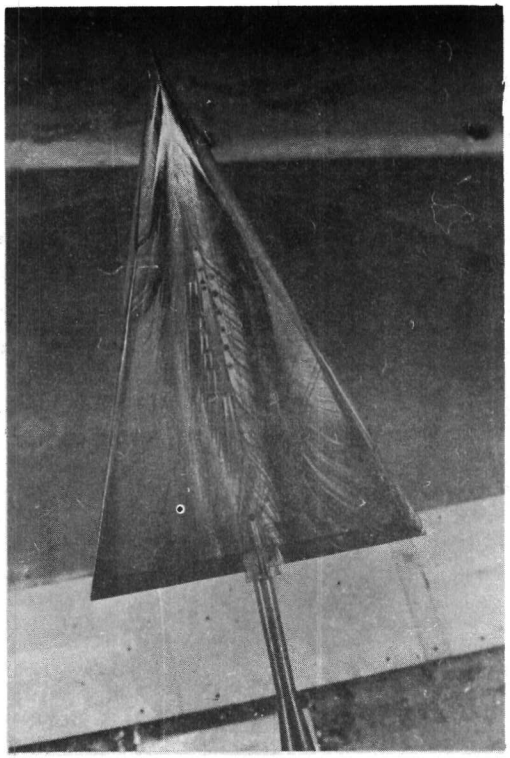

Apex Camber

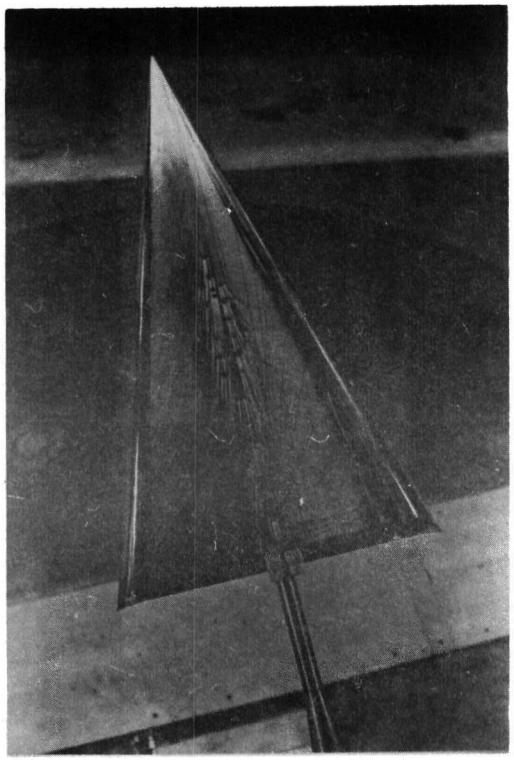

Conical Camber

Figure 51 - Oil Flow Patterns, $\alpha = 20°$, $\beta = 10°$

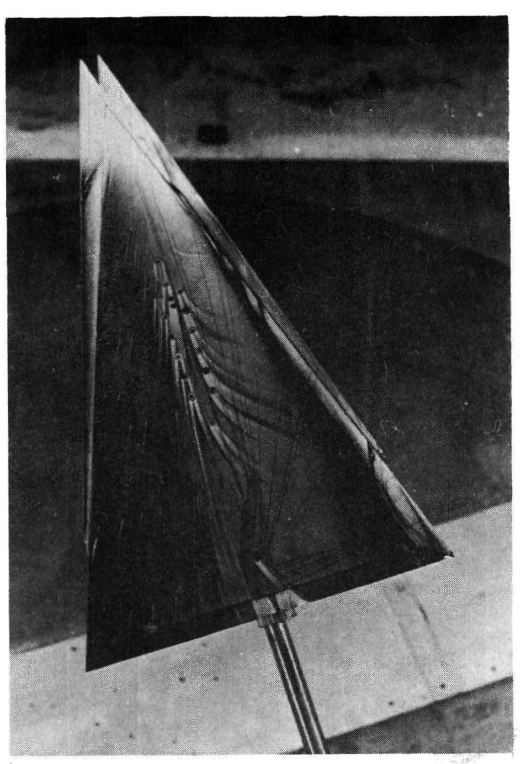

Flat Plate

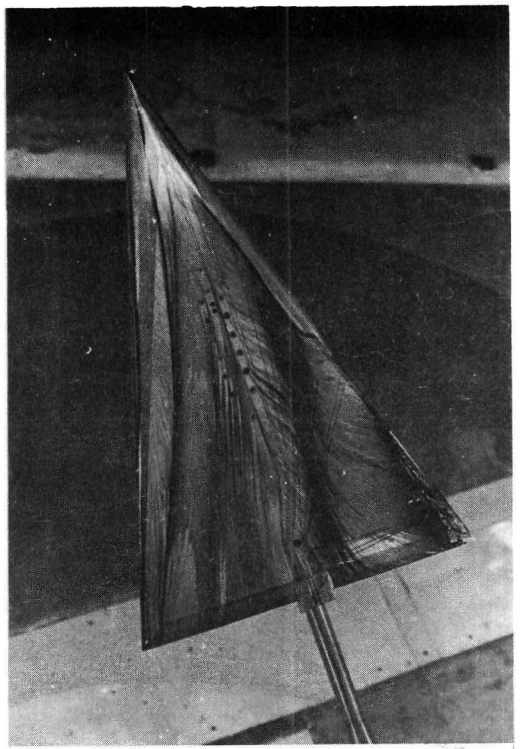

Apex Camber

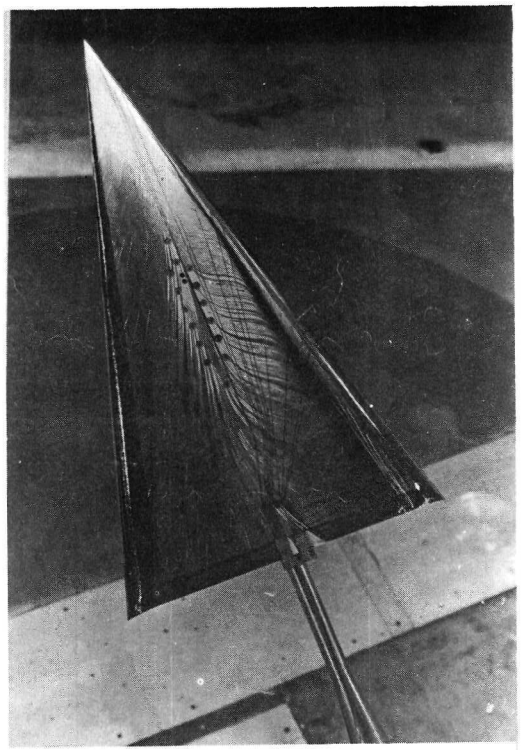

Conical Camber

Figure 52 - Oil Flow Patterns, $\alpha = 20°$, $\beta = 20°$

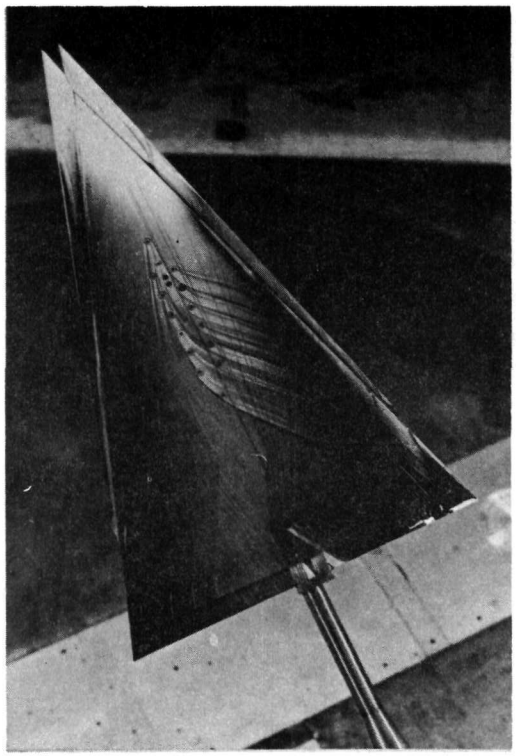

Flat Plate

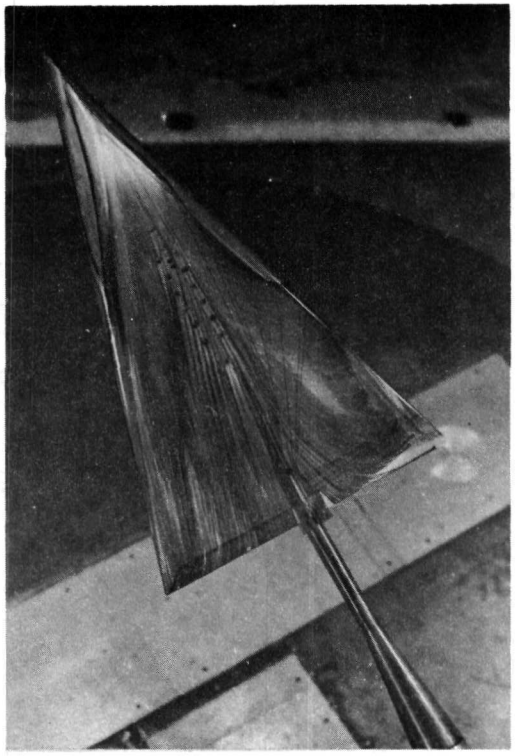

Apex Camber

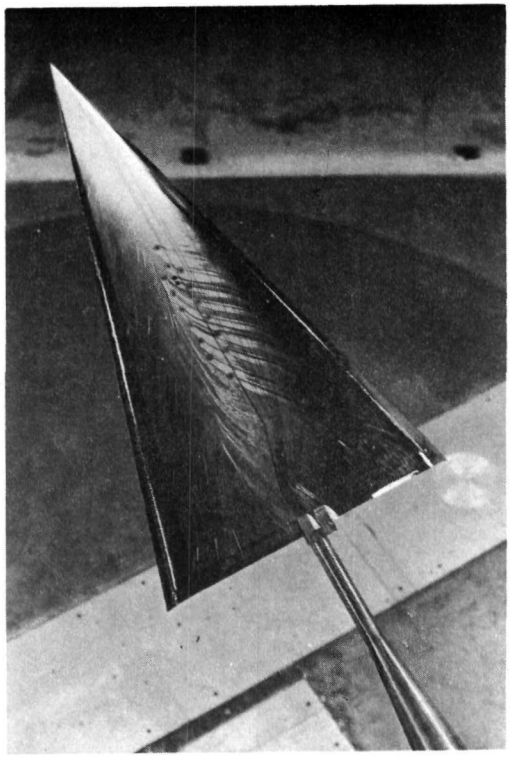

Conical Camber

Figure 53 - Oil Flow Patterns, $\alpha = 20°$, $\beta = 30°$

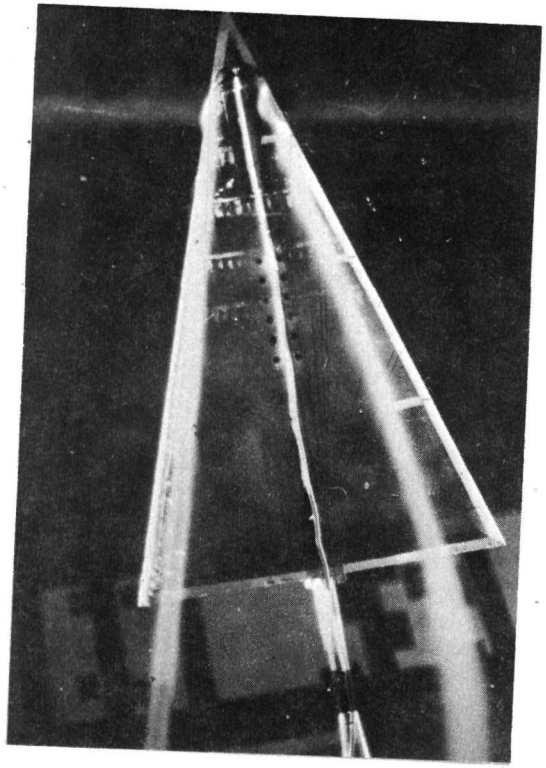

Flat Plate

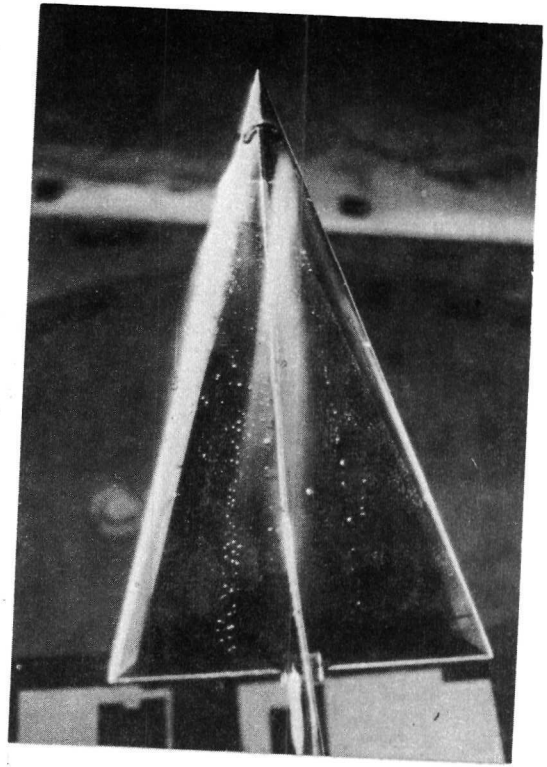

Apex Camber

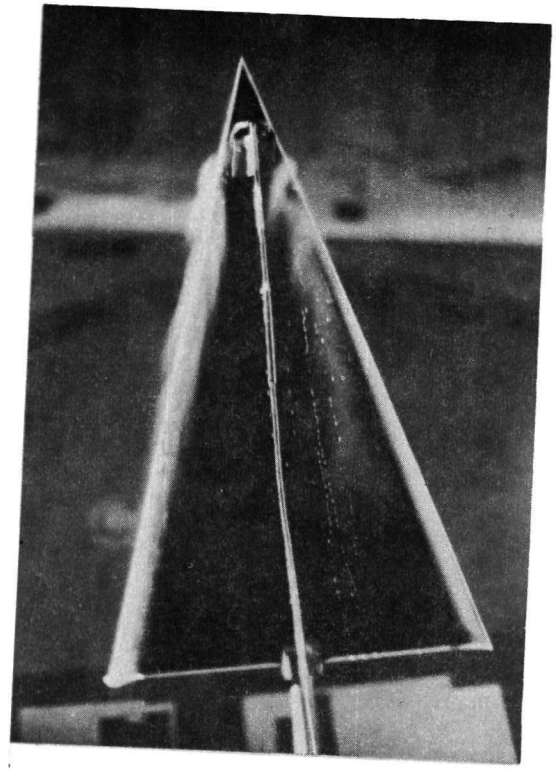

Conical Camber

Figure 54 - Water Vapor Patterns, $\alpha = 20°$, $\beta = 10°$

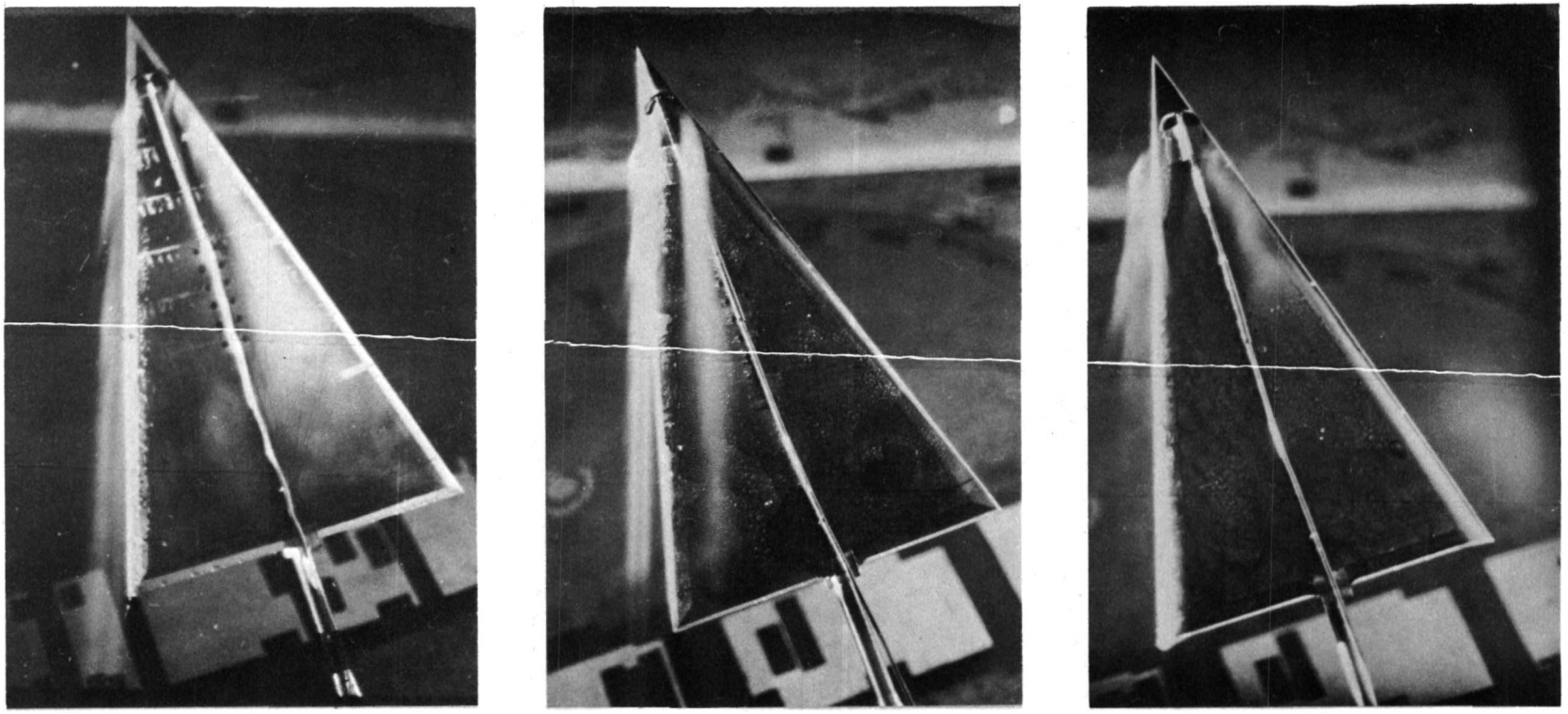

Flat Plate

Apex Camber

Conical Camber

Figure 55 - Water Vapor Patterns, $\alpha = 20°$, $\beta = 20°$

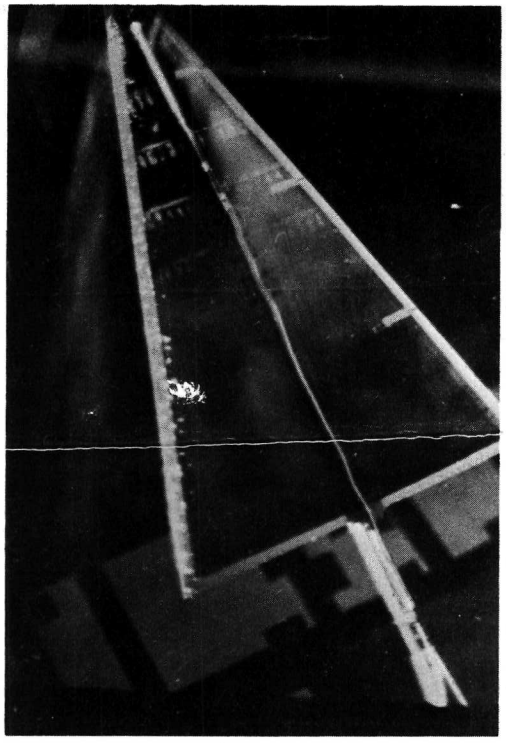

Flat Plate

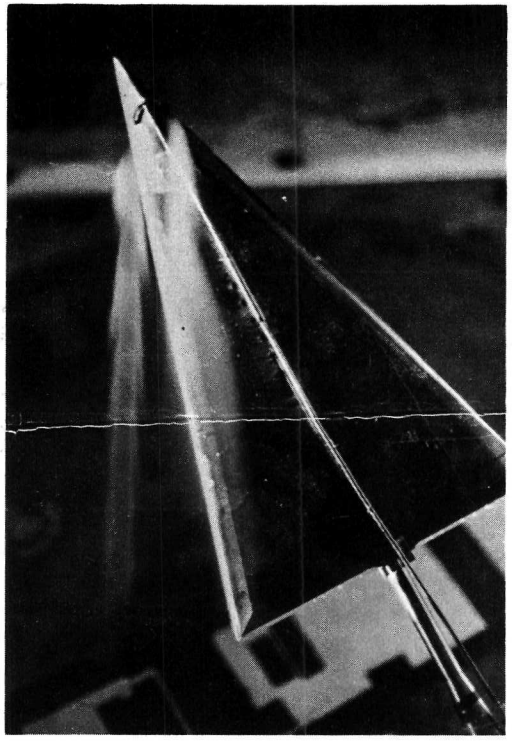

Apex Camber

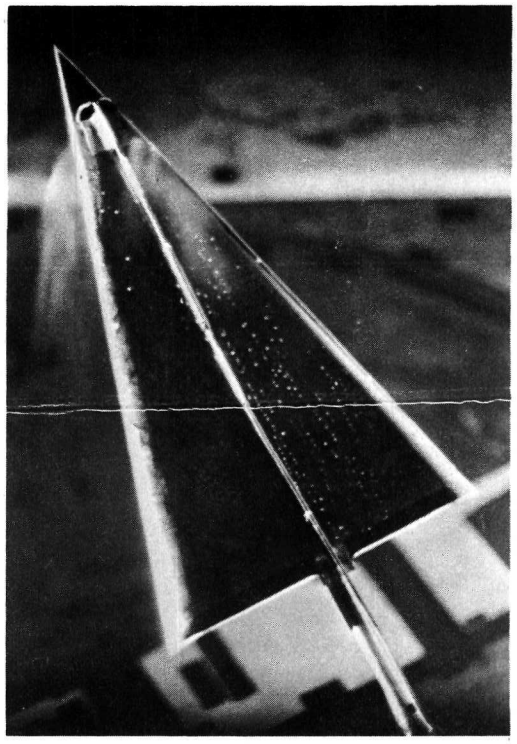

Conical Camber

Figure 56 - Water Vapor Patterns, $\alpha = 20°$, $\beta = 30°$

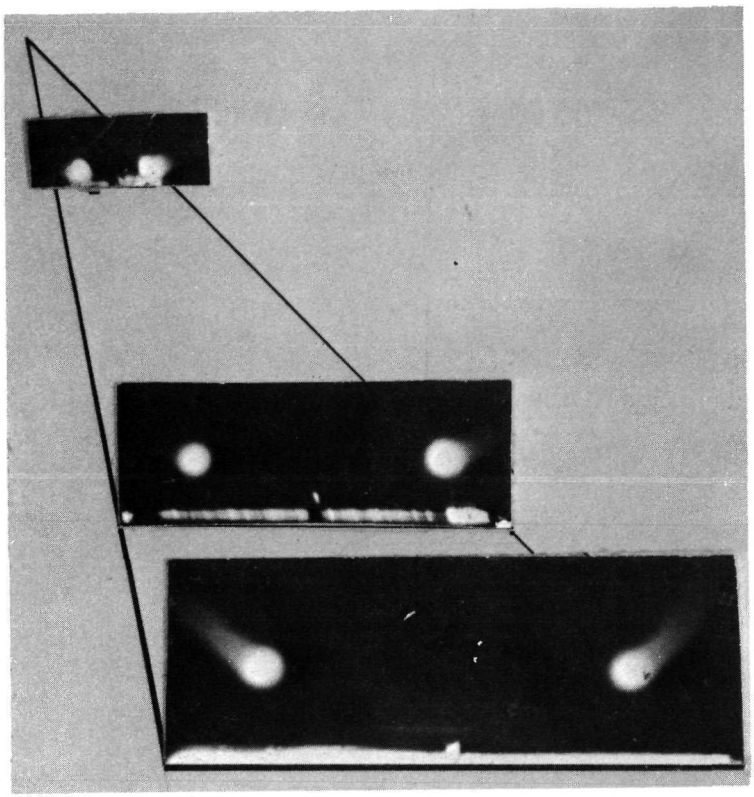

Figure 57 - Water Vapor Cross Flow Patterns
Flat Plate Model, $\alpha = 20°$, $\beta = 0°$

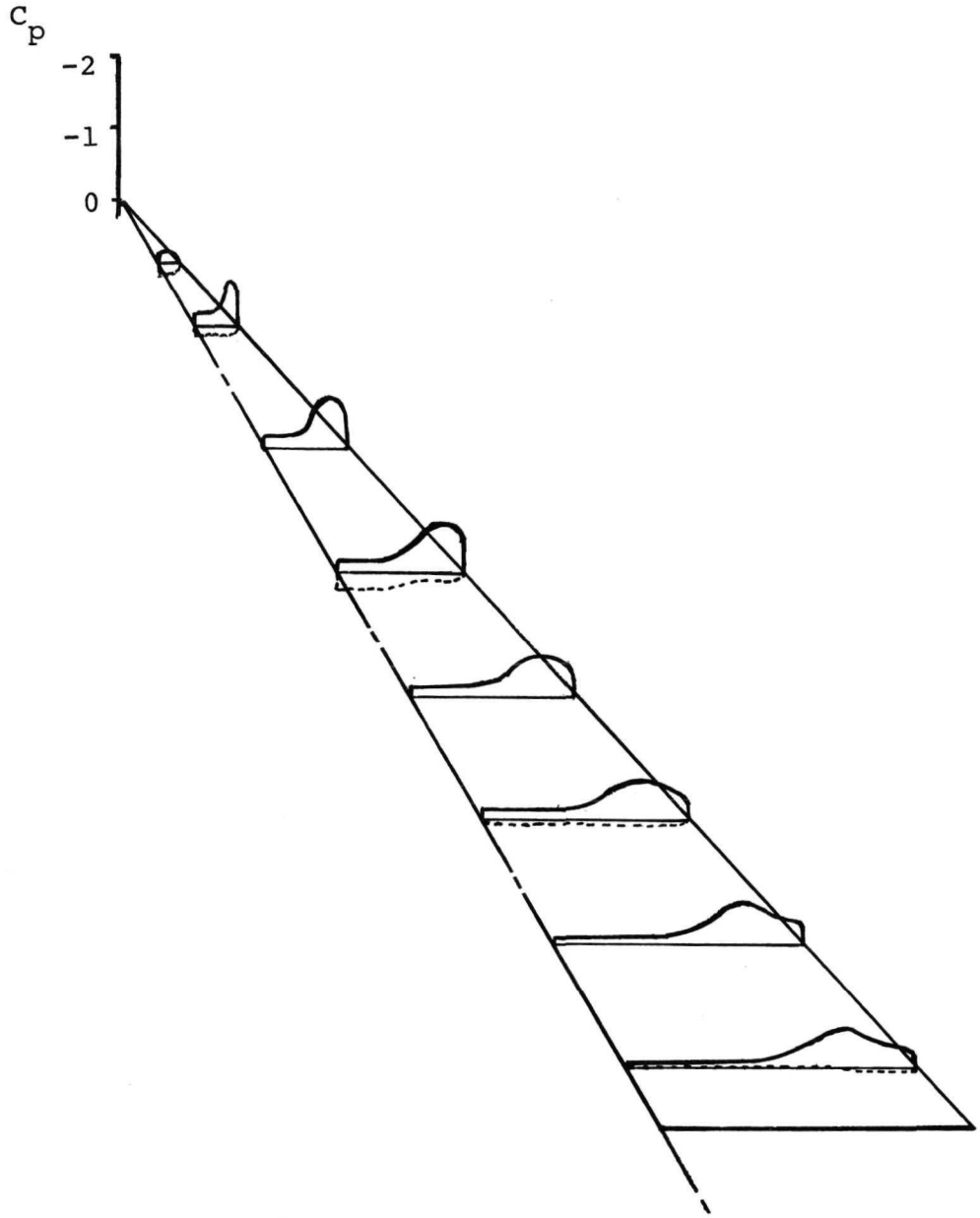

Figure 58 - Pressure Distribution - Flat Plate Model, $\alpha = 10°$, $\beta = 0°$

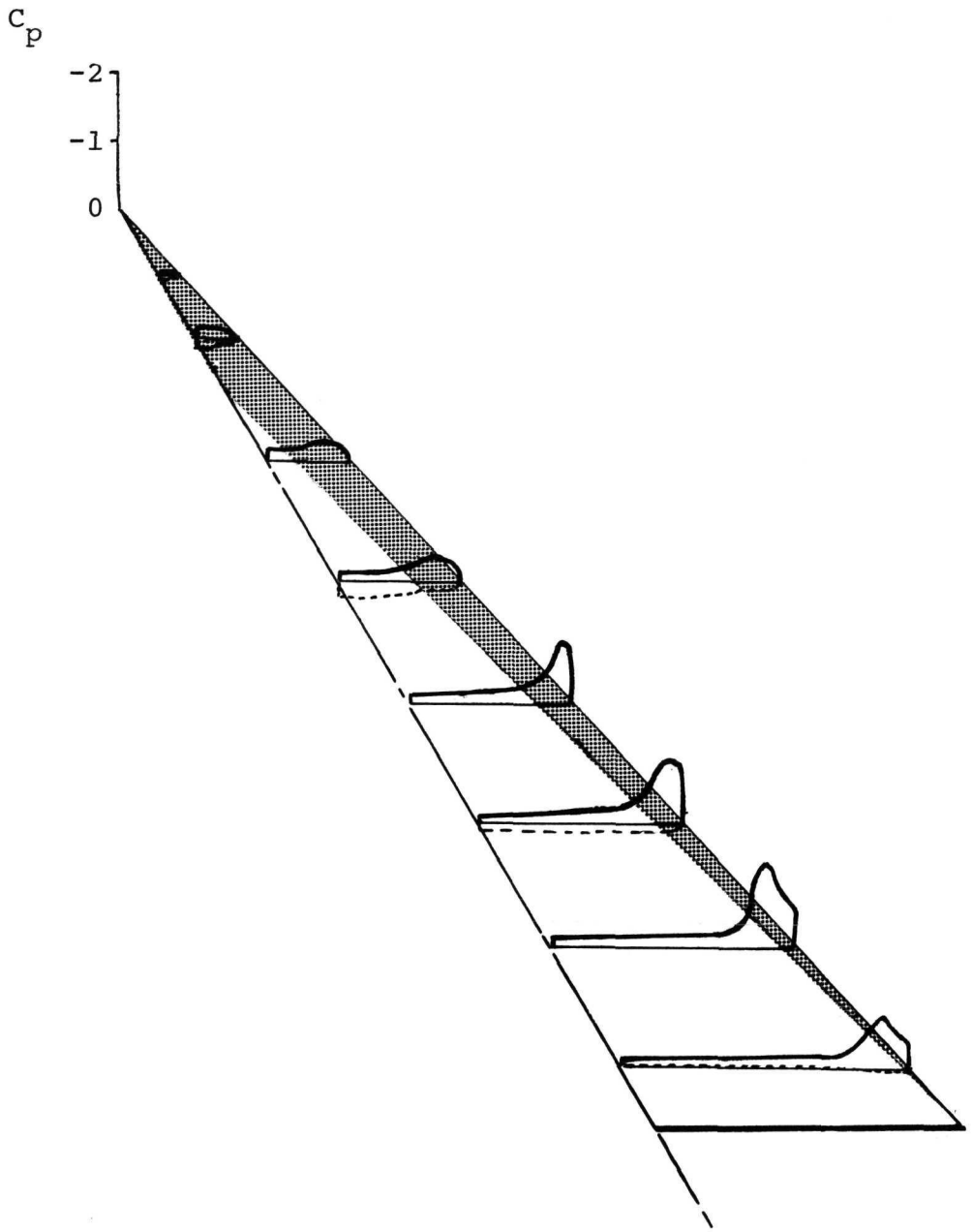

Figure 59 - Pressure Distribution - Apex Camber Model, $\alpha = 10°$, $\beta = 0°$

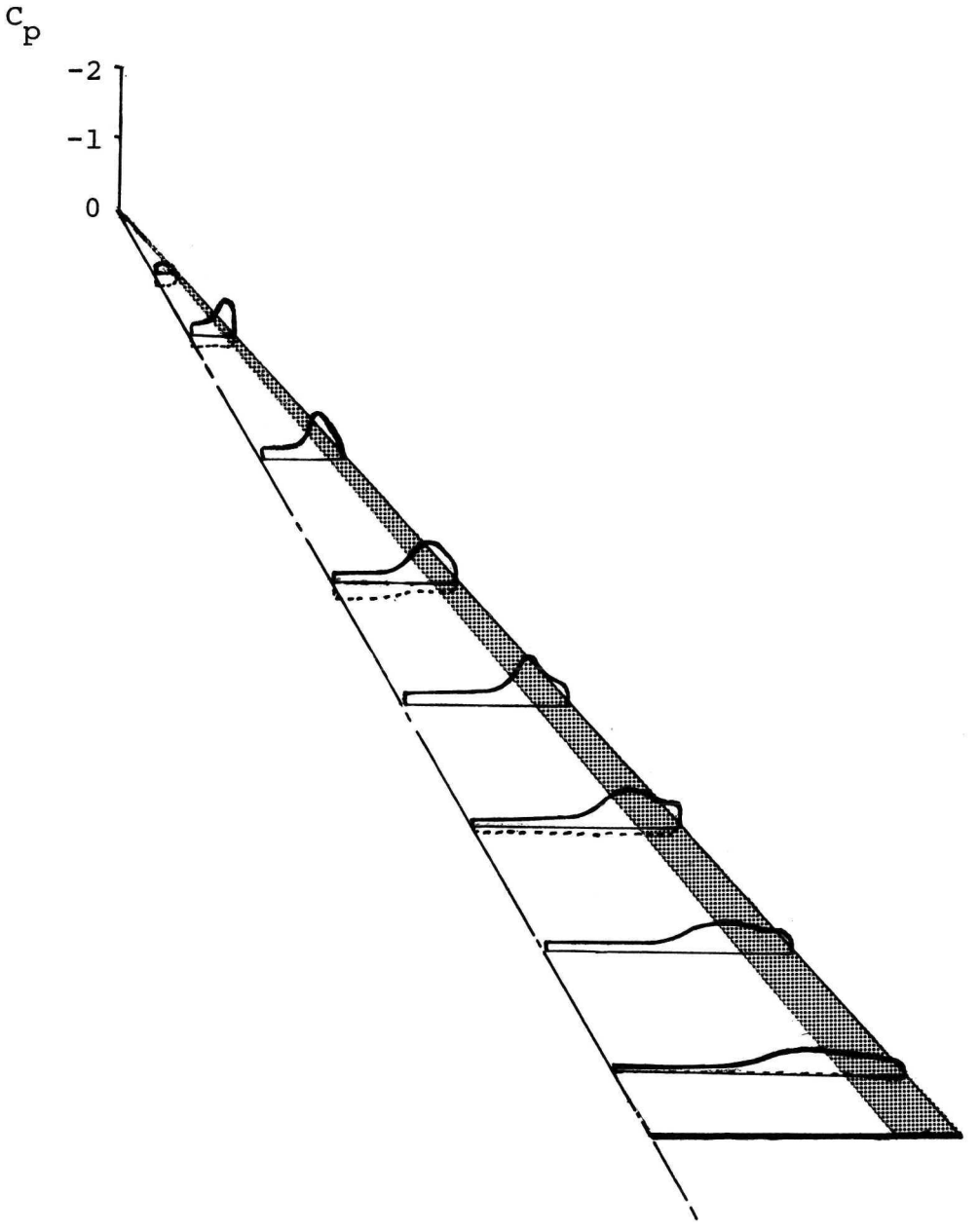

Figure 60 - Pressure Distribution - Conical Camber Model, $\alpha = 10°$, $\beta = 0°$

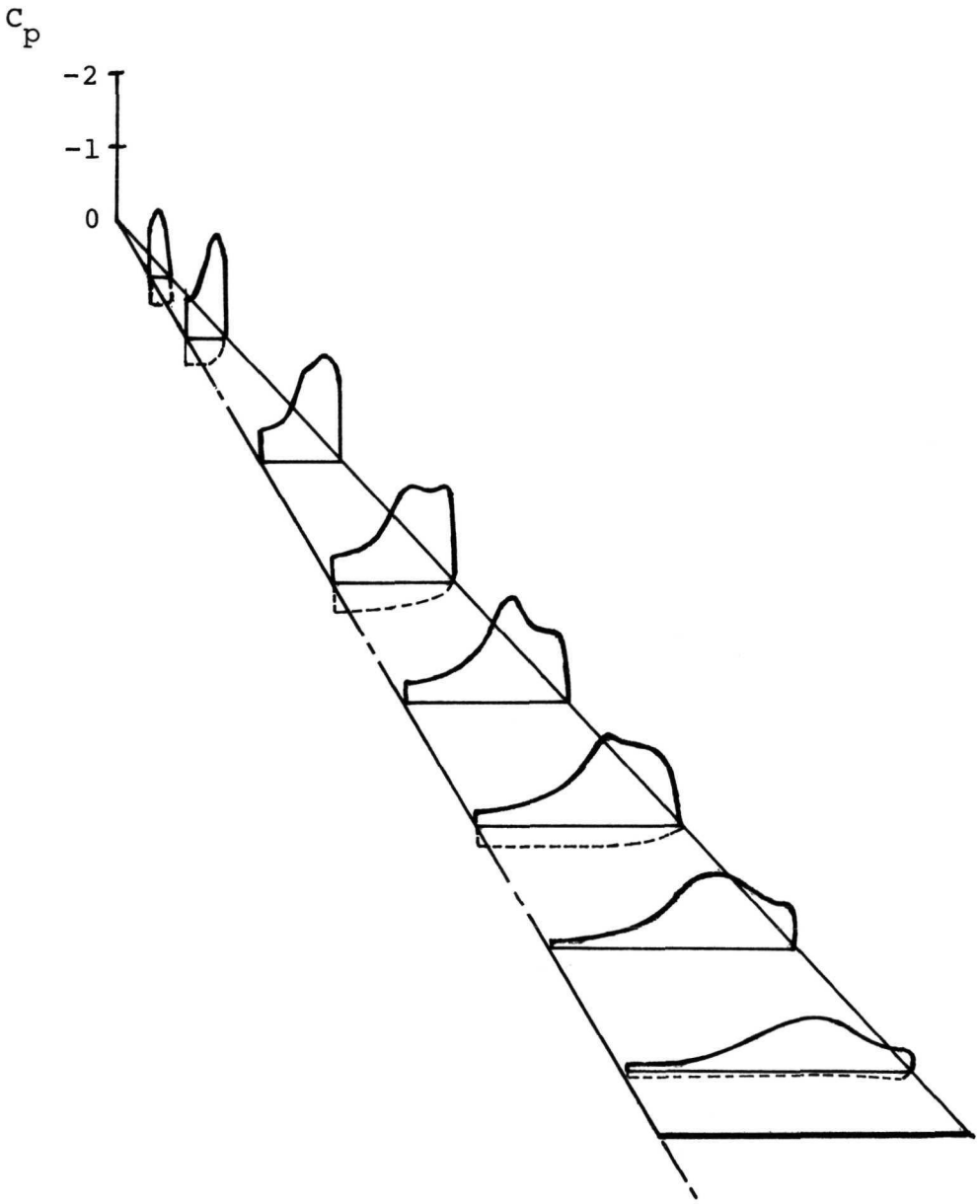

Figure 61 - Pressure Distribution - Flat Plate Model, $\alpha = 20°$, $\beta = 0°$

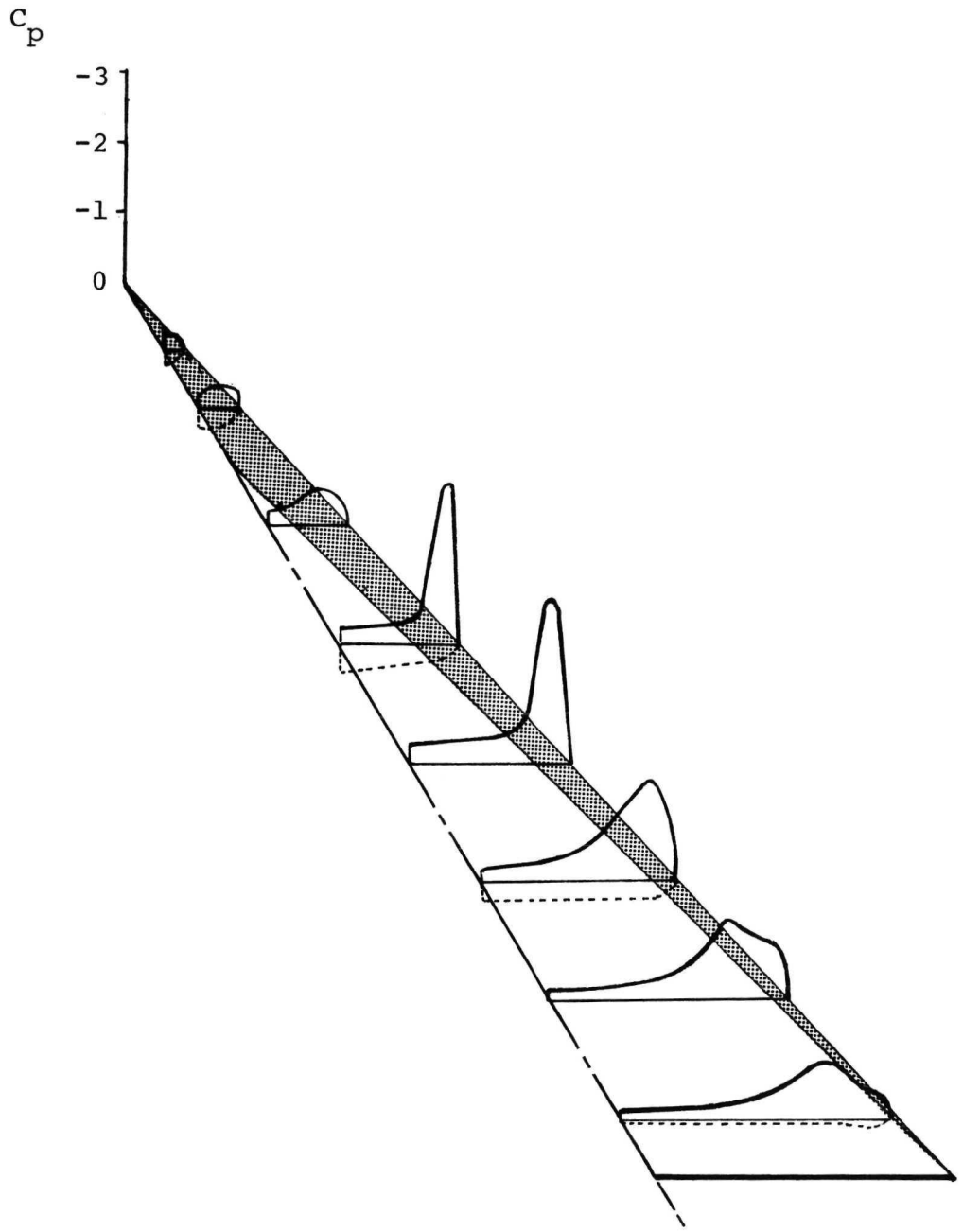

Figure 62 - Pressure Distribution - Apex Camber Model, $\alpha = 20°$, $\beta = 0°$

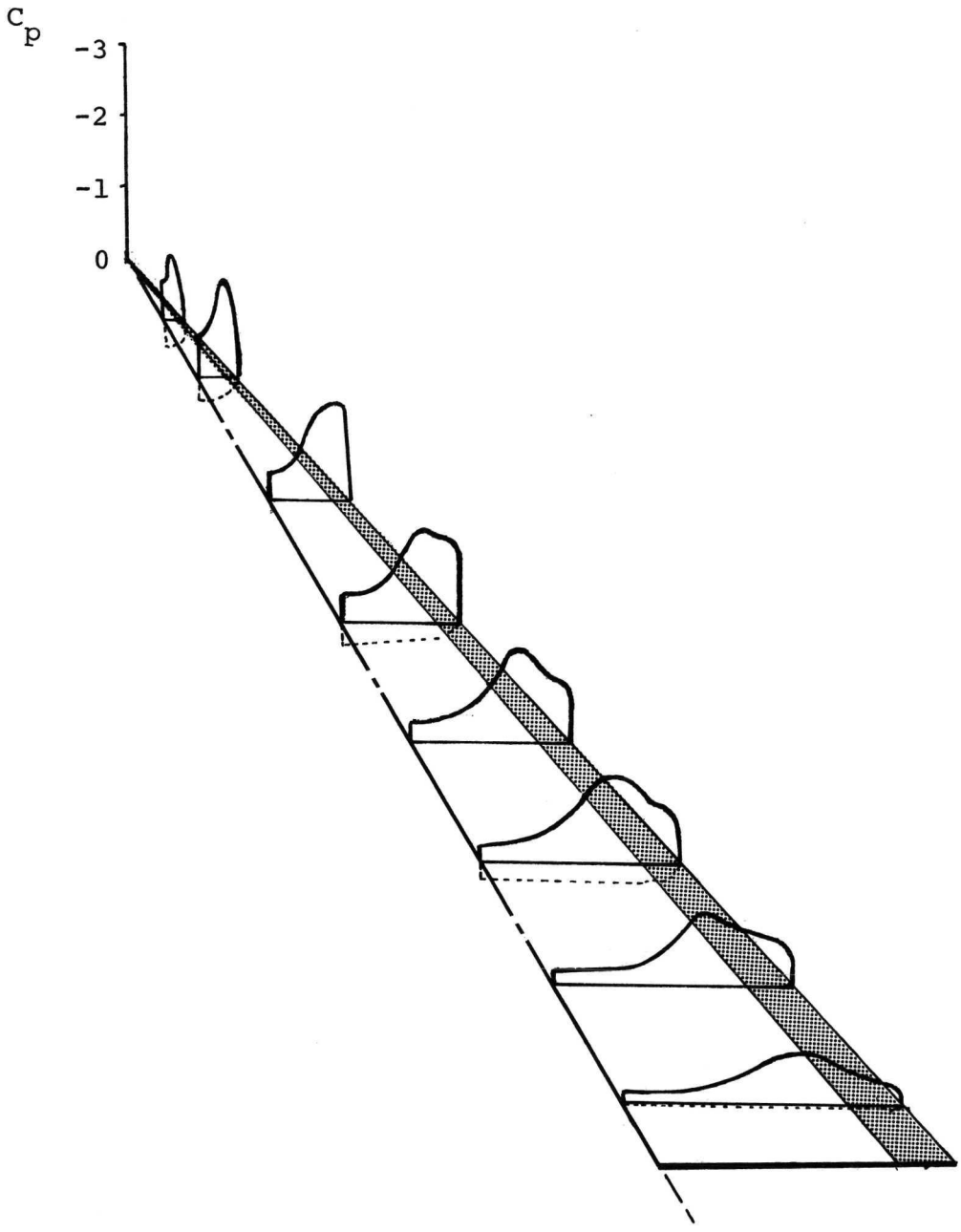

Figure 63 - Pressure Distribution - Conical Camber Model, $\alpha = 20°$, $\beta = 0°$

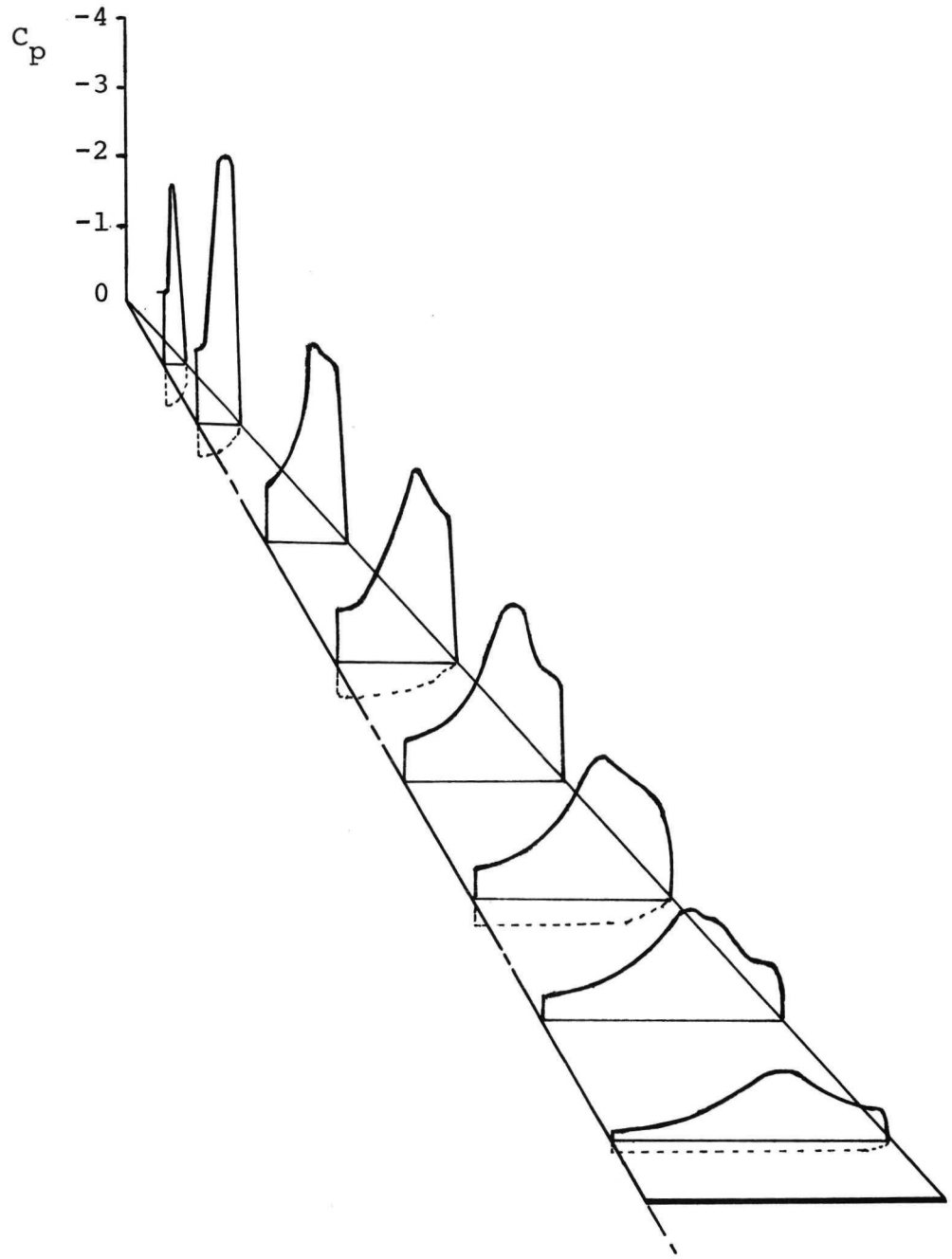

Figure 64 - Pressure Distribution - Flat Plate Model, $\alpha = 30°$, $\beta = 0°$

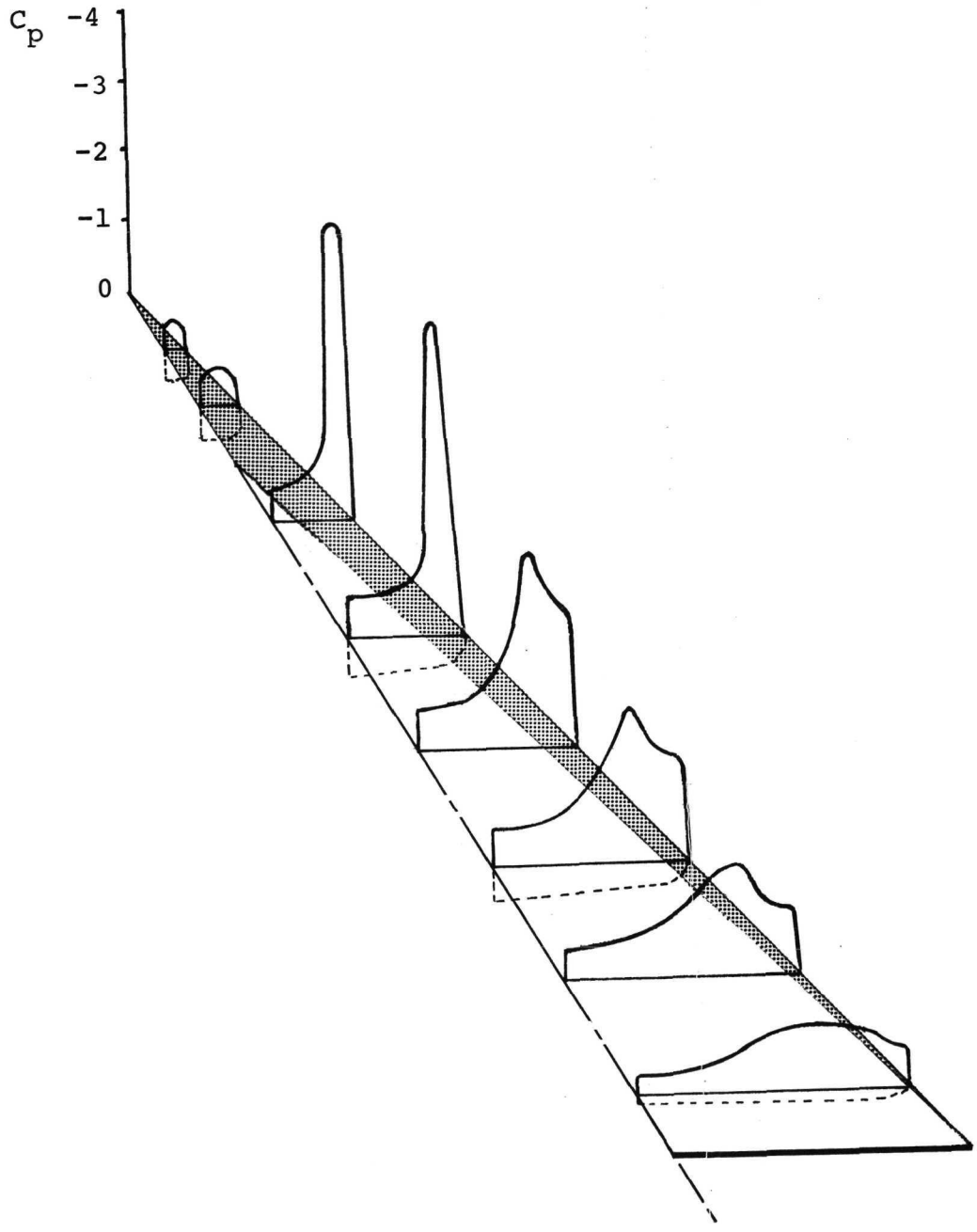

Figure 65 - Pressure Distribution - Apex Camber Model, $\alpha = 30°$, $\beta = 0°$

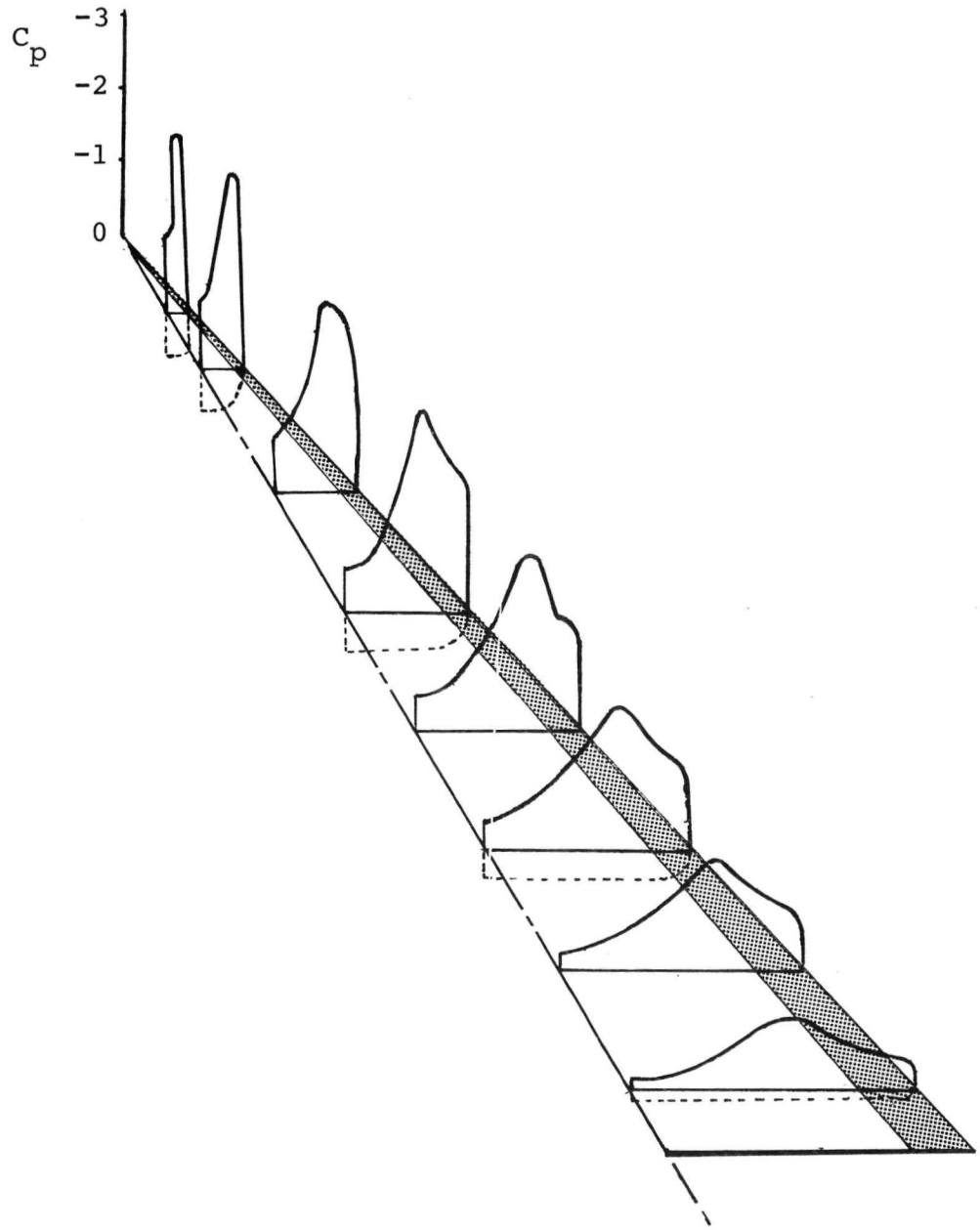

Figure 66 - Pressure Distribution - Conical Camber Model, $\alpha = 30°$, $\beta = 0°$

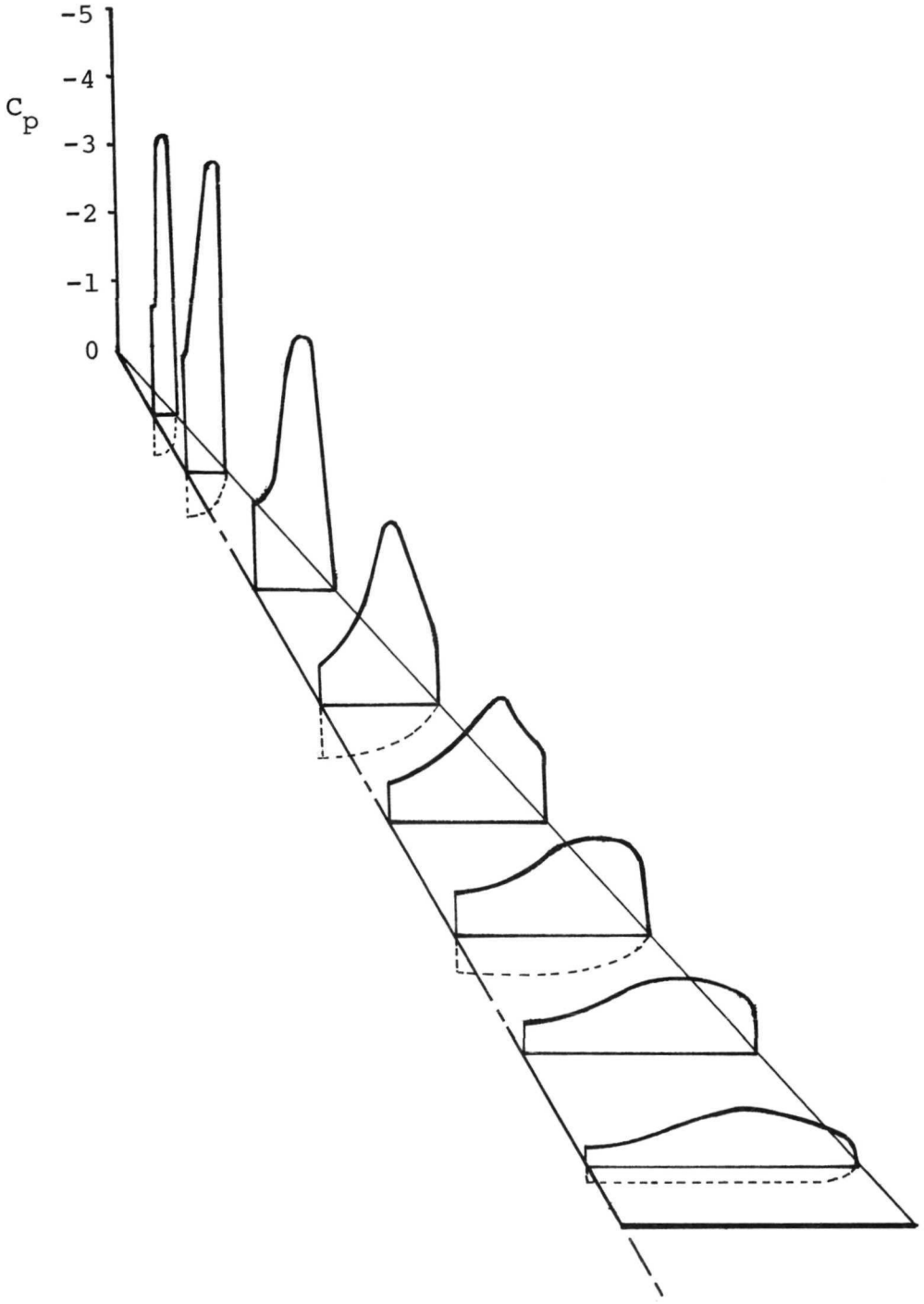

Figure 67 - Pressure Distribution - Flat Plate Model, $\alpha = 40°$, $\beta = 0°$

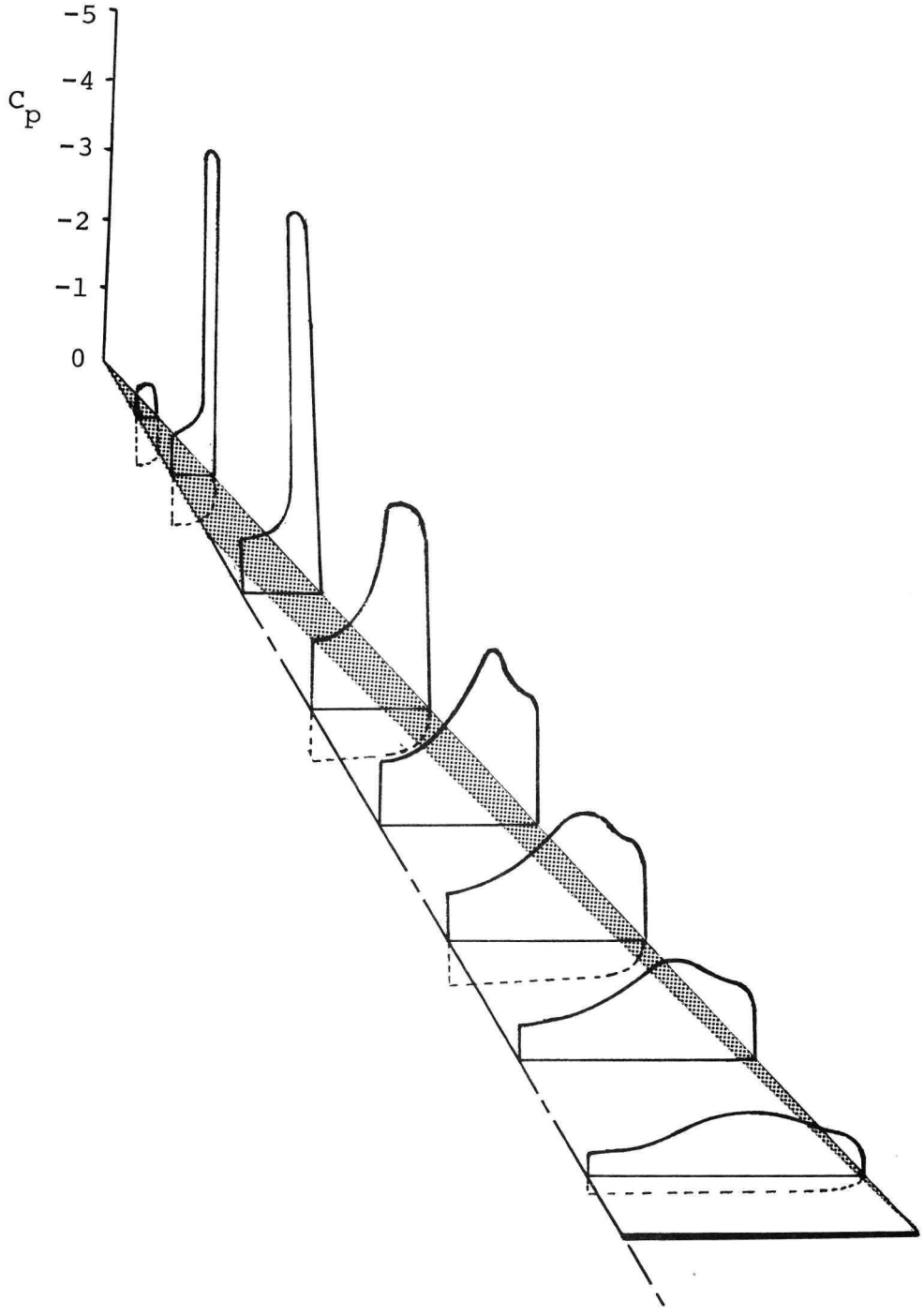

Figure 68 - Pressure Distribution - Apex Camber Model, $\alpha = 40°$, $\beta = 0°$

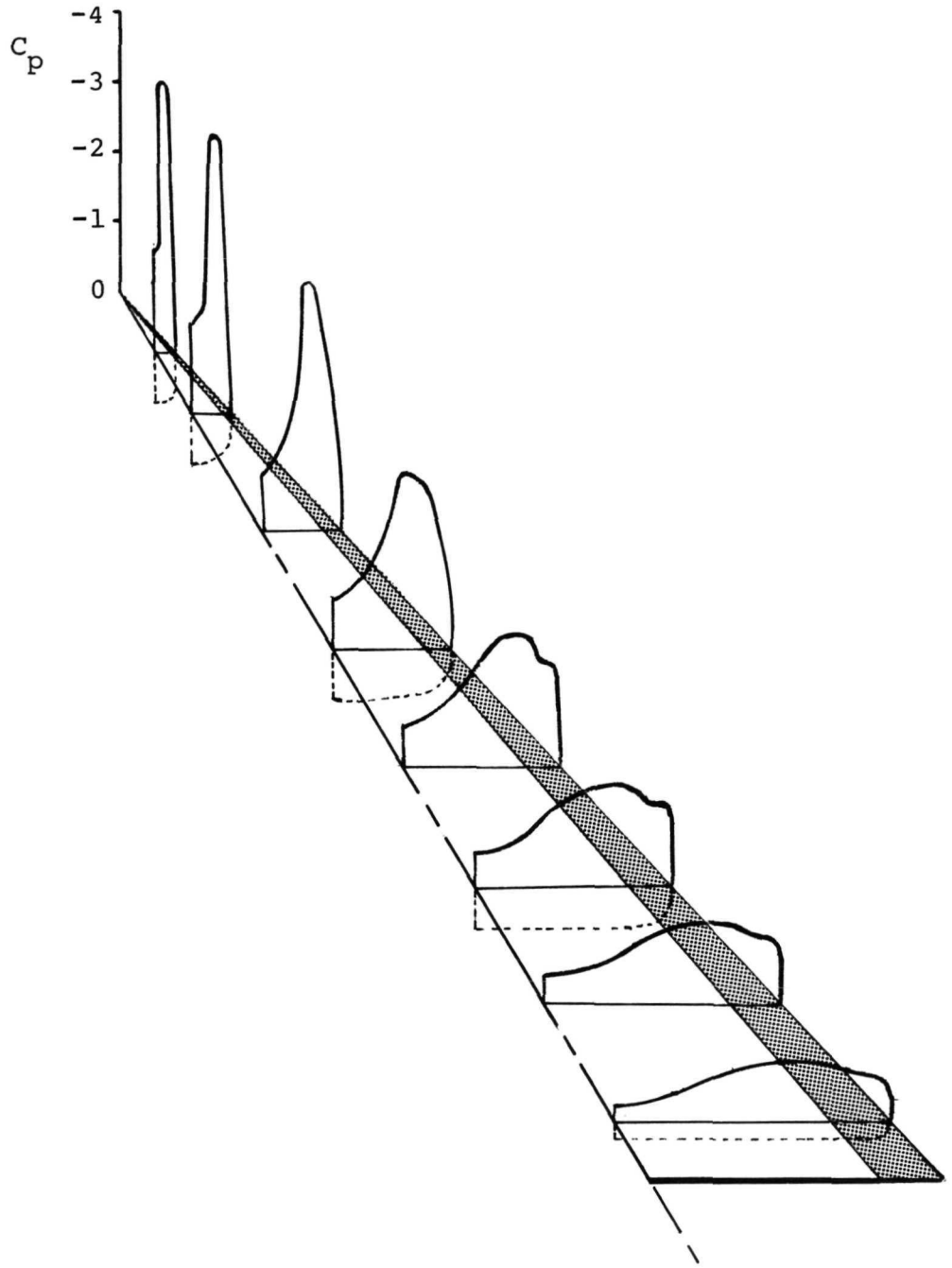

Figure 69 - Pressure Distribution - Conical Camber Model, $\alpha = 40°$, $\beta = 0°$

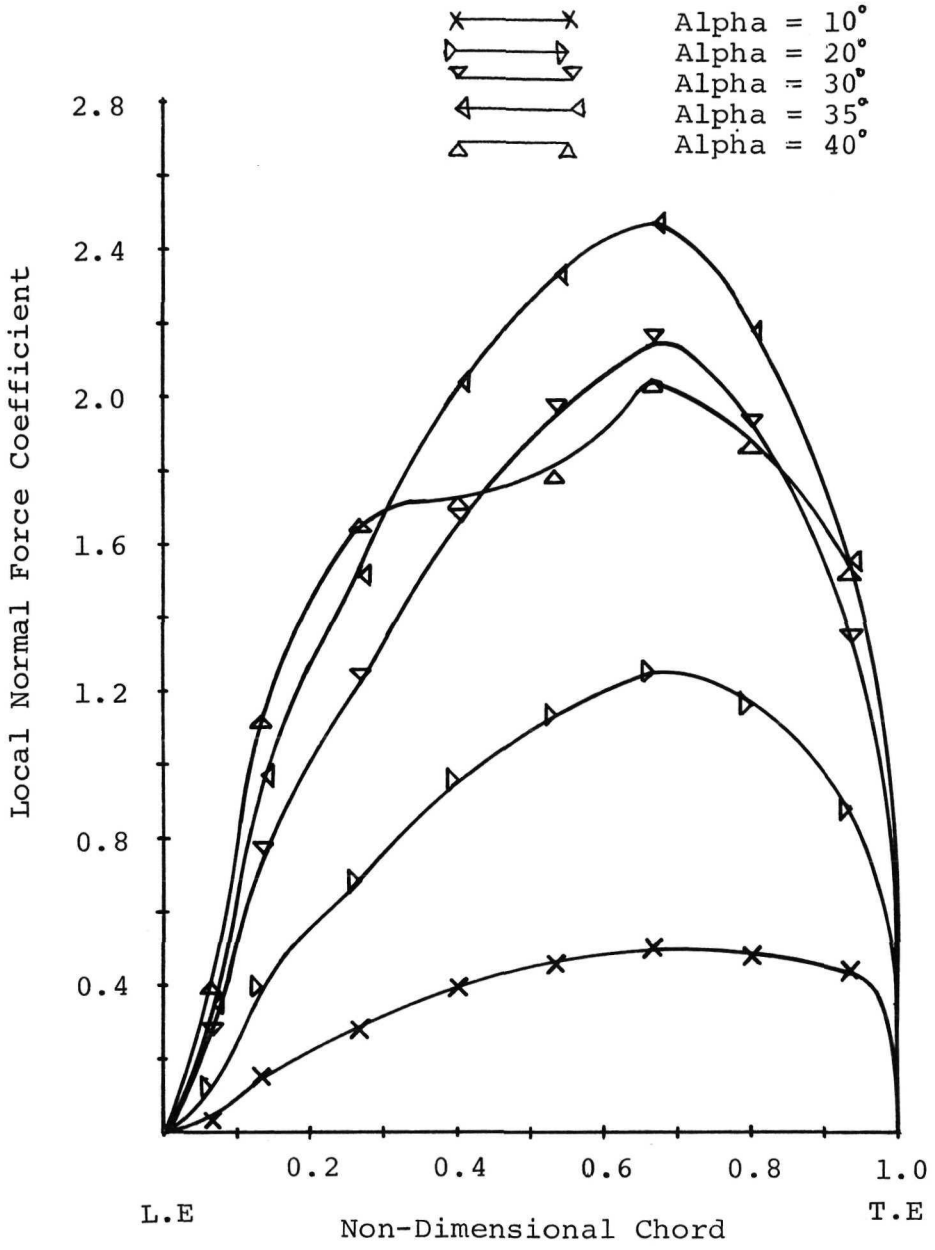

Figure 70 - Longitudinal Distribution of Normal Force - Flat Plate Model

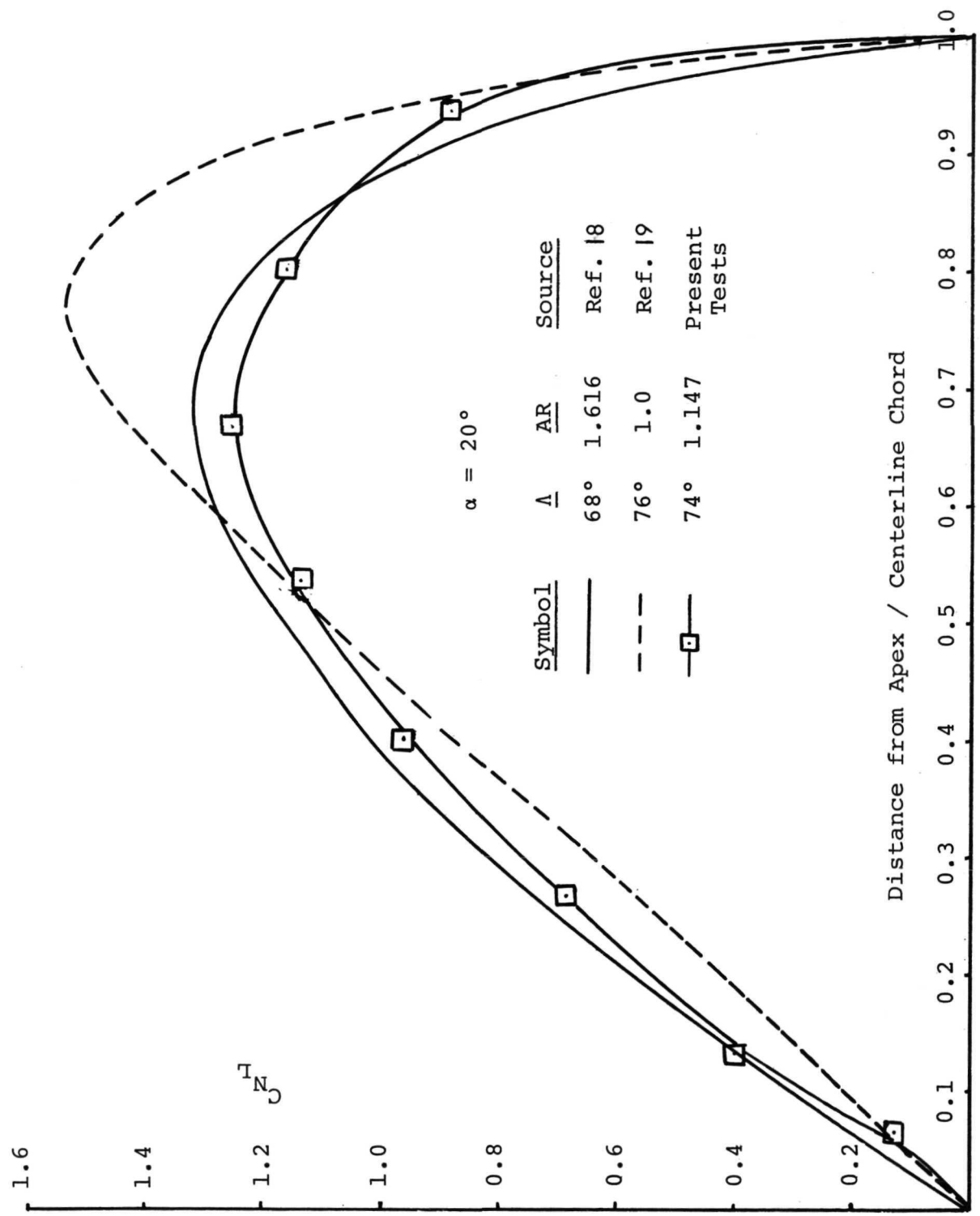

Figure 71 - Comparisons of Longitudinal Loading with Data From Other Sources

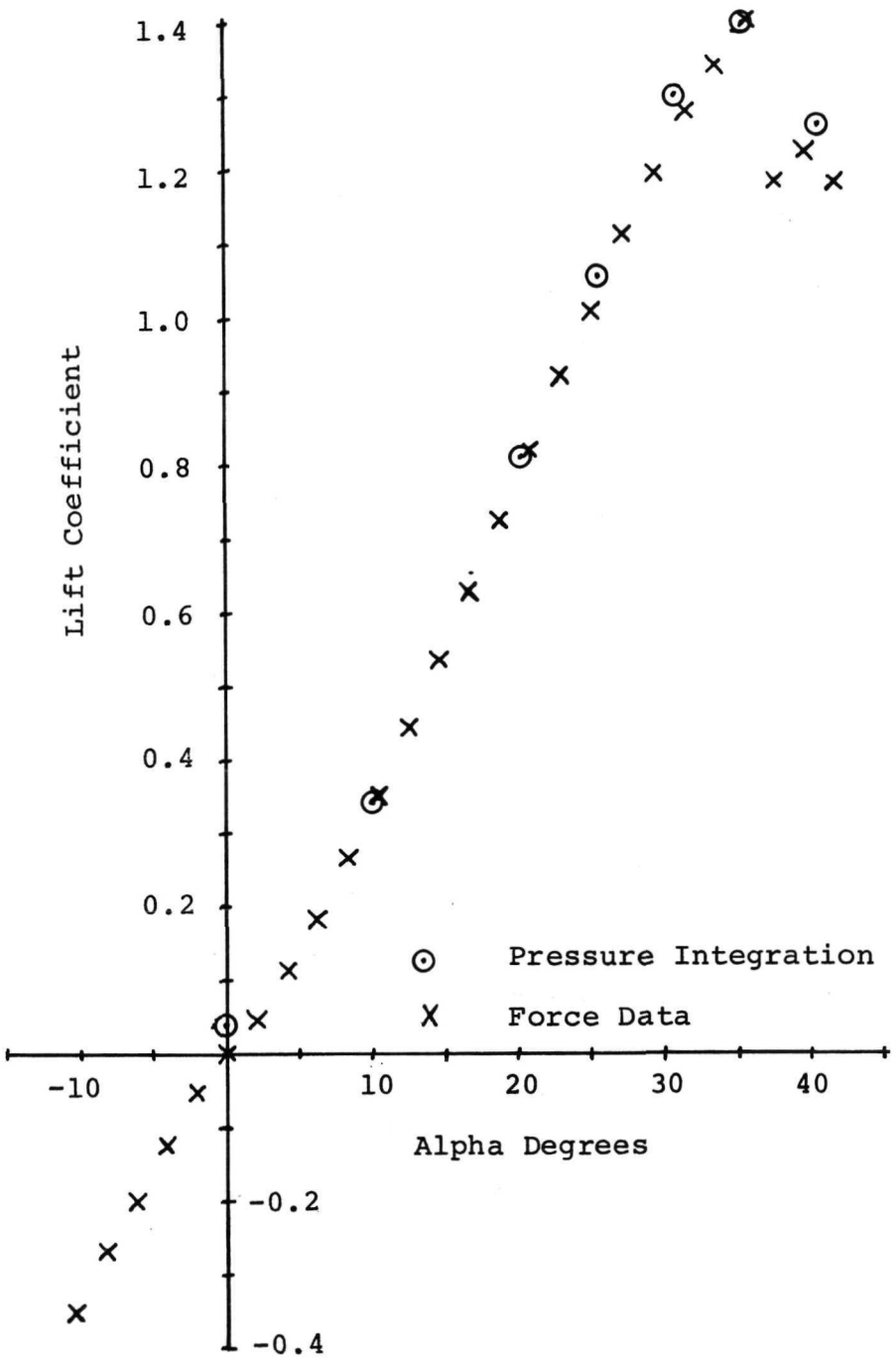

Figure 72 - Comparison of Integrated Pressures with Measured Lift - Flat Plate Model

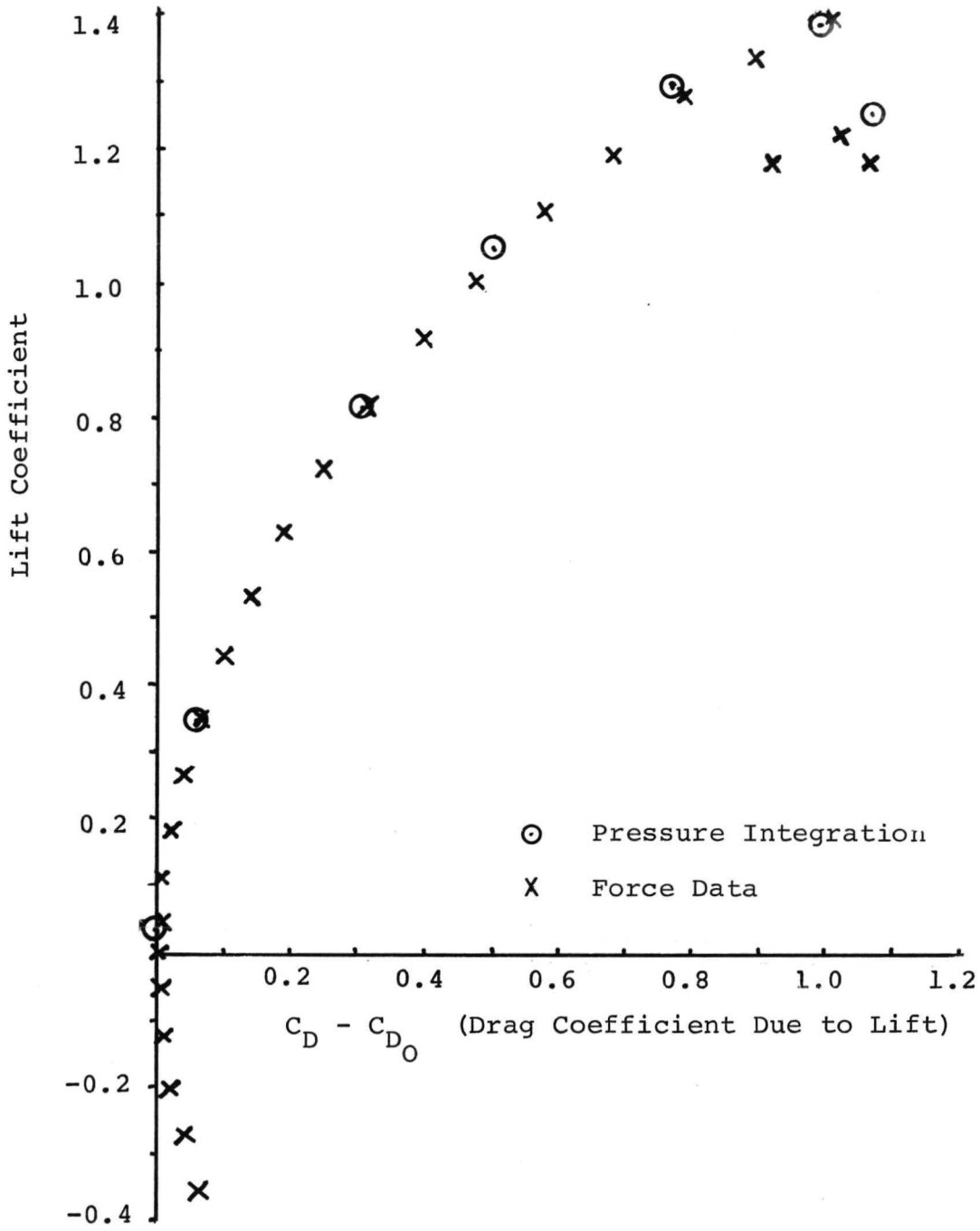

Figure 73 - Comparison of Integrated Pressures with Measured Drag Due to Lift - Flat Plate Model

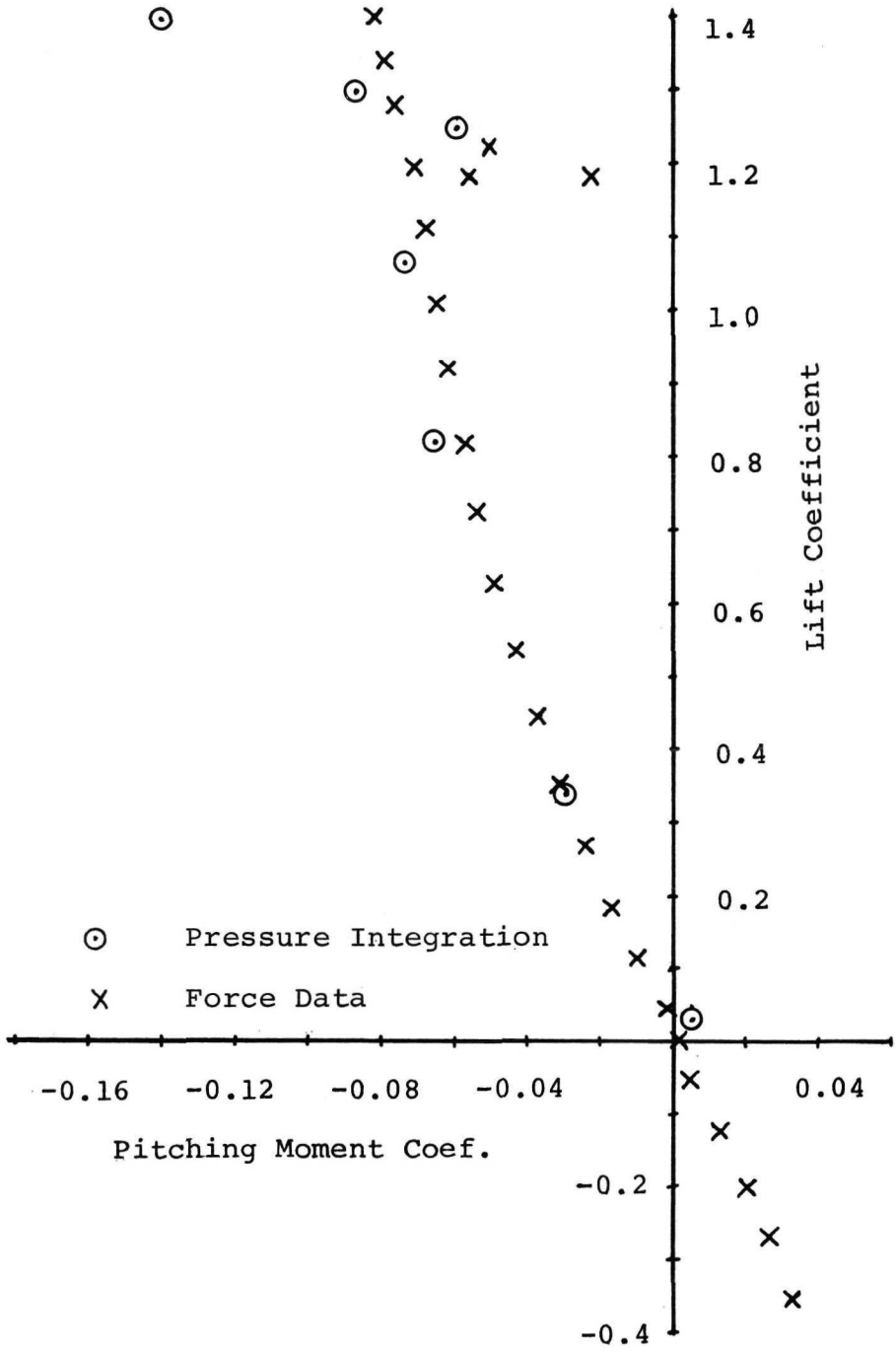

Figure 74 - Comparison of Integrated Pressures with Measured Pitching Characteristics - Flat Plate

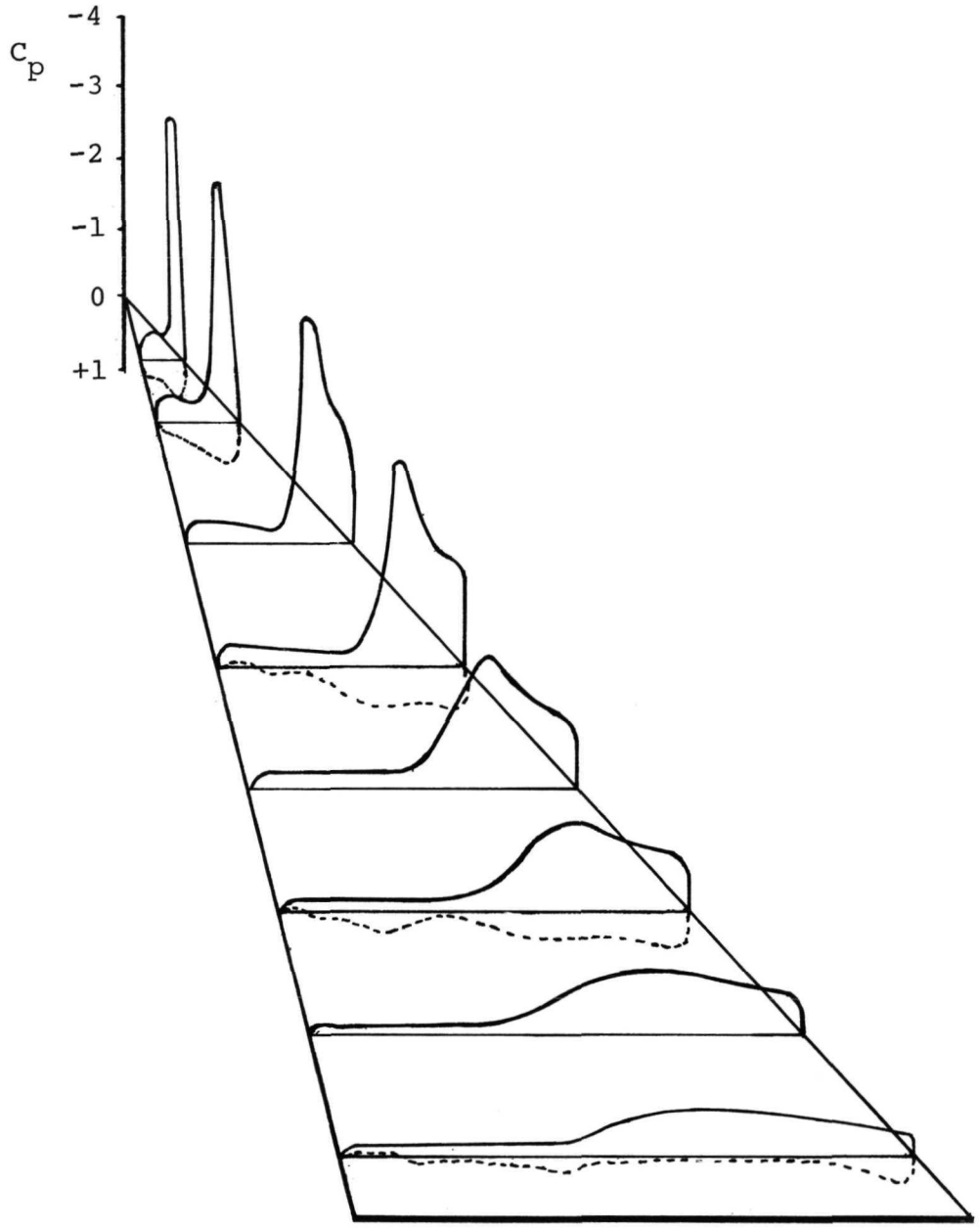

Figure 75 - Pressure Distribution - Flat Plate Model, $\alpha = 20°$, $\beta = 25°$

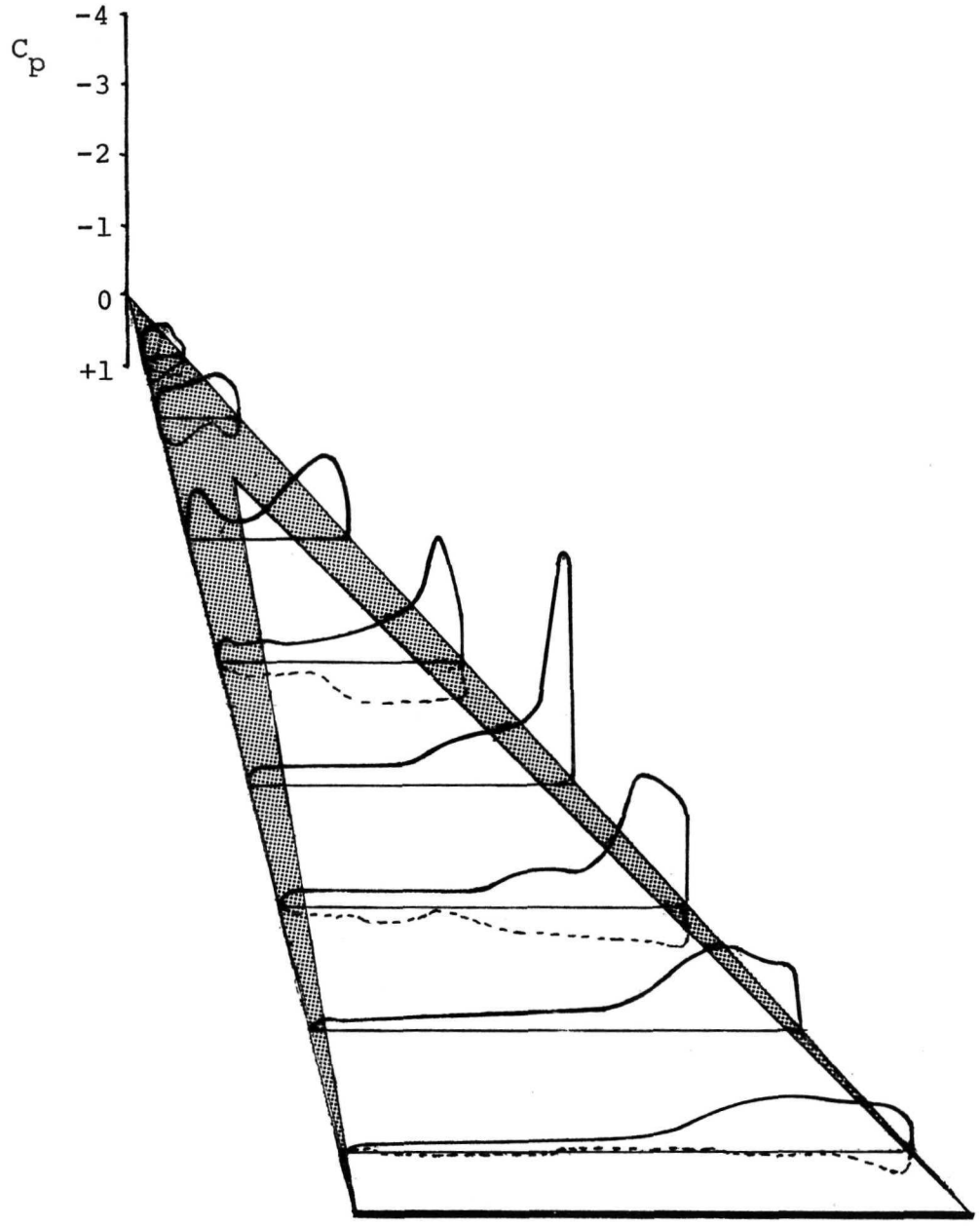

Figure 76 - Pressure Distribution - Apex Camber Model, $\alpha = 20°$, $\beta = 25°$

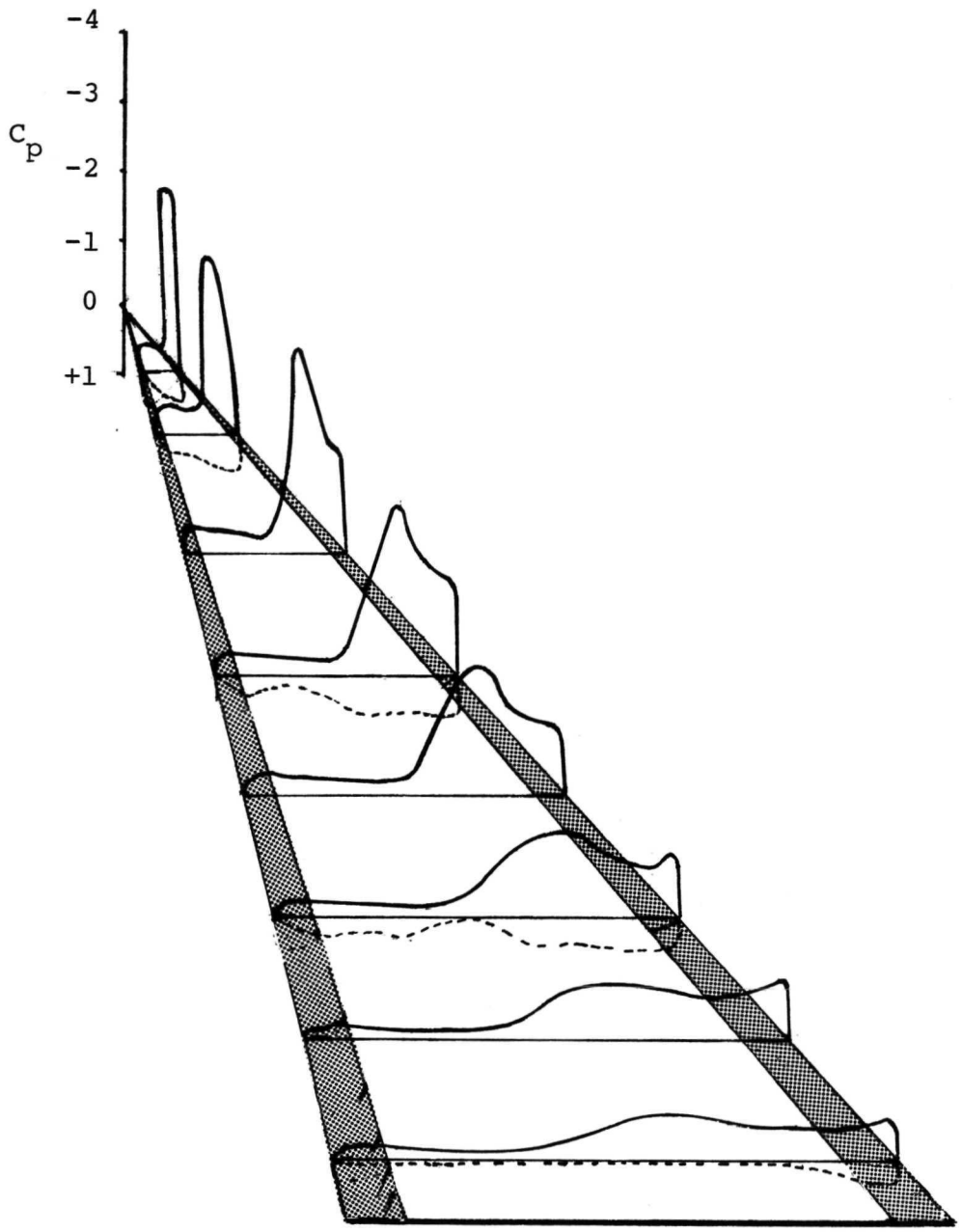

Figure 77 - Pressure Distribution - Conical Camber Model, $\alpha = 20°$, $\beta = 25°$

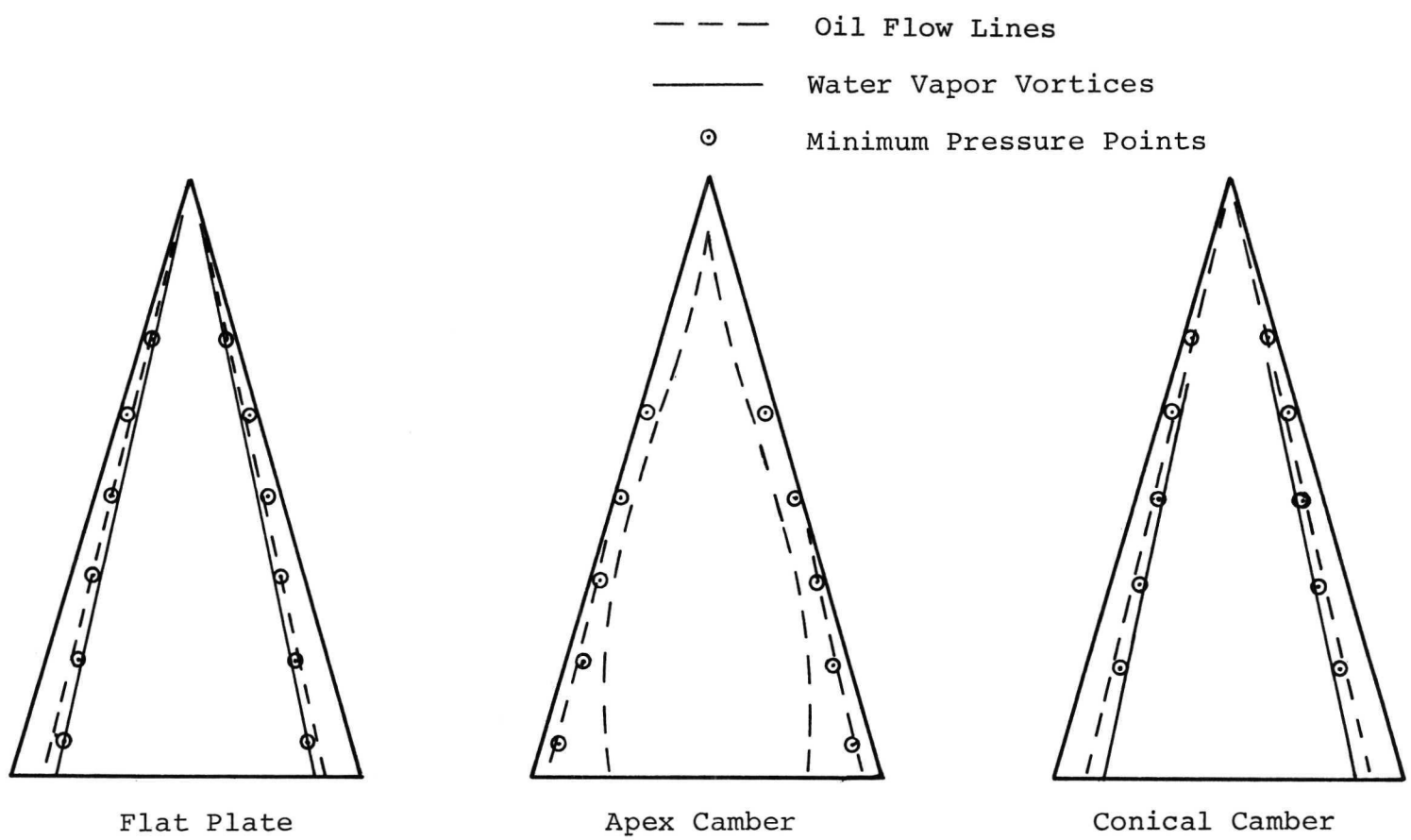

Figure 78 - Combined Flow Field Patterns - $\alpha = 10°$

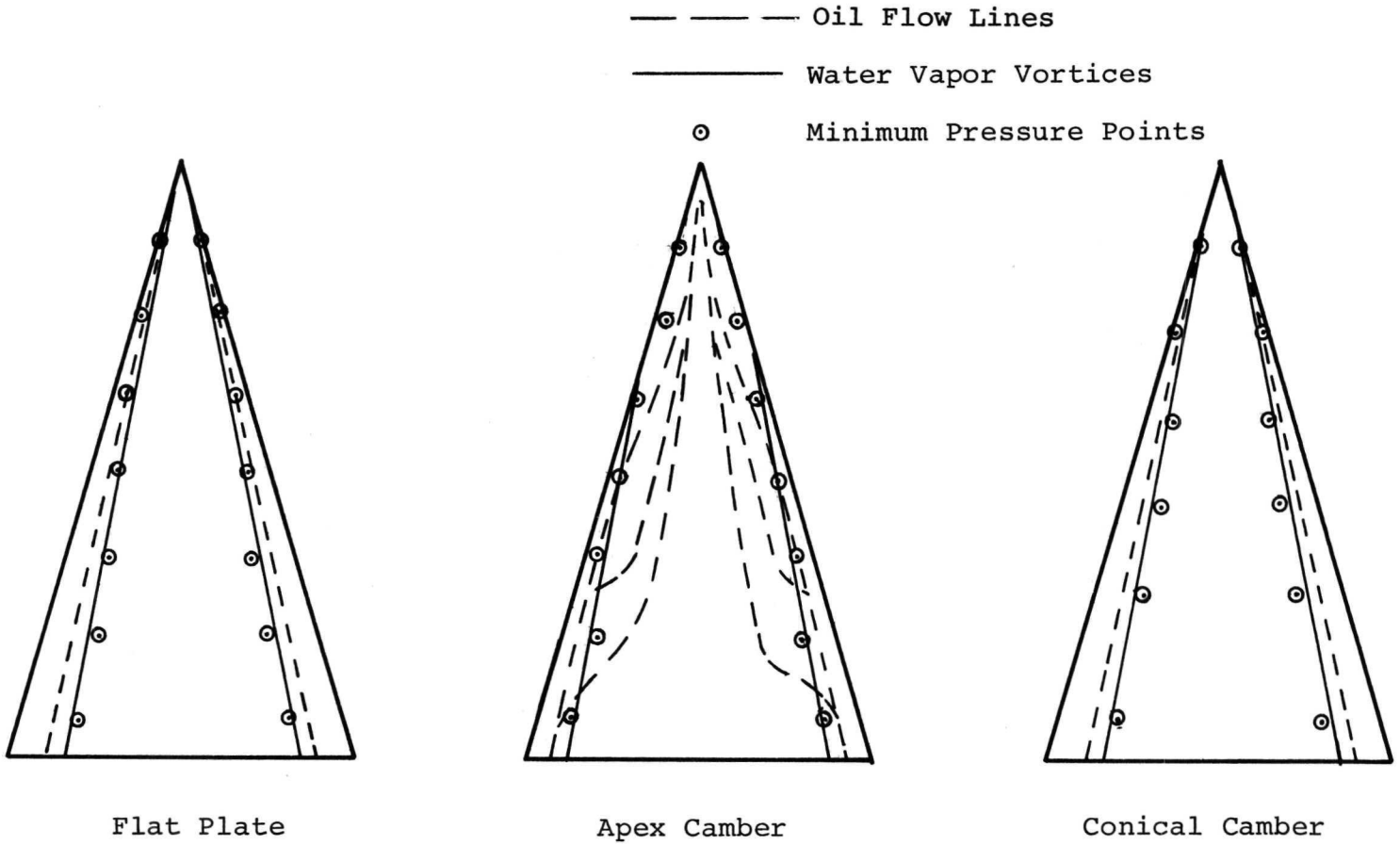

Figure 79 - Combined Flow Field Patterns - $\alpha = 20°$

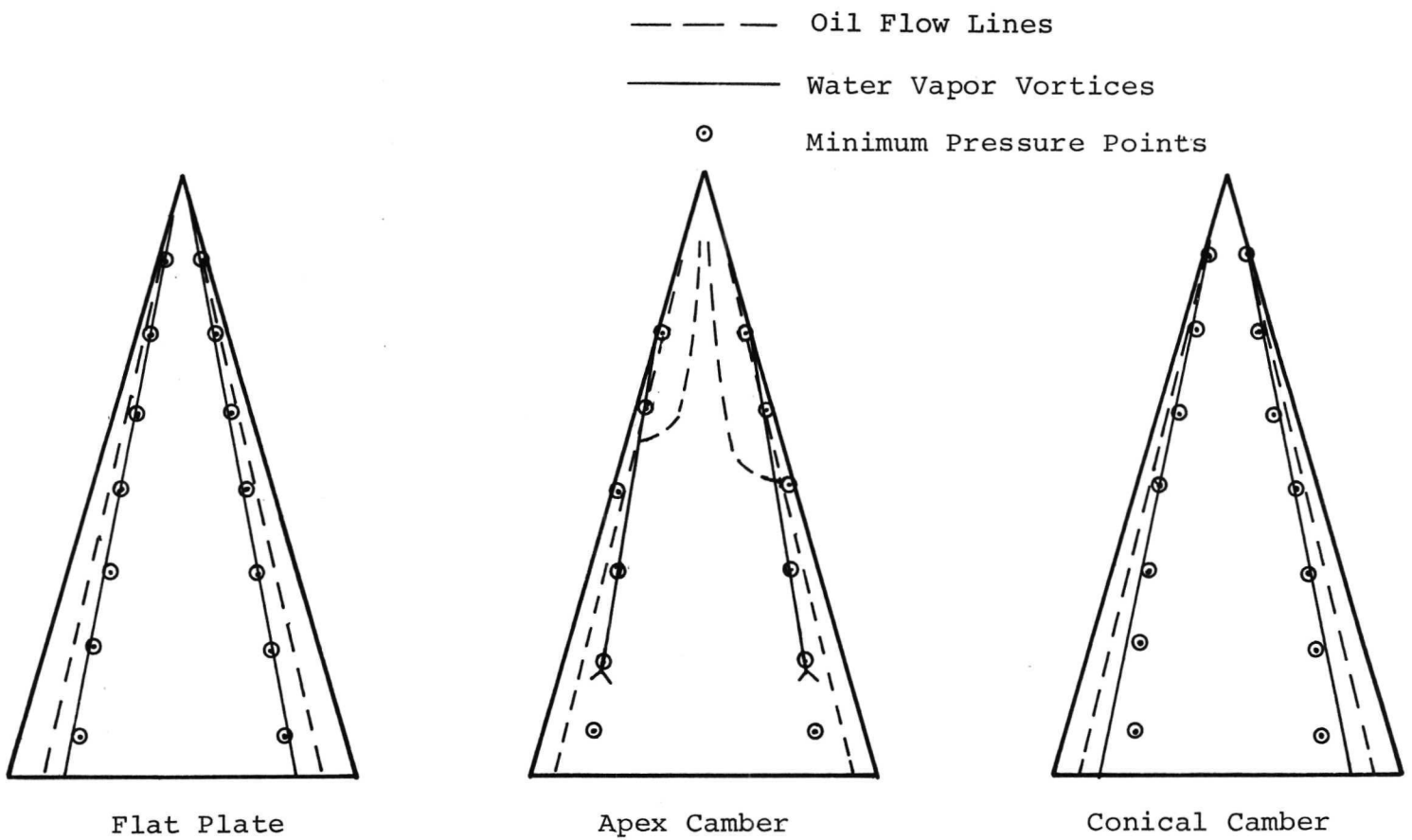

Figure 80 - Combined Flow Field Patterns - $\alpha = 30°$

NATIONAL AERONAUTICS AND SPACE ADMINISTRATION
WASHINGTON, D.C. 20546

OFFICIAL BUSINESS
PENALTY FOR PRIVATE USE $300

FIRST CLASS MAIL

POSTAGE AND FEES PAID
NATIONAL AERONAUTICS AND
SPACE ADMINISTRATION
451

U.S.MAIL

POSTMASTER: If Undeliverable (Section 158 Postal Manual) Do Not Return

"The aeronautical and space activities of the United States shall be conducted so as to contribute . . . to the expansion of human knowledge of phenomena in the atmosphere and space. The Administration shall provide for the widest practicable and appropriate dissemination of information concerning its activities and the results thereof."

—NATIONAL AERONAUTICS AND SPACE ACT OF 1958

NASA SCIENTIFIC AND TECHNICAL PUBLICATIONS

TECHNICAL REPORTS: Scientific and technical information considered important, complete, and a lasting contribution to existing knowledge.

TECHNICAL NOTES: Information less broad in scope but nevertheless of importance as a contribution to existing knowledge.

TECHNICAL MEMORANDUMS: Information receiving limited distribution because of preliminary data, security classification, or other reasons. Also includes conference proceedings with either limited or unlimited distribution.

CONTRACTOR REPORTS: Scientific and technical information generated under a NASA contract or grant and considered an important contribution to existing knowledge.

TECHNICAL TRANSLATIONS: Information published in a foreign language considered to merit NASA distribution in English.

SPECIAL PUBLICATIONS: Information derived from or of value to NASA activities. Publications include final reports of major projects, monographs, data compilations, handbooks, sourcebooks, and special bibliographies.

TECHNOLOGY UTILIZATION PUBLICATIONS: Information on technology used by NASA that may be of particular interest in commercial and other non-aerospace applications. Publications include Tech Briefs, Technology Utilization Reports and Technology Surveys.

Details on the availability of these publications may be obtained from:

SCIENTIFIC AND TECHNICAL INFORMATION OFFICE

NATIONAL AERONAUTICS AND SPACE ADMINISTRATION

Washington, D.C. 20546